Unsteady gas flows and particle dynamics in the shock layer formed by the impingement of a supersonic two-phase jet onto a plate

Dissertation

zur Erlangung des Doktorgrades

der Mathematisch-Naturwissenschaftlichen Fakultäten

der Georg-August-Universität zu Göttingen

vorgelegt von

Konstantin Vladimirovich Klinkov

aus Chulym (Russland)

Göttingen, 2005

D 7

Referent: Prof. Dr. Dirk Ronneberger

Korreferent: PD Dr. Martin Rein

Tag der mündlichen Prüfung: 10 Mai 2005

Contents

Summary

Supersonic particle-laden jets impinging normally on plates are studied. Resulting flow fields include unsteady shock waves of complex structure that are formed in the impingement zone. The complexity of the mathematical description of the flow field in the impingement zone requires experimental measurements covering a wide range of parameters. The free jet studied is characterized by Mach numbers of 2.6-2.8 and stagnation temperatures of 300-500 K. The dispersed phase consists of solid particles of different densities (2700-7900 kg/m^3) and sizes (10-100 μm). First, the parameters of the jet formed by an extremely slender axisymmetric nozzle are examined. Second, unsteady behaviors of jet-plate interactions are studied by a newly developed method of multi-exposure photography, combined with a synchronized pressure measurement on the surface of the plate. Three types of flow oscillations are found and studied by spectrometry of pressure variations in the shock layer. Special attention is focused on flow fields with a recirculating flow. In addition, the dynamics of particles are considered in steady and unsteady flows, both theoretically and experimentally. The formation of a cloud of particles ahead of the plate is studied for different conditions. Finally, particle-surface interactions are studied. Coating formation and the mechanism of impact-induced luminescence are discussed.

Nomenclature

Parameters:

a – speed of sound
A – amplitude of pressure oscillations
c_c – convection velocity
C_d – drag coefficient
d – diameter
f – frequency
h – enthalpy; shock-layer thickness; Planck's constant
h_{coat} – thickness of coating
J – intensity of shock wave: ratio of pressures, after and before shock $J = \dfrac{\hat{p}}{p}$
k – rate of coating growth; Boltzmann's constant
K – curvature the boundary of a jet
L – length
l_b – wavelength of a jet
l_{nozzle} – length of the diverging part of a nozzle
M – Mach number, $M = \dfrac{u}{a}$
M_p – relative particle Mach number, $M = \dfrac{|u_p - u|}{a}$
m – mass
n – ratio of pressures, $n = \dfrac{p_e}{p_a}$
N – ratio of pressures, $N = \dfrac{p_0}{p_a}$
n_p – concentration of particles
p – pressure
p_{pitot} – Pitot pressure
p_{plate} – pressure on the surface of a plate
r – radius; radial coordinate
r_e – exit radius of a nozzle
R – gas constant
Re – Reynolds number
s, S – cross-sectional area
t – time
T – temperature
u – velocity
u_p – velocity of a particle
x – axial coordinate; distance between nozzle exit and either plate or shock
x_{plate} – distance between plate and either shock or particle

α – angle
β – angle of flow deflection

γ – ratio of specific heats at constant pressure (c_p) and volume (c_v), $\gamma = \dfrac{c_p}{c_v}$

δ – boundary-layer thickness
δ_1 – displacement thickness
δ_2 – momentum thickness
λ – wavelength of radiation
μ – dynamic viscosity
ρ – density
σ – standard deviation
σ_p – relaxation length
τ_p – relaxation time
θ – angle of shock inclination

Subscripts:

0 – stagnation value
a – ambient
cr – critical section
e – exit section
exp – exposition; experimental
i – index; incident
m – main
n – normal
p – particle
r – reflection
res – restitution
st – steady
SL – shock layer
$unst$ – unsteady
τ – tangential
σ – shock
ω – expansion wave

1. Introduction

The behavior of supersonic jets that impinge on a solid surface is of a great importance in a variety of industrial and aerospace applications. In the latter case high-speed impinging jets are used, for example, in rocket launching systems, lunar landing modules and short takeoff and vertical landing (STOVL) aircrafts. In these instances, flows in the impingement zone are generally found to be extremely complex. They contain mixed subsonic and supersonic regions, complex interacting shock and expansion systems, a highly non-uniform upstream flow (the free jet), regions of turbulent shear and major flow instabilities. In the case of rocket motors, the presence of high temperatures and solid particles must be added to this list. Under certain conditions the flow field produced by the impinging high-speed lift jets can lead to a degradation of aircraft performance during hover [Alvi et a. 2002]. In addition, the highly unsteady nature of the flow generated by the impingement of a supersonic jet on a surface results in increased noise or overall sound-pressure levels.

Supersonic jets are also employed in process engineering as, for example, in certain variants of thermal spray coating. In particular, in the so-called cold gas dynamic spray (CGDS) deposition method a supersonic jet impinges directly onto a substrate [Alkhimov et al. 1990, Dykhuizen & Smith 1998]. In this method micron-sized particles are accelerated and transported to substrates by means of supersonic free jets. Upon impacting the substrate, particles can stick to the surface and form coatings. Processes occurring in the impingement zone have a profound influence on the quality of coatings produced. Furthermore, noise generated is a serious working environment issue.

Impinging jet flows as well as high-speed particle impacts have been the focus of research for over three decades. Although the mean flow field and acoustic aspects have been carefully examined by a number of investigators, the behavior of both, impinging flows and particles is still not well understood. In addition to numerical computations the complexity of a mathematical description of the flow field in the impingement zone requires experimental measurements covering a wide range of parameters.

In this context we have studied on a laboratory scale phenomena characteristic of the normal impingement of a supersonic jet with and without particles onto a plane surface. When a supersonic jet impinges on a plate a bow shock is formed ahead of the plate. The gas is decelerated on passing the bow shock becomes deflected and is accelerated again in a radial direction up to supersonic velocities. The interaction of the bow shock with shocks that are typically present in impinging supersonic jets results in the formation of a complex flow field. In the shock layer ahead of the plate regions of supersonic and subsonic flows are present together with shear and boundary layers. Such flow fields with transonic regimes are highly unstable. Under certain conditions the flow ahead of the plate as well as shape and position of the bow shock can oscillate strongly in time.

In classic studies Donaldson & Snedeker (1971) and Carling & Hunt (1974) examined the mean flow field in the impingement zone by schlieren photography, surface flow visualization and mean surface-pressure measurements. In addition, Gubanova et al. (1973), Ginzburg et al. (1973) and Kalghatgi & Hunt (1976) have shown that under certain conditions a recirculating flow can occur in the shock layer ahead of the plate. This recirculating flow results in changes of shape and position of the bow shock. Recently, Alvi et al. (2002) have conducted a numerical investigation of such flows. Results of their time-independent computations show a good agreement with experiments. However, the nature of the recirculating flow, in particular, the detailed mechanism by which it is formed, is still not understood. Furthermore, the dynamics of the recirculation bubble have not been studied. This is one focus of the present work.

The globally oscillatory behavior of impinging jets and resulting impingement tones have been studied experimentally [Krothapally et al. 1999] and theoretically [Tam & Ahuja 1990]. One of the main outcomes of these acoustic studies is that impingement tones are caused by a feedback loop through the generation of large-scale structures in the shear layers. However, in these studies the influence of the complex flow field in the impingement zone is not considered. As will be shown in the present work, under certain conditions the influence of the flow field in the impingement zone is of a great significance.

When the concentration of particles in the gas flow is small enough, particles have no influence on the mean parameters of the flow. The particles follow the fluid motion. Nevertheless, the inertia of solid particles leads to features of the particle behavior which is different under certain conditions from the motion of the gas flow. Due to their inertia particles can impinge on the plate while the gas is deflected and flows about the surface. Particles that are reflected from the surface move upstream into the shock layer until they are carried out of the shock layer by the radial wall-jet. Furthermore, reflected particles can penetrate the plate shock and produce distortions of the shock structure formed ahead of the plate. Dunbar et al. (1975) and Alkhimov et al. (1982) have noted such disturbances of bow shocks ahead of bodies in dusty hypersonic flows. They have qualitatively shown that the disturbances are produced by particles reflected from the surface of the body. However, the dynamics of particles in the impingement zone, in particular in the case of an unsteady flow field, was not studied. An investigation of these particle dynamics is another aspect of this work.

In the present study both, the gas flow and the dynamics of individual particles in the shock layer formed by a supersonic two-phase jet impinging normally onto a plate are investigated. The complex time-dependent flow field in the impingement zone does not enable one to develop a mathematical or numerical description of it. For these reasons it is necessary to perform an experimental investigation of impinging jets covering a wide range of parameters and developing a phenomenological model based on semi-empirical approximations. For this purpose the method of high-speed multi-exposure visualization of flow fields and high-speed pressure measurements were applied in combination.

The present work was carried out at a CGDS facility. The *Cold Spray* facility is characterized by a slender nozzle and micron-sized particles, the concentration of which is small enough to not disturb the gas flow. The study of two-phase jets impinging on plates has been divided into three parts. First, gas flows without particles are studied. The second part concerns the particle dynamics in the known gas flow field. Finally, particle-obstacle interactions are studied. Before we start with a discussion of physical results we will introduce, in chapter 2, the experimental setup and a newly developed experimental procedure for studying the unsteady flows in the impingement zone. Thereafter, in chapter 3, various aspects of the gas flow will be considered in the following order: features of under- and overexpanded supersonic free jets issuing from a nozzle, normal jet impingement on a flat plate, and the characteristics of flow oscillations. Results relating to particle-laden flows are the topic of chapter 4. First, a computational and experimental study of a two-phase free jet formed by a supersonic nozzle will be presented. Then, the characteristics of particle behavior in the impingement zone are considered. In chapter 5 the features of particle-plate interactions will be discussed. The discussion is divided into two parts. In the first part the dynamics of the formation of coatings is studied while the second part concerns the properties of luminescence produced by particle impacts on the plate surface. This is followed by a conclusion.

2. Experimental setup and methods

2.1 Cold Spray facility

The present work was carried out using a facility for *Cold Spray* Deposition. In the cold gas-dynamic spraying method, also called *Cold Spray*, a deposition of coatings is performed by the impact of high-velocity particles that are in a solid state [Alkhimov et al. 1990, Dykhuizen & Smith 1998]. Basics of the method are shown in Fig. 2.1. Powder particles are injected into a gas flow upstream of the throat of a supersonic nozzle. Particles are accelerated by the expanding gas and transported to the substrate by the supersonic jet emanating from the nozzle. On impact onto the substrate some particles are reflected from the substrate while others stick together and build up a coating.
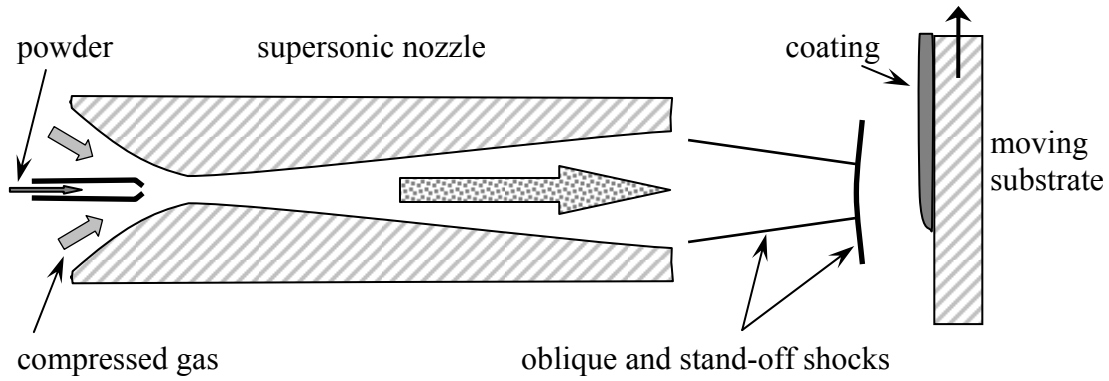

Fig. 2.1. Principles of the *Cold Spray* deposition process.

Main elements of the *Cold Spray* facility of the Institute of Aerodynamics and Flow Technology of the German Aerospace Center are shown in Fig. 2.2. Compressed gas is divided into two parts. The main gas flow passes through a heater and then enters into the pre-chamber of a supersonic nozzle. In the pre-chamber the pressure and temperature of the gas (in the present investigations air has always been used) can be varied from 10 bar to 30 bar and from 300 K to 800 K, respectively. The compressed gas is expanded by an axisymmetric converging-diverging nozzle. The supersonic jet which issues from the nozzle has a flow Mach number of M = 2.78 and the ratio n of the static pressure p_e in the supersonic flow at the nozzle exit and the ambient pressure p_a, $n = p_e / p_a$, is in the range of $n = 0.3 - 1.1$. The diverging part of the nozzle is conical and has a length of 100 mm. The radiuses of the critical and exit cross-sections are $r_{cr} = 3.3$ and $r_e = 6.6$ mm, respectively. The outside diameter of the nozzle is constant, 35 mm. Thus, the width of the nozzle lips (about 15 mm) is clearly greater than the exit diameter of the nozzle.
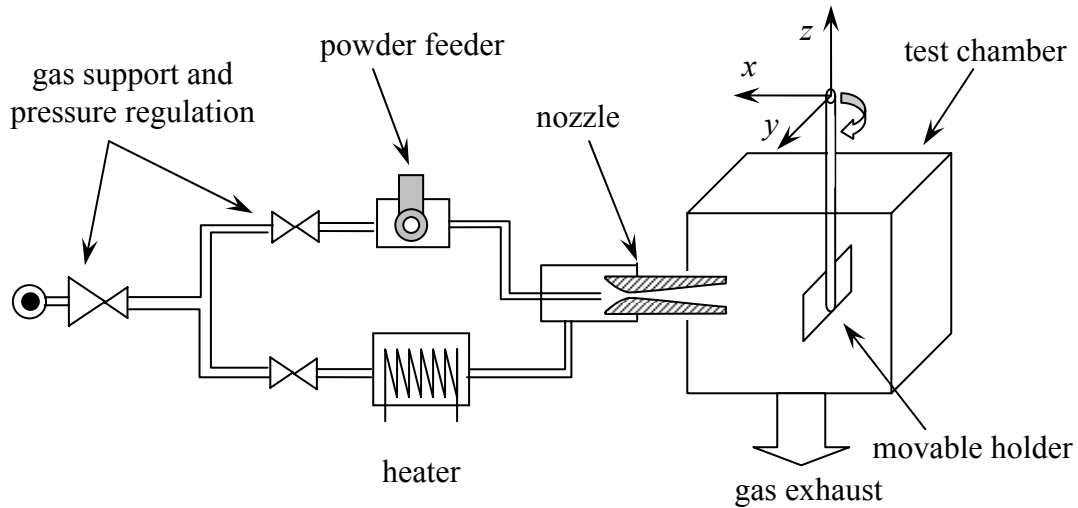
Fig. 2.2. Experimental setup.

The secondary part of the compressed gas is applied to inject powder particles into the main flow. Powder is mixed into the secondary gas flow by a powder-feeder. The two-phase flow is then injected into the main flow in the converging part of the nozzle. In experiments powders of the following metals have been used: aluminium (Al), zinc (Zn), copper (Cu) and iron (Fe). The diameter of the particles is in the range of 10 – 100 μm.

All experiments are performed in a test chamber. In this manner, the powder-laden gas does not pollute the laboratory. Powder laden gas which is present in the chamber is pumped out of the test chamber by a gas exhaust system. Optical and other devices are thus not polluted by the fine powder used. In order to allow for a convenient performance of optical investigations the size of the chamber is small (dimensions about 0.7 x 0.7 x 0.7 m^3). In the chamber a holder is present, which is used to move substrates in three directions (*x*-, *y*-, *z*-axes) or to rotate substrates about one of the axes (*z*-axis) by step-motors. The holder enables one to move plates and other objects with a linear velocity of up to 0.2 m/s and an accuracy in position and angle of 0.025 mm and 1.8° (grad), respectively. Glass windows (size: 0.08 x 0.24 m^2) allow to apply optical methods for investigating the flow field.

The cold spray facility is fully computer controlled. The gas flow is regulated by an SPS-program (SPS: Speicher Programmierbare Steuerung). Specially designed software for both, driving stepmotors and data acquisition and processing that have mostly been performed by digital techniques and computers is described in the Appendix.

2.2 Estimates of characteristic parameters

In this chapter we estimate typical time and length scales of phenomena which will be studied in the following chapters. The values obtained are used to determine the required capabilities of a diagnostic system.

Object of the investigations is a supersonic jet impinging on a plate. In particular, the flow field in the shock layer ahead of the plate is of interest. The gas flow can be

laden by solid particles. The purpose is to study the behavior of particles as well as shocks when the jet impinges on a barrier. Some features of the studied flows require special methods of investigation.

Firstly, it is necessary to note that the total size of the whole flow field is small. The diameter of the jet is about 6.6 mm and the distance between nozzle exit and plate equals several nozzle diameters. As a result the important regions of the flow field such as boundary and mixing layers, shock intersections and the shock layer ahead of the barrier have extensions of about 1 mm and are usually smaller. This limits the geometrical size of devices which are to be located in the flow (e.g. Pitot-tubes and other pressure transducers) and requires an accuracy in positioning such devices of at least 0.1 mm (10 %) for all diagnostic systems. Also, the small geometrical size corresponds to larger frequencies (or smaller characteristic times) of instabilities in the flow, as compared to a larger system. The length scale of objects is compared with the jet diameter ($d_{jet} \sim 6 \cdot 10^{-3}$ m). Based on the sound speed, a, in air at room temperature ($a \sim 3 \cdot 10^{2}$ m/s), large scale oscillations that are expected to occur, may have a frequency of up to 50 kHz. That requires suitable time characteristics of a diagnostic system of $\Delta t_{meas} \sim 2 \cdot 10^{-5}$ s.

The second important limiting characteristic of the studied phenomena is the small size and high velocity of particles in the two-phase flow. Furthermore, in the shock layer ahead of the barrier particles exhibit a complex behavior (interaction with shocks, reflection from the barrier, particle-particle interactions). An application of well-known optical methods, such as Laser-2-Focus (L2F), Laser-Doppler (LDV) or similar particle velocimetry methods does not give the required information about the flow field. A serious disadvantage of such methods of local measurements is the impossibility to obtain the large-scale information about objects, e.g., to obtain not only the velocity of particles at a given location, but also to obtain information about the size of each particle and about the behavior of particles and the gas flow on the whole. Also, the spatial resolution of these methods is usually determined by the size of the focal spot of the light beam and usually equals several decimal fractions of a millimeter. Thus it is complicated to identify the behavior of single particles in the shock layer which has a thickness of about 1 mm in the present case. In addition, the application of these methods is connected with technical difficulties caused by the proximity of the surface of the barrier [Alkhimov et al. 1997, Klinkov & Rein 2004, Klinkov et al. 2004].

In our case more suitable diagnostics of two-phase flows are based on direct imaging of particles, e.g. by the so-called Particle Image Velocimetry (PIV) [Willert et al. 1996, Raffel et al. 1998]. In the present work the concentration of particles varied between 10^{8} m^{-3} in the free jet and 10^{9} m^{-3} in the shock layer. The measurements show that only a few particles traverse a cross-section of the jet every microsecond. For this reason and considering further the very complicated traces of particles in the shock layer ahead of a barrier where particles moving in the opposite directions are present, an application of standard 2-Frames PIV with subsequent statistical evaluations is disadvantageous. Also, presently it is not possible, for technical reasons, to follow an individual particle. Under these conditions an ideal diagnostic method is the multi-frame particle trace visualization. Let us estimate main parameters needed for such a particle tracing system.

As stated above particles have a diameter in the range of $10 - 100$ μm. Particle velocities can vary from 50 m/s in the subsonic zone ahead of the barrier to 500 m/s in the supersonic free jet. Although mesh sieves have been applied before experiments were performed, particle sizes are not exactly known. For this reason we considered a shadowgraph system that enables one to determine particle sizes from the pictures

obtained. In order to obtain well recognizable shadow images of particles it is necessary to keep the duration of exposure well below the time interval in which the particle moves one diameter (Fig. 2.3). For a particle with a diameter of 10 μm and a velocity of 500 m/s this time equals 20 ns. The time interval between two images of a particle in the flow should correspond to a time interval during which the particle moves several diameters, for instance, three diameters. For small fast particles ($d_p = 10$ μm, $u_p = 500$ m/s) and bigger slow particles ($d_p = 100$ μm, $u_p = 50$ m/s) these time intervals are 60 ns and 6 μs, respectively.
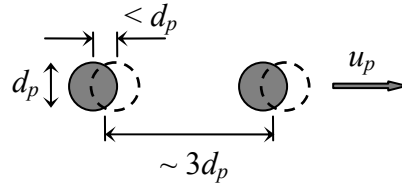

Fig. 2.3. Determination of characteristic times of a multi-frame visualization scheme.

In order to estimate which spatial resolution is necessary let us apply a dimensionless unit, a so-called *pixel*, which is assumed to be the smallest information element of an image. In the case of a digital photoreceiver pixels correspond to elementary photosensitive cells. If an error of 10 % is tolerated in determining the size, the image of the smallest particles (diameter: 10 μm) should consist of at least 10 pixels. That suggests an image scale of 1 pixel ≈ 1 μm. Further, in order for the system to work properly at least one particle should be caught on each camera-frame. In the shock layer the particle concentration is about 10^9 m^{-3}. Therefore a cube with sides of about 1 mm contains one particle on average. Thus the total width of an image should equal 1000 pixels. Hence, most modern CCD-cameras are suitable since they have a matrix with more than 1 Mio cells. The physical size of one elementary photosensitive cell is usually equal to $2-5$ μm. This means that the optical system should produce an image having a size of $2-5$ sizes of the object projected.

A multi-frame visualization system satisfying these conditions typically includes a short pulse source of light (e.g. a solid-state laser) and/or a high-speed photo-receiver (e.g. a CCD-camera) for every frame. These devices need to be synchronized by a high-speed electronic signal-sequencer. Setting up such a system is connected with great difficulties due to its complexity and expensiveness. Therefore, instead of a multi-frame visualization system a multi-exposure visualization system has been developed here. In such system all images of a particle track are exposed in one shot of a photoreceiver. In this manner the capabilities of the diagnostic system are kept at the same level as that of a multi-frame system while essentially simplifying its construction. The multi-exposure system developed and applied in the present study will be described in detail in section 2.4.

2.3 Flow field investigations by pressure measurements and shadowgraphy

2.3.1 Devices and methods of pressure measurements

The flow Mach number is determined using an impact pressure tube, a so-called *Pitot* tube. Geometric parameters of the Pitot-tube are depicted in Fig. 2.4. In supersonic flows a bow shock is formed ahead of the Pitot-tube. If the axis of the Pitot-tube is aligned along the jet axis the approaching flow suffers full deceleration. First, the gas passes through a normal shock and becomes subsonic. After the shock it is smoothly decelerated to velocity zero at the tube inlet. at the same time the pressure increases to the stagnation pressure. The stagnation pressure of a gas decreases when the gas passes through a shock. The ratio of the stagnation pressure before the shock to that after the shock is a function of the Mach number M ahead of the shock [Abramovich 1963, Oswatitsch 1976] :

$$\frac{p_{pitot}}{p_{0\,flow}} = \left(\frac{\gamma+1}{2}\right)^{\frac{\gamma+1}{\gamma-1}} \left(\frac{2}{\gamma-1}\right)^{\frac{1}{\gamma-1}} \cdot \frac{M^{\frac{2\gamma}{\gamma-1}}}{\left(\frac{2\gamma}{\gamma-1}M^2-1\right)^{\frac{1}{\gamma-1}}} \cdot \frac{1}{\left(1+\frac{\gamma-1}{2}M^2\right)^{\frac{\gamma}{\gamma-1}}} \cdot \quad (2.1)$$

Here, the stagnation pressure after the shock equals the Pitot-pressure p_{pitot} and $p_{0\,flow}$ is the stagnation pressure of the gas ahead of the bow shock. At the nozzle exit, outside of the boundary layer, the stagnation pressure of the flow is equal to the stagnation pressure in the pre-chamber of the nozzle, i.e. $p_{0\,flow} = p_0$. Hence, by measuring the Pitot-pressure on the jet axis the local flow Mach number of the jet can be calculated.
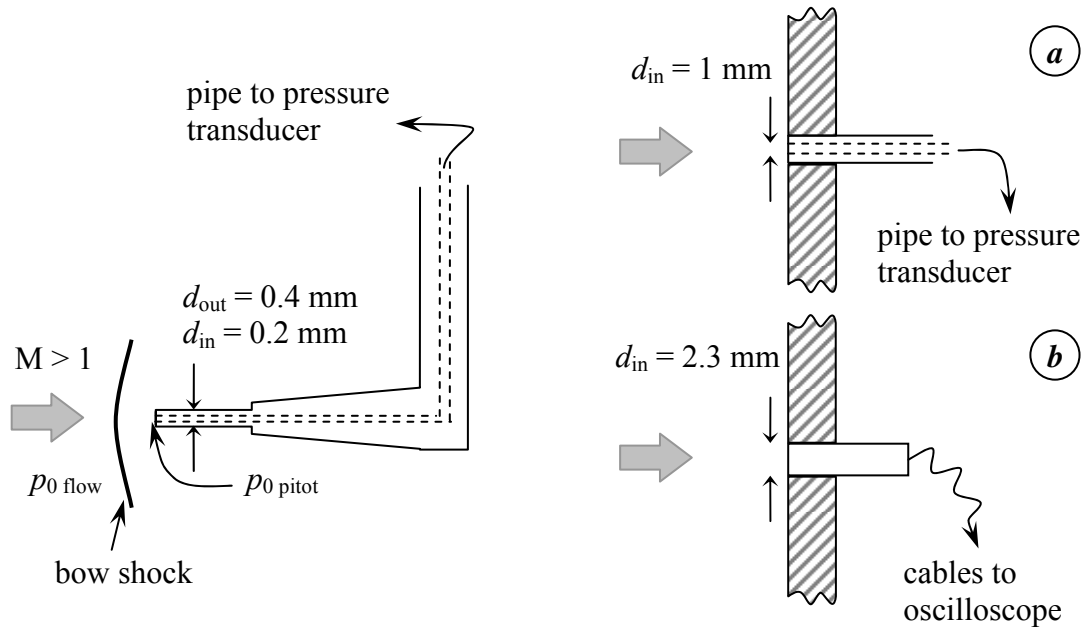

Fig. 2.4. Pitot-tube in supersonic flow.

Fig. 2.5. Plate-pressure measurements: *a*) static pressure tube, *b*) high performance pressure transducer.

The pressure was also measured on the surface of the plate in the jet impingement zone. Arrangement and dimensions of the pressure transducers used are shown in Fig. 2.5. A static pressure tube (Fig. 2.5*a*) has been used to obtain the mean value of the pressure and in order to calibrate a high-speed pressure transducer (Fig. 2.5*b*). High frequency pressure fluctuations were measured by the high-performance transducer (Fig. 2.5*b*). The main parameters of the high-performance transducer are given in Table 2.1.

Table 2.1. Characteristics of the pressure transducer.

Transducer	"Kulite" XCL-100 series
Geometry of sensitive element	round, diameter 2.3 mm
Pressure measurement accuracy	0.1% in the range of $p = 1 - 35$ bar
Frequency band	$0 - 1$ MHz (3 dB)

For digitizing and storing pressure signals a high performance multi-channel oscilloscope of the Hewlett-Packard ULTIMA-500 series was applied. Sampling rates in the range of 250 kHz – 10 MHz and a quantization of 12 bit were used. In order to obtain spectrums of pressure signals a Discrete Fast Fourier Transform was applied. Samples having a length of 4096 values, averaged by accumulation of 20 measurements, were subjected to transformation using the Hanning window method.

2.3.2 Shadowgraphy

In most of the experiments a direct "focused" shadowgraphy in parallel light was applied in order to visualize the flow field [Settles 2001]. The general scheme is shown in Fig. 2.6. A compact-arc air-cooled lamp is applied as a continuous-wave light source. In the case of multi-exposure visualizations a modulated laser diode is used as a short pulsed light source. As a photoreceiver a digital CCD-camera is applied. All camera functions are remotely controlled by a personal computer via a digital interface. The main characteristics of the laser and the CCD-camera are given in Tables 2.2 and 2.3.

The first part of the optical scheme, the so-called illumination section, is designed for producing a regular parallel beam of light. This part includes a condenser lens, a pinhole and a first field lens. The pinhole functions as a spatial filter. When continuous-wave light of a lamp is used the pinhole has a diameter of 0.1 mm and 50 μm for light of a laser diode. The first and second field lenses are similar and have a focus length of 310 mm and an aperture of 100 mm. The second field lens and an optional focusing lens are used to image the shadowgram plane F onto a screen at F*. Such a scheme allows to adjust the magnification and sensitivity of the visualization system.
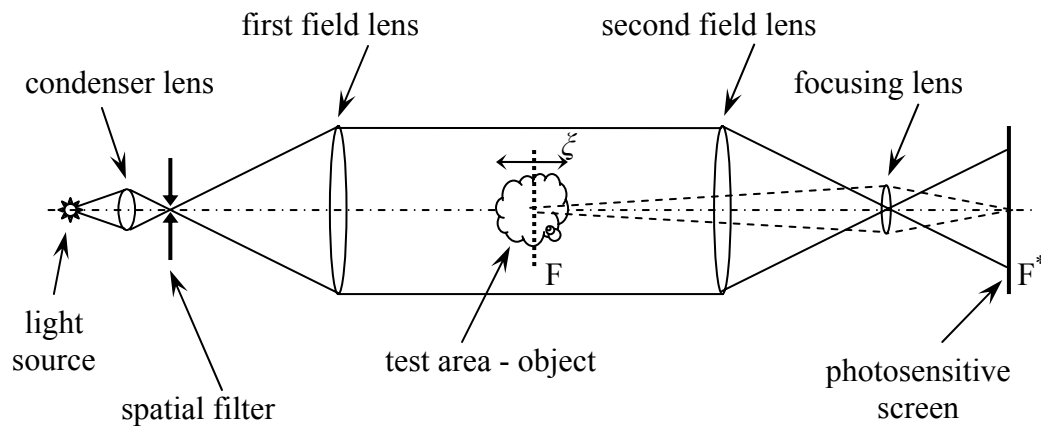
Fig. 2.6. Scheme of "focused" shadowgraphy.

Table 2.2. Characteristics of the laser.

Light source	semiconductor laser diode
Ligth wavelength	660 nm
Illumination power	10 mW (cw)
Beam diameter	4 mm
Beam divergence	0.3 mrad
Modulation bandwidth	0 (cw) – 50 MHz

Table 2.3. Characteristics of the CCD-camera.

Type	"PCO CCD imaging" PixelFly series
Scan area	6.3 x 4.7 mm^2
Spatial resolution	1360 x 1024 pixel
Pixel size	4.65 x 4.65 μm^2
Dynamic resolution	12 bit
Readout noise	12 e$^-$
Spectral range	280 – 1100 nm
Exposure time	10 μs – 10 ms
Imaging frequency	24 fps

It is necessary to comment on some features of shadowgraphy with lasers as a light source. The laser illumination is monochromatic and coherent. The first property offers the advantages of evading chromatic aberration effects and providing an intense light emission in which all energy is pumped into one spectral line of light. On the other hand the intense and spatially coherent laser emission requires clean, high-quality, scratch-free optics. Diffraction on the lenses and objects, and coherent artifact noise degrade the resulting shadow image. For example, diffraction rings can always be seen in shadow pictures obtained with a laser light source.
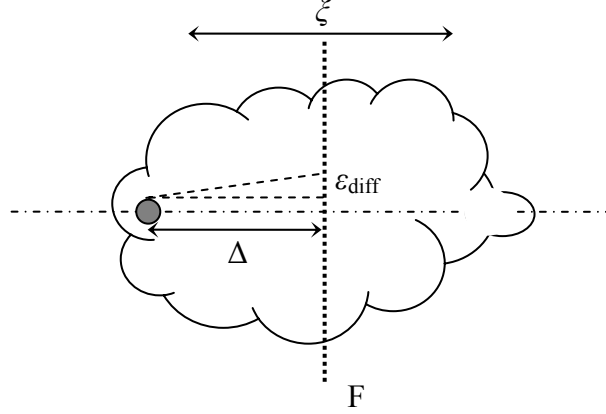

Fig. 2.7. Blur of particle image due to diffraction.

Let us consider particularly the diffraction effects on the objects studied: particles and shocks. Diffraction by small particles results in a strong diffraction blur in the shadowgrams. The size of blur is comparable with the size of the particle image. The diffraction effects are so strong that even particles which are only slightly shifted from the focus plane, have no sharp images. On the one hand this makes adjusting the visualization system difficult. On the other hand this essentially decreases the thickness ζ of the test volume (Fig. 2.6), since it allows to select only sharp images of particles. The level of unsharpness ε_{diff} associated with diffraction blur can be estimated as

$$2 \cdot \varepsilon_{diff} \approx 2 \frac{\lambda}{d_p} \Delta, \qquad (2.2)$$

where λ is the light wavelength, d_p is an object size (particle diameter) and Δ is the distance between an object and the shadowgram plane F (Fig. 2.7). A small relative shift of a particle out of the focus plane is sufficient to recognize a diffraction blur on the shadowgraph picture. For example, for $\lambda = 0.66$ μm, $d_p = 50$ μm and $\Delta = 1$ mm the change of the image diameter equals approximately 26 μm, e.g. about 50 %.

These results have been examined experimentally. Shadowgraph pictures of particles which were mounted on a transparent object-plate have been obtained for different distances Δ between object-plate and shadowgram plane F (Fig. 2.7). Under conditions of the experiment in the obtained images the magnitude of the diffraction blur agrees with the values predicted by eq. 2.2. The experiments have shown that such shadowgraph pictures enable one to measure the particle size d_p and to estimate the distance Δ between the particle and the focal plan. This finding has been applied in measurements of parameters of two-phase flows that will be described in chapter 4.

2.4 Multi-exposure method of visualization

2.4.1 General scheme of the method

For investigating the motion of particles and discontinuities in a supersonic flow a multi-exposure method based on direct shadowgraphy has been set up. The general scheme of the diagnostic system is given in Fig. 2.8. A modulated laser diode is applied as a short-pulse light source. The optical part has been described above. The shadowgram images are received and digitized by CCD-camera. Control signals for laser, camera and other devices are formed by a special programmable device, called a signal sequencer. The whole system, including storage of images, is controlled by a personal computer. The main characteristics of the diagnostic system are a wide variability of both pulse shapes and sequences of light pulses. The duration of single pulses is as low as 20 ns and the interval between different pulses is greater than 20 ns. The exposure time of the CCD-camera is as low as 10 μs. The time delay of a signal between the signal sequencer and any device is smaller than 150 ns. The time accuracy of the signal sequencer is 1 ns.
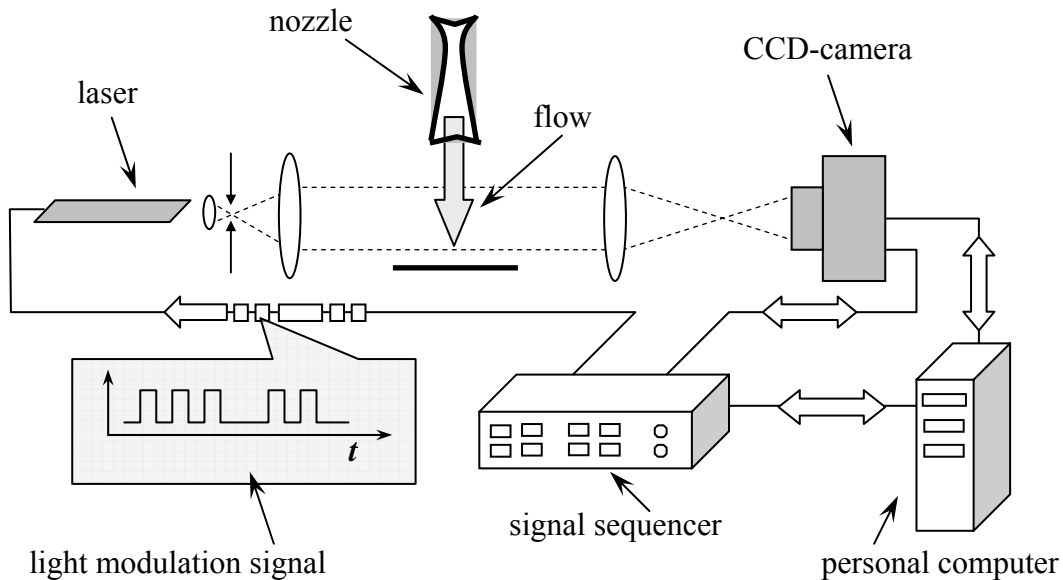
Fig. 2.8. Sketch of the diagnostic system.

The results which will be presented below show a wide applicability of the multi-exposure visualization method in studying two-phase flows. In particular, the possibility of applying the method to investigating the behavior of particles at small concentrations is advantageous compared to well-known methods such as PIV, which requires many particles for statistics. Furthermore, the method is well-suited for taking shadowgraphs of the gas flow in addition to particle images. Obtaining information on the gas flow and the particle motion at the same time enables an easy interpretation of processes occurring in the flow. The wide variability of sequences of light pulses allows for determining not only parameters (e.g., velocity) of an object but also the rate of change (e.g., acceleration) at different times. Furthermore it is possible to obtain

additional information about objects as, for example, the shape and size of particles or the shape of shock waves.

A semiconductor laser was used as a source of light pulses. In this manner complex high-voltage devices for pumping and modulating of the light have been avoided. Furthermore, the use of a semiconductor laser renders the adjustment and operation of the diagnostic system particularly simple.

2.4.2 Visualization of the motion of particles

The visualization system allows to determine the velocity of particles in supersonic gas flows. For this purpose the particle-tracking method was used. In order to obtain particle traces in the free jet (Fig. 2.9*a*) a sequence of three light pulses was applied during one exposure time of the camera-shutter. The duration of the single pulses was 50 ns each, and the time intervals between the pulses were 200 ns and 400 ns, respectively (Fig. 2.10). Different intervals were chosen in order to determine the direction of the particle motion.

The diagnostic method of multi-exposure visualization is particularly well suited for studying processes in the thin shock layer ahead of a plate in supersonic jet impingement flows. By varying the number and duration of light pulses, and the intervals between individual pulses the motion of both, the bow shock and particles in the shock layer can be directly observed. An image of particles in the shock layer ahead of the plate is shown in Fig. 2.9*b*. A sequence of three light pulses (duration: 50 ns) was applied. The velocity of most particles in the cloud ahead of the plate is so small that the short time intervals between the pulses (200 ns and 400 ns, respectively) do not suffice to separate the three images of individual particles during one exposure of the camera. When particle velocities in the shock layer were determined the time intervals have been increased up to 2 μs and 4 μs, respectively.

Based on multi-exposure photographs as shown in Fig. 2.9 particle velocities have been calculated and the size and distribution of particles within the flow field have been determined. Let us estimate the error in velocity measurements. The time accuracy of light pulses was measured as 10 ns and can be negligible. The spatial resolution of the pictures depends on the magnitude of the optical system and was usually equal to 3 μm/pixel (e.g., in Fig. 2.9). Hence, assume that the error of determining the distance between two particle images to be 3 pixels. Thus, when light pulses as in Fig. 2.10 are used, we will determine the particle velocity with an accuracy of $\Delta u_p \sim 15$ m/s. In the case of a velocity of $u_p = 300$ m/s this corresponds to an error of 5%.

2.4.3 Visualization of the dynamics of shock waves

The motion of the shock wave ahead of the barrier has been detected by combining several light pulses with different time parameters. In order to observe the relatively slow motion of the shock wave, sequences of 5 pulses (duration: 100 ns) with time intervals betweens the pulses ranging from 2 to 10 μs were applied (Fig. 2.11). A typical shadowgraph image of the unsteady bow shock that was obtained with five light pulses, is shown in Fig. 2.12.
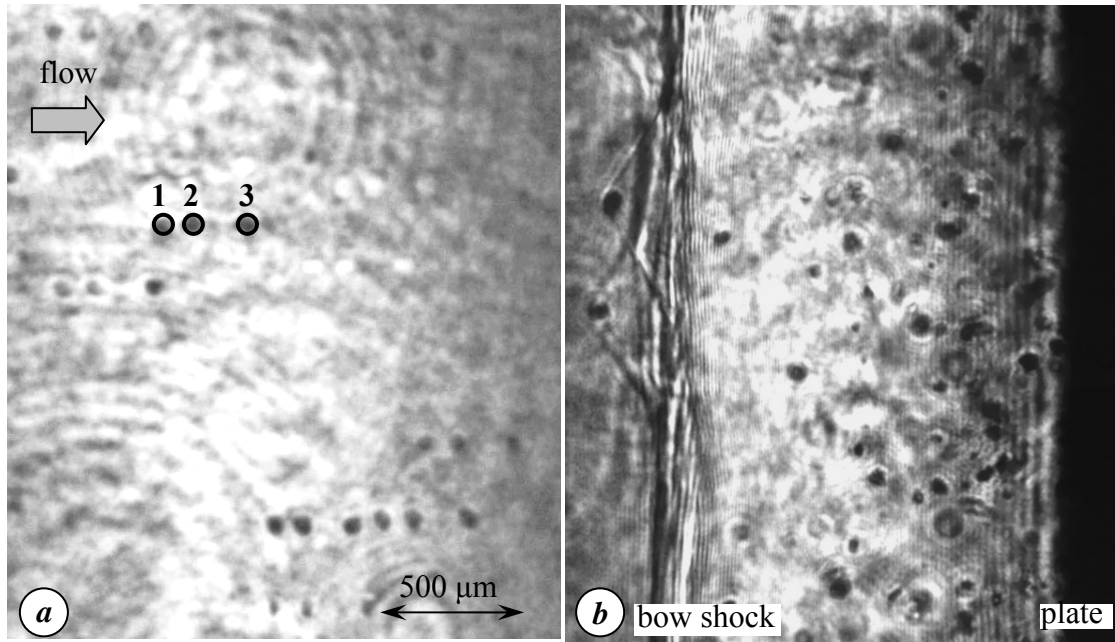
Fig. 2.9. Three-exposure shadowgraph images of particles (*a*) in a free jet and (*b*) within a shock layer.

Fig. 2.10. Sequence of three light pulses.

Fig. 2.11. Sequence of five light pulses.

Fig. 2.12. Five-exposure shadowgraph of an unsteady bow shock.
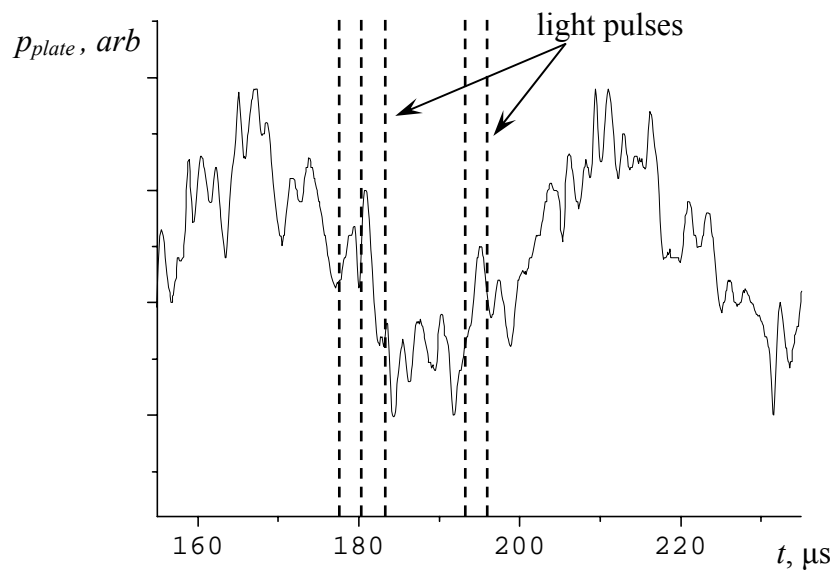
Fig. 2.13. Oscillogram of the pressure on the plate surface. Times coinciding with the five exposures of the corresponding shadowgraph picture have been marked by vertical lines. The plate pressure is shown in arbitrary units.

In the lower half of the photograph the five positions of the bow shock are enhanced by dotted lines. It can be seen that the b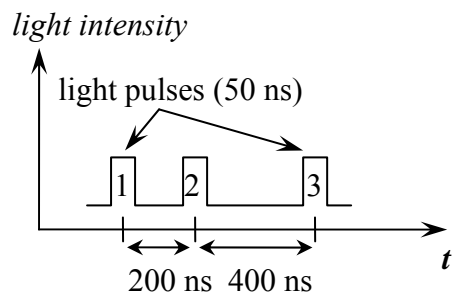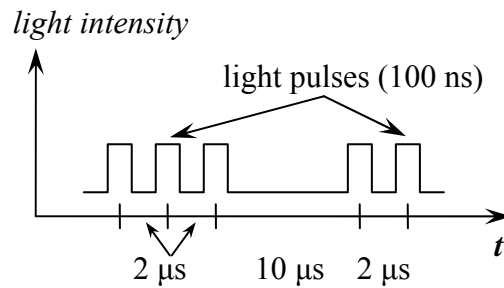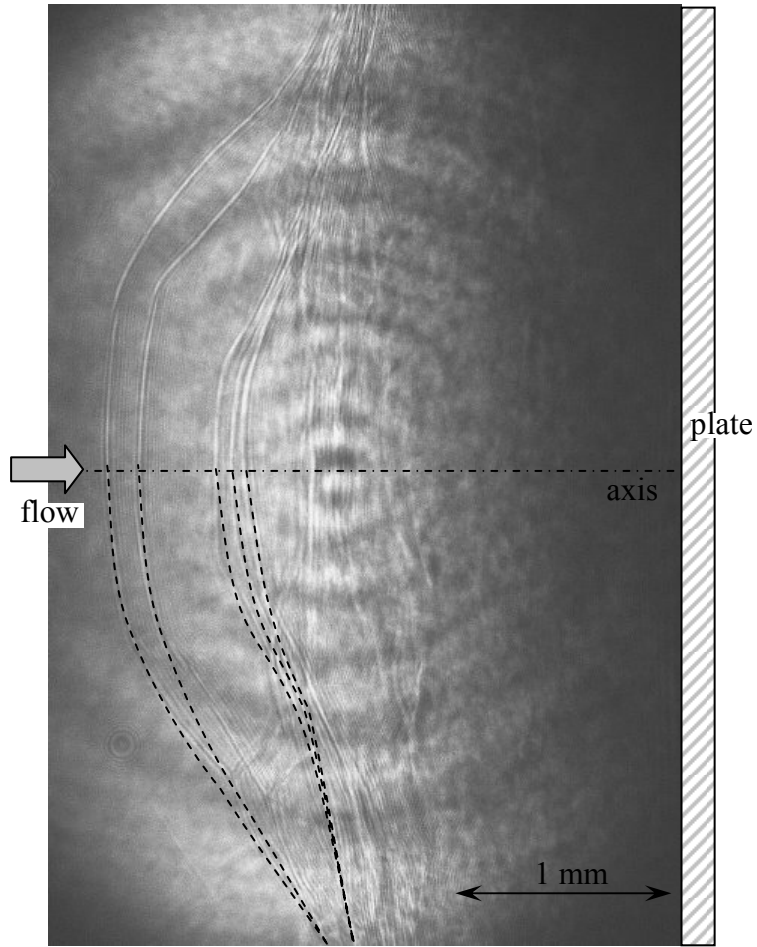ow shock moves away from the plate and changes its shape. These shock motions can have a profound influence on the flow field in the shock layer ahead of the plate. For obtaining a better understanding of processes in the shock layer pressure transients have been obtained on the surface of the plate. The high-speed pressure measurements were synchronized with five shadowgraph expositions, as shown in Fig. 2.11. In Fig. 2.13 an interval of the pressure oscillogram is shown. Times corresponding with the five light pulses of the shadowgraph (Fig. 2.11) are indicated by dashed lines. A combined analysis of multi-exposure photographs with synchronized pressure measurements will be presented in section 3.2.4.

3. Gas flow field in the impingement region

The subject of the present investigation is the interaction of supersonic jets and obstacles. This interaction depends on the properties of the jet and other parameters. Therefore, also supersonic free jets and the generation of such jets will be considered here.

When axisymmetric supersonic jets are formed by converging-diverging nozzles shock-cell structures are normally present in the jet flow. The shocks appear in the flow due to a non-ideally expansion of the gas by the nozzle. The jet flow is non-uniform along the jet axis as well as non-uniform in a cross-section of the jet. The character of irregularities of the jet flow depends on the conditions of jet formation: the degree of over-/underexpansion of the jet, the flow Mach number and the boundary layer formed in the nozzle.

The presence of shocks and irregularities of the jet flow has a strong influence on the character of interactions between the jet and an obstacle. Flow regimes of jet impingement depend also on the distance between the nozzle exit and the plate, the so-called nozzle-to-plate distance. When a supersonic jet impinges on an obstacle a region of gas with high pressure and temperature, a so-called shock layer, is formed ahead of the obstacle. The shock layer is separated from the upstream jet flow by a strong bow shock. This bow shock interacts with shocks located in the jet flow. Due to this interaction complicated shock structures are formed ahead of the obstacle. Furthermore, under certain conditions a recirculating flow can occur in the shock layer ahead of the plate. This changes the flow in the jet impingement region strongly.

Instabilities of the jet flow generate acoustic waves in the ambient air as well as an unsteadiness of the flow field in the shock layer ahead of the obstacle. An interaction between these instabilities can lead to self-sustained oscillations of the flow field. The complicated structure of the flow in the impingement region as well as changes in the jet structure as a function of the degree of over-/underexpansion, nozzle-to-plate distance and plate size has made it difficult to connect different features of the oscillating flow. In particular, the interaction between the unsteady flow field in the shock layer with the recirculation zone and with self-sustained oscillations in the impinging jet is not yet clear. These aspects are the topic of the present investigation.

In view of the above the investigation of processes occurring during the impingement of supersonic jets on an obstacle has been divided into three main parts. The first one relates to the properties of supersonic jets formed by nozzles. The second part concerns mean properties of the flow field which occurs ahead of the obstacle on which the supersonic jet impinges. The third object of this study is the unsteady behavior of flows at the jet impingement on an obstacle.

3.1 Supersonic free jets formed by axisymmetric nozzles

In the present work a conical axisymmetric nozzle with an extremely slender supersonic part was used. The ratio of the length l_{nozzle} of the diverging part to the exit radius r_e of the nozzle equals of $l_{nozzle} / r_e = 30$. Under these conditions the boundary layer formed on the nozzle wall has a strong influence on the jet issuing from the nozzle. In experiments the stagnation parameters of the gas were varied in a wide range. This

also resulted in significant changes in structure and parameters of the jet formed by the nozzle.

In the following sections a theoretical estimate of the influence of the boundary layer on the jet are obtained and a comparison with experimental data is provided. In addition, main features of shock structures that are present in non-ideally expanded jets are introduced und basics of the theory of interferences between shocks are given. Then, characteristics of over- and underexpanded jets that were both studied experimentally, are discussed.

3.1.1 Expansion of gas through slender axisymmetric supersonic nozzles

The basic equations of classical Laval-nozzle-theory can be obtained from any textbook on fluid dynamics [Abramovich 1963, Oswatitsch 1976, Landau & Lifshitz 1987] and analytical solutions are possible. In this theory the gas flow is assumed to be adiabatic, frictionless and one-dimensional. The fluid is approximated by a perfect gas with constant specific heats at constant pressure and volume, respectively, c_p and c_v. The gas parameters in the flow issuing from the nozzle are a function of the nozzle geometry (rather, of the ratio of the exit and critical cross-sectional areas S_e/S_{cr}), the stagnation gas temperature T_0 and the pressure p_0 (Fig. 3.1).
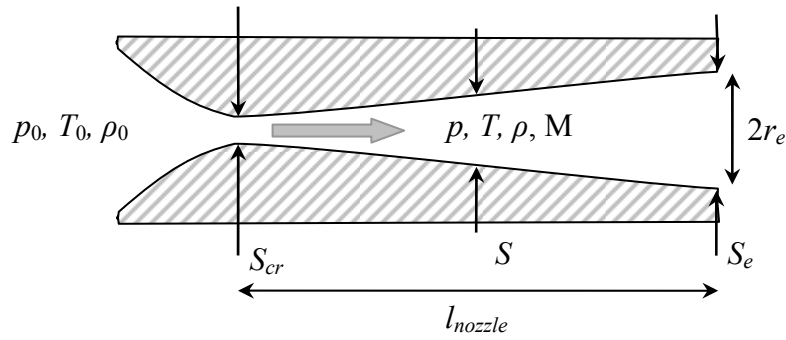

Fig. 3.1. Laval nozzle: notation.

The stagnation temperature and pressure of the gas can be measured in the reservoir ahead of the nozzle, where the gas is stagnant. As the gas is accelerated through the nozzle, temperature and pressure decrease from these values while the velocity increases. The gas parameters can be written as a function of the local Mach number M, $M = u/a$ where u and a are the local flow velocity and sound speed, respectively. The local Mach number and local cross-sectional area, normalized by the critical cross-sectional area, are related to each other. Thus the isentropic one-dimensional flow model provides a fundamental equation connecting the local flow Mach number with the area ratio:

$$\frac{S}{S_{cr}} = \frac{1}{M}\left(1 + \frac{\gamma-1}{2}M^2\right)^{\frac{\gamma+1}{2\gamma-2}}\left(\frac{\gamma+1}{2}\right)^{-\frac{\gamma+1}{2\gamma-2}}. \tag{3.1}$$

The main gas parameters are a function of the local flow Mach number and the stagnation values as follows:

$$\frac{T}{T_0} = \left(1 + \frac{\gamma-1}{2}M^2\right)^{-1} , \tag{3.2}$$

$$\frac{p}{p_0} = \left(\frac{T}{T_0}\right)^{\frac{\gamma}{\gamma-1}} , \quad \frac{\rho}{\rho_0} = \left(\frac{T}{T_0}\right)^{\frac{1}{\gamma-1}} , \quad \frac{a}{a_0} = \left(\frac{T}{T_0}\right)^{\frac{1}{2}} , \tag{3.3}$$

$$a = \sqrt{\gamma R T} . \tag{3.4}$$

Here, γ is the ratio of specific heats, $\gamma = c_p/c_v$, ρ is the density and R is the specific gas constant.

Let us consider the influence of different operating conditions of supersonic nozzles. For convenience we introduce a parameter $N = p_0/p_a$, i.e. the ratio of the stagnation pressure of the gas, p_0 , and the pressure of the ambient air, p_a , outside of the nozzle. In the framework of ideal gas theory simple analysis allows to define particular values of the ratio N. N_1 corresponds to the lowest value of N where the local sonic speed is reached at critical cross-section of the nozzle. For $N < N_1$ the flow within the whole nozzle is subsonic. The maximum value of the velocity is assumed in the critical cross-section. When N is increased to $N > N_1$, the flow is supersonic downstream of the nozzle throat and a normal shock appears in the diverging part of the nozzle terminating the supersonic part of the flow. The position of this shock depends on N and moves downstream towards the nozzle exit with increasing N (Fig. 3.2).

That value of N for which the normal shock reaches the exit edge of the nozzle is called N_2. In this case the flow is supersonic everywhere within the diverging part of the nozzle. A fully subsonic jet is formed behind the normal shock at the nozzle exit. When N is further increased ($N > N_2$) the distribution of the flow Mach number within the nozzle is no longer changed. But the static pressure p_e in the flow issuing from the nozzle exit changes. Furthermore, instead of a normal shock an oblique shock is formed at the nozzle exit (Fig. 3.3) and the flow field is no longer one-dimensional. For $N = N_3$, it changes into a weak discontinuity or a so-called Mach wave. The value N_3 corresponds to the case of an ideally expanded nozzle flow in which the ratio n of the static pressure in the supersonic flow at the nozzle exit and the ambient pressure is given by $n = p_e / p_a = 1$. For $N > N_3$ the jet is underexpanded ($n > 1$) and for $N < N_3$ it is overexpanded ($n < 1$). The parameter n will be called the off-design degree of the jet hereafter.

By considering the change of a normal shock into an oblique shock we pass already on to discussing two-dimensional flows issuing from the nozzle. In this connection let us consider the influence of multi-dimensional flows and of the viscosity of the gas on the gas expansion through nozzles. The one-dimensional inviscid theory ignores a radial variation of flow parameters, which depends on the geometry of the converging, critical and diverging parts of the nozzle. Any change in the curvature of the nozzle wall can lead to the formation of shocks in the flow. These shocks that are reflected from the axis of symmetry and from the wall of the nozzle can reach the shock at the exit of the nozzle. Furthermore, viscous effects in combination with a positive gradient of the pressure along the wall of the nozzle can result in a separation of the flow for low off-design degrees. Due to an interaction of shocks and flow separation oscillating flow fields can occur [Rein et al. 1988]. Under certain conditions, instead of a normal shock attached to the wall, so-called triple shock structures with an incident oblique shock which originates at the separation point at the nozzle wall, a reflected shock and a normal shock or Mach disk can be formed [Romine 1998]. All these

phenomena have an influence on the formation of the jet at the nozzle exit (Fig. 3.4). Further, the ideal gas theory ignores the displacement effect of the boundary layer formed along the nozzle wall. Thus, gas flow rates calculated by the model of a one-dimensional inviscid flow are higher than those obtained in practice.
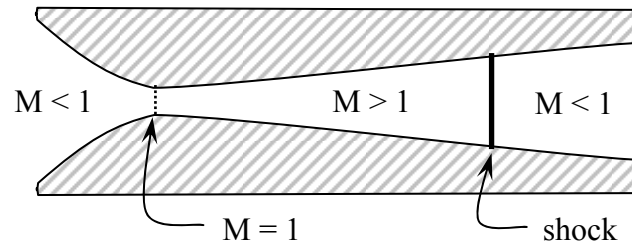
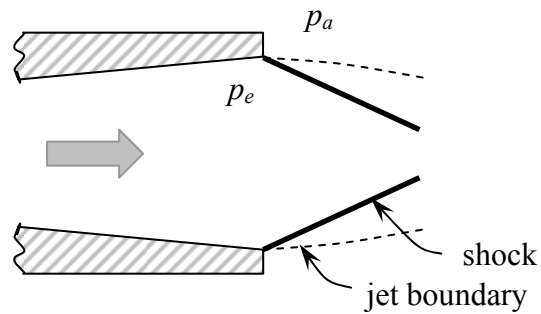Fig. 3.2. Basics of supersonic nozzle flows.
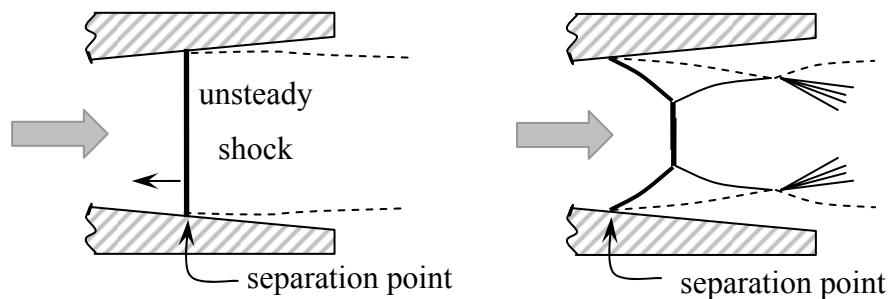
Fig. 3.3. Oblique nozzle shock.

Fig. 3.4. Flow separation in a nozzle (real flow conditions).

Although the presence of large pressure gradients and supersonic gas velocities renders a theoretical calculation of boundary layers in nozzles very difficult an approximate numerical analysis can be performed. For approximating boundary layers in supersonic nozzles numerical methods based on the following assumptions are used [Abramovich 1963, Schlichting 1978]:
- velocity and temperature profiles are similar to those in a developed turbulent boundary layer, the so-called "1/7 law" that is realized in boundary layers on flat plates or in free jets can be applied;
- local moment transfer is related to the thickness of the boundary layer as it in the case of turbulent boundary layers on plates;
- the flow outside of the boundary layer is calculated by one-dimensional, inviscid theory taking into account only the displacement thickness.

Important results of such computations that have been confirmed by experiments, are that the thickness δ of the boundary layer at the critical cross-section of the nozzle is negligibly small for usually applied shapes of the converging part of the nozzle and can be taken to be zero (Fig. 3.5).
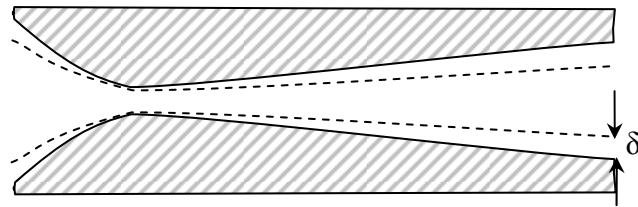

Fig. 3.5. Boundary layer in a nozzle.

Thus a simple estimate of boundary layer properties in nozzles will be based on the laws of turbulent boundary layers on flat plates in compressible flows. Under the assumption of a zero pressure gradient and no heat transfer across the surface the boundary layer (δ), displacement (δ_1) and momentum (δ_2) thicknesses are given by [Abramovich 1963, Schlichting 1978]:

$$\frac{\delta_2}{\delta} = 1 - \frac{\delta_1}{\delta} - 7\int_0^1 \frac{\zeta^8 d\zeta}{1 + 0.2\mathrm{M}^2(1 - \zeta^2)}, \qquad (3.5)$$

$$\frac{\delta_1}{\delta} = 1 - 7\int_0^1 \frac{\zeta^7 d\zeta}{1 + 0.2\mathrm{M}^2(1 - \zeta^2)}, \qquad (3.6)$$

$$\delta = x \cdot \frac{0.0575}{\mathrm{Re}_x^{0.2}} \cdot \left(\frac{\delta_2}{\delta}\right)^{-0.8} \cdot \frac{\left(1 + 0.2\mathrm{M}^2\right)^{0.6}}{\left(1 + 0.15\mathrm{M}^2\right)^{1.05}}, \qquad (3.7)$$

where the Reynolds number Re_x is defined by

$$\mathrm{Re}_x = x \cdot u \cdot \frac{\rho}{\mu}. \qquad (3.8)$$

Here, ζ is a formal parameter of integration; x is the distance from the critical cross-section (where the thickness of the boundary layer is assumed to be zero); u, ρ, μ are flow velocity, and density and dynamic viscosity of the gas at that point where the boundary layer thickness is to be calculated. All numerical coefficients are given for air. The viscosity μ depends on the temperature and can be approximated by Sutherland's equation:

$$\mu = \mu_0 \cdot \left(\frac{T}{T*} \right)^{\frac{3}{2}} \frac{T*+C}{T+C}, \tag{3.9}$$

where μ_0, $T*$ and C are constants (for air $\mu_0 = 1.72 \cdot 10^{-5}$ N·s/m², $T* = 273$ K, $C = 122$ K [Abramovich 1963]).

Expressions for turbulent boundary layers in incompressible flows can be obtained from eqs. 3.5 – 3.8 by substitution of M = 0. This yields:

$$\delta = x \cdot \frac{0.37}{\mathrm{Re}_x^{0.2}}, \qquad \frac{\delta_1}{\delta} = \frac{1}{8}. \tag{3.10}$$

In this manner estimates of the thickness of the boundary layer at the nozzle exit were obtained. For calculating Re_x the length of diverging part of the nozzle, l_{nozzle}, was used as the distance x, and the flow and gas parameters at the nozzle exit were taken.

3.1.2 Estimate of the influence of the boundary layer formed in the nozzle

The displacement thickness of the boundary layer at the nozzle exit calculated by the method described above is given in table 3.1 for the nozzle used in the experiments. As can be seen the thickness of the boundary layer is significant but the boundary layer does not reach the axis. Based on these results it is save to assume that the stagnation pressure p_0 in the core flow equals the one in the reservoir and the gas parameters vary in accordance with the laws of isentropic flow. The effect of the boundary layer is to decrease the effective cross-sectional area of the nozzle.

Thus Pitot-pressure measurements at the nozzle exit give the Mach number in the core flow (eq. 2.1). From the measured values of the flow Mach numbers we evaluated the effective ratio of cross-sectional areas $(S_e/S_{cr})_{eff}$ at the nozzle exit (eq. 3.1). Assuming that the effective throat area $(S_{cr})_{eff}$ is equal to the geometrical area because the boundary layer thickness is extremely small here, the effective area at the exit cross-section $(S_e)_{eff}$ has been calculated. With $(S_e)_{eff}$ determined in this manner the boundary-layer displacement thickness δ_1 at the nozzle exit becomes:

$$\delta_1 = \frac{\sqrt{S_e} - \sqrt{(S_e)_{eff}}}{\sqrt{\pi}}. \tag{3.11}$$

Properties of the boundary layer depend on the roughness of the surface of the nozzle wall. In the case of gas flows laden with solid particles the surface of the nozzle wall suffers damage from particle impacts (erosion) and after some time the surface of the wall that was initially smooth becomes rough. Also the long-term erosion leads to a progressive increase of the cross-sectional area of the diverging part of the nozzle.

The results of theoretical estimates and experimental measurements are summarized in a table 3.1. The theoretical values (1) of the flow Mach number M and pressure ratio N_3 for which the flow is ideally expanded, are calculated by inviscid one-dimensional theory. The parameters of the boundary layer were estimated for incompressible (2) and compressible (3) flows. Experimental results are presented for two states of the nozzle wall. First (4), a measurement was carried out with a new nozzle having smooth walls. Then, another measurement (5) was performed with the same nozzle after it had experienced a long-term exposure to erosion by particle impacts causing a roughing of the walls.

Table 3.1. The results of theoretical estimates and experimental measurements of parameters of nozzle flow.

	$(S_e/S_{cr})_{eff}$	M	N_3,	δ_1, mm	δ, mm
1. Inviscid theory (eq. 3.1)	4	2.94	33.6	-	-
2. Boundary layer estimate, incompressible flow (eq. 3.10)	3.63	2.84	-	0.15	1.26
3. Boundary layer estimate, compressible flow (eq. 3.7)	3.09	2.67	-	0.40	1.33
4. Polished wall, new nozzle (exp.)	3.15	2.69	22.9	0.37	1.2
5. Eroded wall (exp.)	3.43	2.78	26.3	0.25	0.8

As can be seen the influence of the boundary layer is significant. The flow Mach number predicted by frictionless theory is clearly overestimated: the predicted value of M = 2.94 (1) is 9% higher than the measured value of M = 2.69 (4). Already a simple approximation of the boundary layer gives results closer to the experimental value. The estimate of the boundary layer thickness obtained taking into account the compressibility of the gas gives an even better result (compare the displacement thickness δ_1 in cases 2, 3 and 4). The increase of the flow Mach number in case 5 (relative to case 4) can be explained by an increase of the cross-sectional area of the nozzle rather than by a change of the properties of the boundary-layer. The throat of the nozzle remains smooth and only the diverging (supersonic) part of the nozzle becomes eroded. This confirms the explanation of an increase of the flow Mach number due to an increase of the cross-sectional area at the nozzle exit. All experimental results presented in the following chapters were obtained with the eroded nozzle wall, as in case 5.

3.1.3 Introduction to the theory of interferences between discontinuities

Prior to describing typical wave structures in supersonic jets it is useful to provide some basics of the theory of shock waves and other discontinuities as well as some specific nomenclature (for details see classical textbooks, e.g., Adrianov et al. 1995, Oswatitsch 1976, Landau & Lifshitz 1987). In gas-dynamics, discontinuities are defined as surfaces at which parameters of the flow or their derivatives have a jump. In stationary flows the gas can penetrate through a surface of discontinuity or move tangentially along it. The discontinuity is called *normal* or *tangential*, respectively. In supersonic flows three main classes of gas-dynamic discontinuities are possible: normal discontinuities or shocks (σ), tangential discontinuities (τ) or *slip lines*, and centers of rarefaction (expansion) waves (ω) can be distinguished. Based on the intensity of the discontinuities each class can be divided into finite and weak discontinuities.

First, shock waves will be considered. The theory of shocks is based on the conservation laws for mass, momentum and energy. When the change of a parameter Φ across a discontinuity, i.e., the difference of the value after ($\hat{\Phi}$) and ahead (Φ) of the discontinuity, is denoted by $[\Phi] = \hat{\Phi} - \Phi$, the conservation laws can be written as follows:

$$[\rho u_n] = 0, \quad [u_\tau] = 0,$$
$$[p + \rho u_n^2] = 0, \tag{3.12}$$
$$\left[\frac{u_n^2}{2} + h\right] = 0,$$

where u_τ and u_n are the tangential and normal component of the local flow velocity and h is the enthalpy.

The intensity J of a shock is usually defined as the ratio of the static pressure after and before the shock:

$$J = \frac{\hat{p}}{p} = (1 + \varepsilon)\left(\frac{u_n}{a}\right)^2 - \varepsilon, \quad \varepsilon = \frac{\gamma - 1}{\gamma + 1}, \tag{3.13}$$

where $\hat{p}$ and p are the static pressures in the flow behind and ahead of the shock, respectively, and a is the local sound speed (Fig. 3.6). For steady shocks having an angle θ of inclination to the vector of the velocity $\vec{u}$ of the oncoming flow:

$$J = (1 + \varepsilon)\mathrm{M}^2 (\sin\theta)^2 - \varepsilon, \tag{3.14}$$

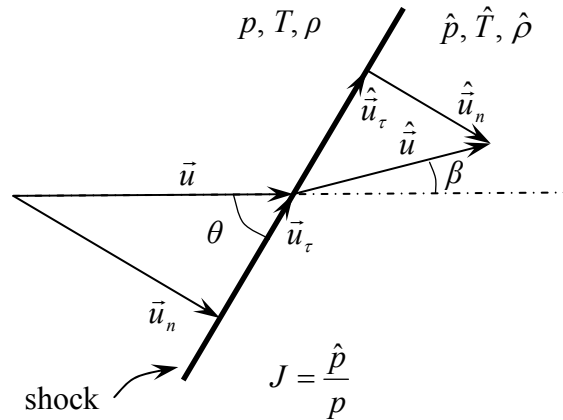where M is the local flow Mach number ahead of the shock.

Fig. 3.6. Oblique shock: notation.

The following equations that can be obtained from the conservation equations, relate the intensity of the shock and other parameters of the flow and will be used hereafter:

Intensity of a normal shock: $\qquad J_n = (1 + \varepsilon)\mathrm{M}^2 - \varepsilon$; $\qquad\qquad$ (3.15)

Ratio of densities: $\qquad\qquad\qquad E = \dfrac{\hat{\rho}}{\rho} = \dfrac{J + \varepsilon}{1 + \varepsilon J}$; $\qquad\qquad$ (3.16)

Ratio of enthalpies and temperatures: $\qquad H = \dfrac{\hat{h}}{h} = \dfrac{\hat{T}}{T} = \dfrac{J}{E}$; $\qquad\qquad$ (3.17)

Ratio of stagnation pressures: $\qquad\qquad I = \dfrac{\hat{p}_0}{p_0} = \left(J E^{-\gamma}\right)^{\frac{\varepsilon - 1}{2\varepsilon}}$; $\qquad\qquad$ (3.18)

Angle of flow deflection, β, at the shock: $\tan\beta = \sqrt{\eta}\,\dfrac{E-1}{E\eta+1}$,   (3.19)

where $\eta = (\cot\theta)^2 = \dfrac{J_n - J}{J + \varepsilon}$.   (3.20)

Another discontinuity is the tangential discontinuity or slip line that is characterized by the normal component of flow velocity being zero on both sides of the discontinuity (Fig. 3.7). Thus, no fluid passes through a tangential discontinuity. The integral feature of slip lines is the formation of mixing layers which occurs due to the viscosity of the gas. At the point where the slip line originates, the thickness of the mixing layer is zero, and, theoretically, some parameters are discontinuous. Downstream of this point the thickness increases. In the mixing layer the values of parameters of the flow change continuously from the values of the parameters on one side of the layer, to those on the other side.

Finally let us consider centered expansion waves. An isentropic expansion of a gas does not occur stepwise, but continuously within a certain spatial interval. The expansion wave can be described as an infinite number of infinitesimal expansion waves. A typical case where such rarefaction waves occur is the deflection of a supersonic flow at a corner (Fig. 3.8). In this case the flow becomes expanded and turned continuously within the centered expansion wave that is enclosed by the two characteristics $O_\omega A$ and $O_\omega B$. The point O_ω is the center of a rarefaction waves.

Classical theory provides the angle of the flow deflection, β_ω, caused by an isentropic rarefaction wave:

$$\beta_\omega = \omega(\hat{M}_\omega) - \omega(M),$$ (3.21)

where $\omega(M)$ is the Prandtl-Meyer function

$$\omega(M) = \frac{1}{\sqrt{\varepsilon}}\arctan\sqrt{\varepsilon(M^2-1)} - \arctan\sqrt{M^2-1},$$ (3.22)

and $\hat{M}_\omega$, the flow Mach number behind the wave, is given by:

$$\hat{M}_\omega = \frac{1}{\sqrt{\varepsilon}}\sqrt{(1+\varepsilon(M^2-1))J_\omega^{\frac{-2\varepsilon}{1+\varepsilon}} - 1 + \varepsilon},$$ (3.23)

where J_ω is the intensity of the expansion wave.

In complex flows discontinuities can interact with each other. The theory of interferences between discontinuities distinguishes numerous possibilities of such interactions. We consider only the interaction of shocks between each other or of shocks with a tangential discontinuity. The shock interactions can be divided into two classes: regular and irregular interactions.

Regular interactions, shock-shock or shock-tangential discontinuities, can be represented in a general manner (Fig. 3.9). At the intersection of two incident shocks, σ_1 and σ_2, two reflected shocks, σ_3 and σ_4, are formed. These shocks have different directions. The flow field between the reflected shocks is divided by a contact discontinuity τ, which originates at the intersection. Such interferences can be written by the conventional expression:

$$\sigma_1, \sigma_2 \rightarrow \sigma_4, \tau, \sigma_3.$$

In a similar manner the refraction of a shock σ_1 at a tangential discontinuity τ can be expressed as:

$$\sigma_1, \tau_1 \rightarrow \sigma_4, \tau_2, r_3.$$

Depending on the values of the flow Mach number on both sides of the tangential discontinuity τ_1 and on the intensity of shock σ_1, the reflected discontinuity r_3 can be a shock σ_3 or a centered rarefaction wave ω_3 (Fig. 3.9).
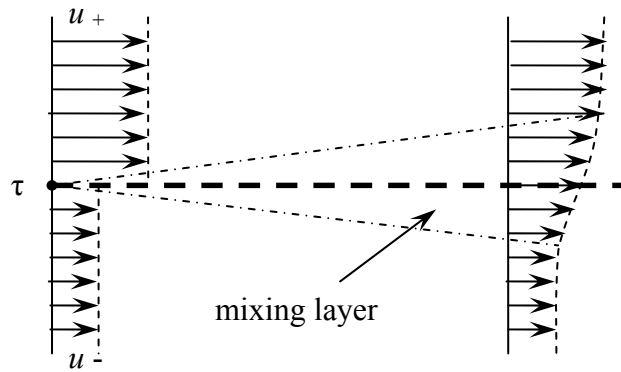

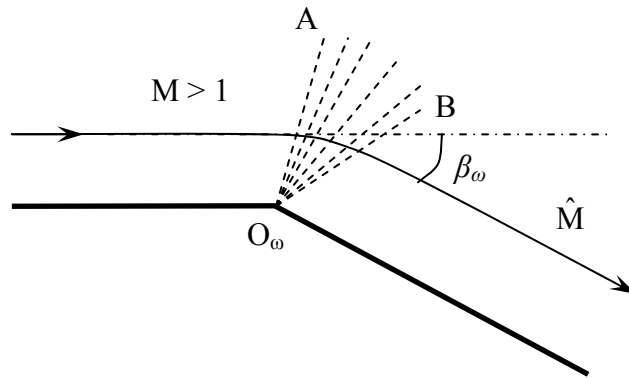Fig. 3.7. Tangential discontinuity: notation.

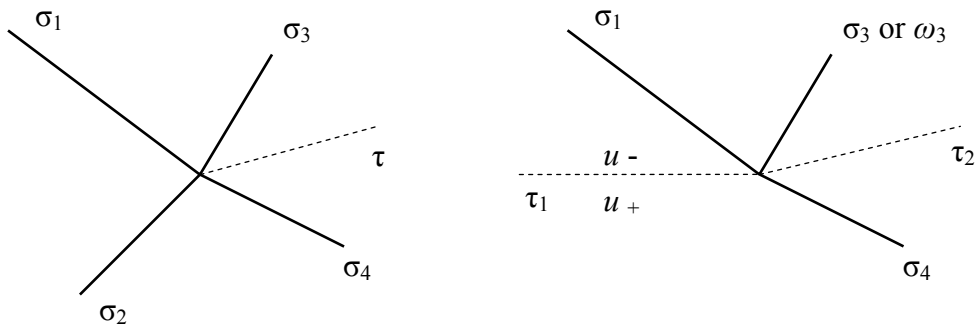Fig. 3.8. Flow deflection by a centered rarefaction wave.

Fig. 3.9. Regular interactions: interference of shocks (left) and of a shock and a tangential discontinuity (right).

Characteristic features of irregular interferences, so-called Mach reflections, are the formation of triple shock structures (Fig. 3.10) [Henderson & Menikoff 1998, Hornung 1986]. A Mach reflection results in a triple shock structure consisting of the incident shock σ_i, the main shock σ_m and the reflected shock σ_r. In addition, a tangential discontinuity τ is formed after the intersection of the shocks, between the shocks σ_m and σ_r. Such structures are formed in the case of an irregular reflection of shock waves at a rigid wall or at an axis of flow symmetry. In particular, within supersonic non-ideally expanded jets, a triple shock structure is formed with a so-called Mach disk as the main shock.

As can be seen in all cases of shock interactions, a contact discontinuity τ which originates at the intersection is present. In general the solution of problems with shock interactions is based on finding dynamic consistency conditions at the discontinuity τ, i.e., equality of static pressure and collinearity of velocity vectors on each side of the contact discontinuity [Adrianov et al. 1995]. Let us consider this for the example of a triple shock structure. It is assumed that the parameters of the incident shock σ_i are known. In this case finding the parameters of the main shock σ_m and the reflected shock σ_r results in the solution of the equations:

$$\begin{cases} J_m = J_i \cdot J_r \\ |\beta_m| = |\beta_r - \beta_i| \end{cases}, \tag{3.24}$$

where J is a shock intensity and β is an angle of flow deflection at the corresponding shock. Note that the conditions of the existence of a triple shock structure has not been considered.

3.1.4 Basics of supersonic over- and underexpanded jets

The classical theory of shock wave interferences allows to approximate flow parameters as well as shock curvatures and positions in supersonic jets [Adrianov et al. 1995, Rist 1996]. In the following, we will consider the main features of overexpanded ($n < 1$) and underexpanded ($n > 1$) axisymmetric jets.

First, let us consider overexpanded jets. Then, the degree of off-design is less than one ($n < 1$). Increasing the degree of off-design, $n \rightarrow 1$, results in decreasing the intensity $J_e = \dfrac{p_a}{p_e} = \dfrac{1}{n}$ of the nozzle shock that is formed at the edge of the nozzle exit,. According to eq. 3.14, the angle of inclination θ_e of the nozzle shock is also decreased. In Fig. 3.11 the angle β of flow deflection by the nozzle shock (calculated using eqs. 3.15-3.20) is shown as a function of the shock intensity for $M = 2.78$ and $\gamma = 1.4$. As mentioned above for real gases there exists a limiting value n_l of the off-design degree, so that for $n < n_l < 1$ the flow separates from the nozzle wall upstream of the exit and inviscid theory does not work anymore. For the nozzle used in the present work $n_l \approx 0.5$ was determined experimentally. At the edge of the nozzle exit, right after the nozzle shock, the angle of inclination of the jet boundary with respect to the axis is given by $\alpha = \alpha_e - \beta$, where α_e is the angle ahead of the shock which equals the half-angle of the conical nozzle. Depending on α_e, n and M this angle can be both positive and negative.

Because the flow is axisymmetric, i.e., essentially two-dimensional, the intensity of the nozzle shock has to change with distance from the nozzle edge. The shock is not straight, but has some curvature. It is known [Adrianov et al. 1995], that for $n < 1$ and

$M_e > 2$ the curvature of the nozzle shock is negative, i.e., the intensity of the shock increases from the nozzle edge to the axis.
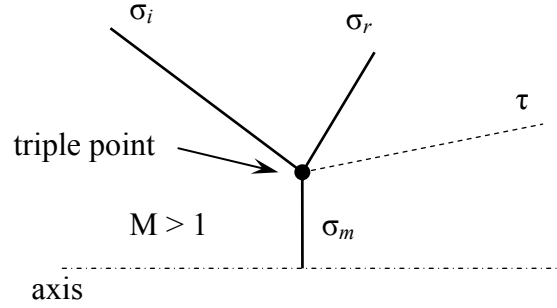

Fig. 3.10. Irregular reflection: Mach reflection at a line of symmetry.
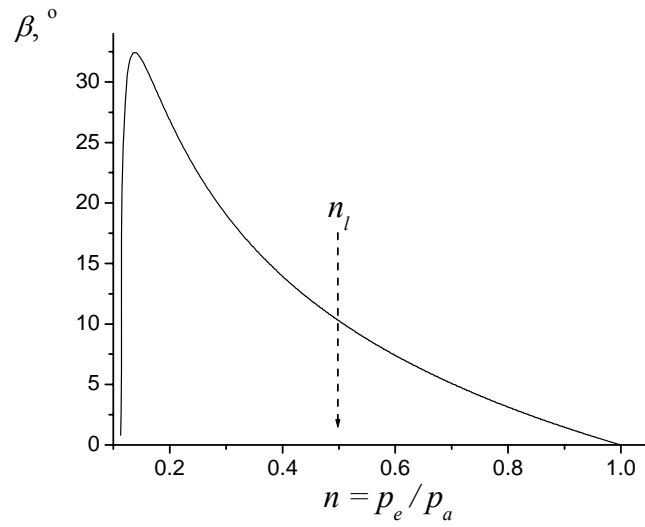

Fig. 3.11. Flow deflection by the nozzle shock versus off-design degree. For $n < n_l$ shock induced flow separation was observed in the conical nozzle used.
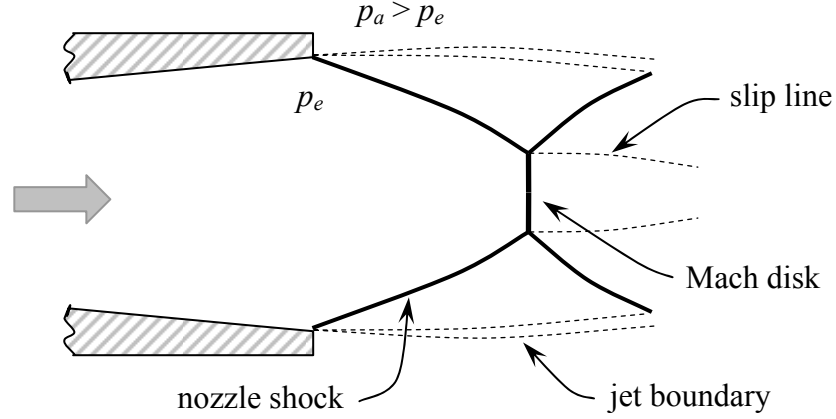
Fig. 3.12. Overexpanded outflow from a supersonic nozzle.

On the boundary of the jet the gas-dynamic parameters are constant and equal the ones in the ambient air. Because the intensity of the nozzle shock varies between the nozzle edge and the axis of the jet the flow behind the shock is non-isentropic. At the jet axis the intensity of the shock becomes so great that a regular reflection is not possible. Therefore an irregular reflection with a triple point and a Mach disk is formed (Fig. 3.12).

Now let us consider ideally expanded jets ($n = 1$) and underexpanded jets ($n > 1$). At first sight, in these cases there are no reasons for the formation of compression shocks directly at the edge of the nozzle. For $n = 1$ only a weak discontinuity (Mach wave) with intensity $J_e = 1$ leaves the edge. For $n > 1$ a centered rarefaction wave is formed. Its intensity is given by $J_\omega = 1/n$, and the flow is turned outward by an angle β_ω that is defined by eq. 3.21. Thus, the cross-sectional area of the jet increases downstream of the nozzle exit and reaches a maximum some distance downstream of the exit. In this case the curvature of the jet boundary is negative. Theory predicts a negative curvature of the boundary of the jet also for the case of an ideal expansion ($n = 1$). In the case of axisymmetric nozzles the curvature K_e of the jet boundary can be determined analytically [Adrianov et al. 1995, Omel'chenko et al. 2003]:

$$K_e = -\frac{4\sin(\alpha_e)}{2r_e\sqrt{M_e^2 - 1}} . \tag{3.25}$$

Hence, for conical nozzles ($\alpha_e > 0$) the curvature is negative.

In order to explain the formation of nozzle shocks in underexpanded jets ($n > 1$) it is necessary to account for the non-uniform flow in the boundary layer. The continuous shear layer can be represented by a continuous distribution of infinitesimal entropy discontinuities or slip surfaces. Weak discontinuities (such as expansion waves) propagating through such layers are partially reflected at every infinitesimal discontinuity. The reflected waves are again reflected at the free boundary of the jet. At the boundary of the jet a negative curvature in combination with a constant static pressure results in an intersection of these reflected characteristics originating at the jet boundary. For the flow Mach numbers $M_e > \sqrt{2}$ the characteristics are weak compression waves [Weinbaum 1966]. This is the reason for the formation of a separated shock near the edge of the nozzle (cf. inset in Fig. 3.13). The behavior of this shock is similar to the one in overexpanded jets.
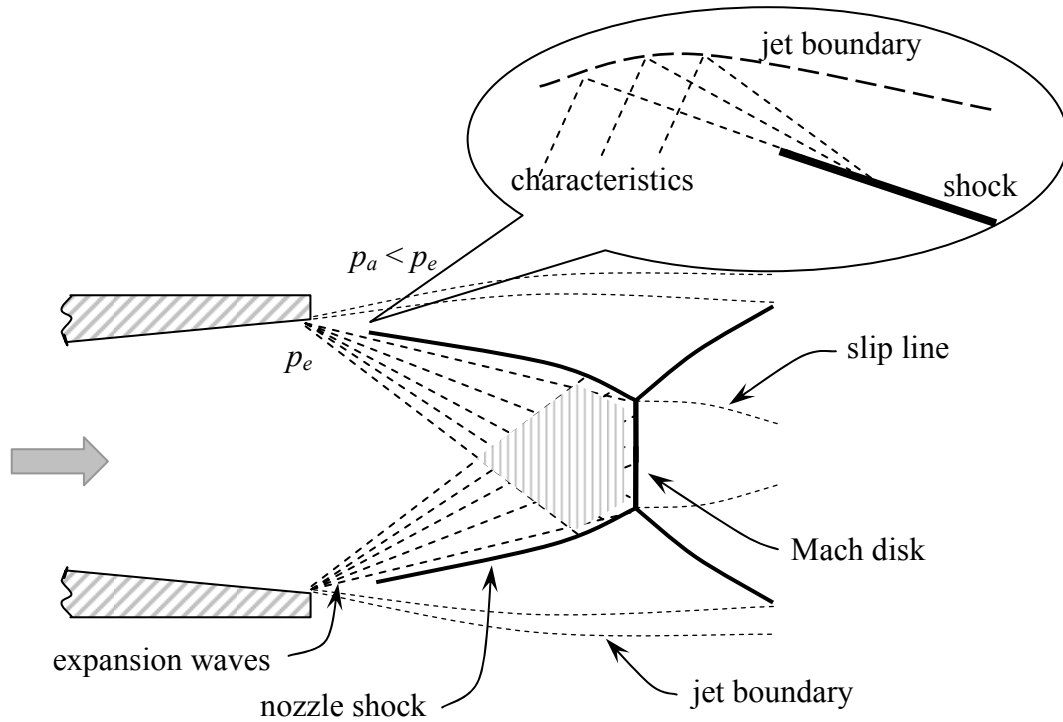
Fig. 3.13. Underexpanded outflow from a supersonic nozzle.
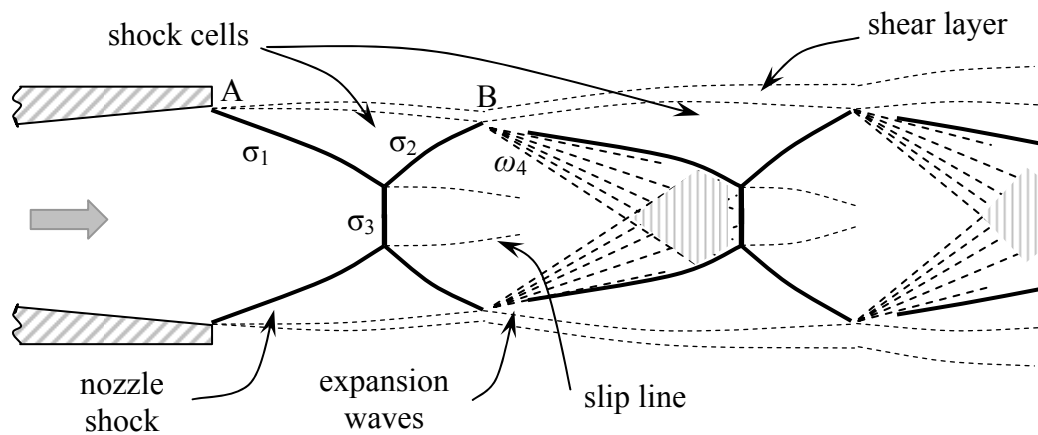
Fig. 3.14. Overexpanded supersonic jet.

According to the last discussion in supersonic axisymmetric jets formed by conical nozzles an oblique shock beginning near the nozzle edge and extending to the axis is always present (Fig. 3.14). This shock σ_1, the so-called *nozzle shock*, is reflected irregularly from the axis of symmetry and a triple shock structure is formed. The flow is supersonic behind the reflected shock σ_2 and subsonic behind the Mach disk σ_3. When the shock wave σ_2 reaches the jet boundary AB, a centered rarefaction wave ω_4 is formed at point B. The situation that is present at the nozzle exit in the case of

underexpanded jets is repeated with the formation of an oblique shock and its irregular reflection from the axis of the jet. The flow region between two consequent shock intersections is called a *barrel* or *shock cell* of the jet.

The periodic shock structure of supersonic jets results in alternate regions of acceleration and deceleration of the gas. For instance, let us consider an overexpanded supersonic jet as in Fig. 3.14. After the nozzle shock the flow is deflected to the axis of the jet. The gas becomes somewhat compressed and the velocity decreases slightly. At the nozzle exit the flow is supersonic near the axis and experiences acceleration until the Mach disk is reached. Behind the Mach disk the flow is subsonic. However, gas that passes through the two oblique shocks, σ_1 and σ_2, waves remains at a supersonic velocity. By passing through the oblique shocks it obtains a positive radial component of velocity. This leads to a repeated expansion of the gas. Between the central subsonic region behind the Mach disk and the peripheral region a mixing layer is formed. A momentum transfers from the outer to the central part of the jet causes an acceleration of the gas near the axis up to supersonic velocities. In passing through the shocks the total pressure of the gas is reduced. Therefore, the second shock cell is weaker than first one (reduced degree of overexpansion, reduced intensity of the Mach disk). Thus the shock intensities decrease from barrel to barrel until the static pressure in the jet becomes equal to the ambient pressure and the flow becomes shockless. The kinetic energy of the gas is dissipated due to a mixing of the gas in the jet with still ambient gas. The length of the core region of the jet, where the flow at the jet axis does not experience of an influence of the ambient gas, depends on the off-design degree n and can be up to $60\,r_e$ (r_e: radius of the nozzle exit). In the following we will study the impingement of jets on plates. The distance between the plate and the nozzle edge is always less than $20\,r_e$. Then, the interaction of the jet with the plate is strongly influenced by the transonic core region.
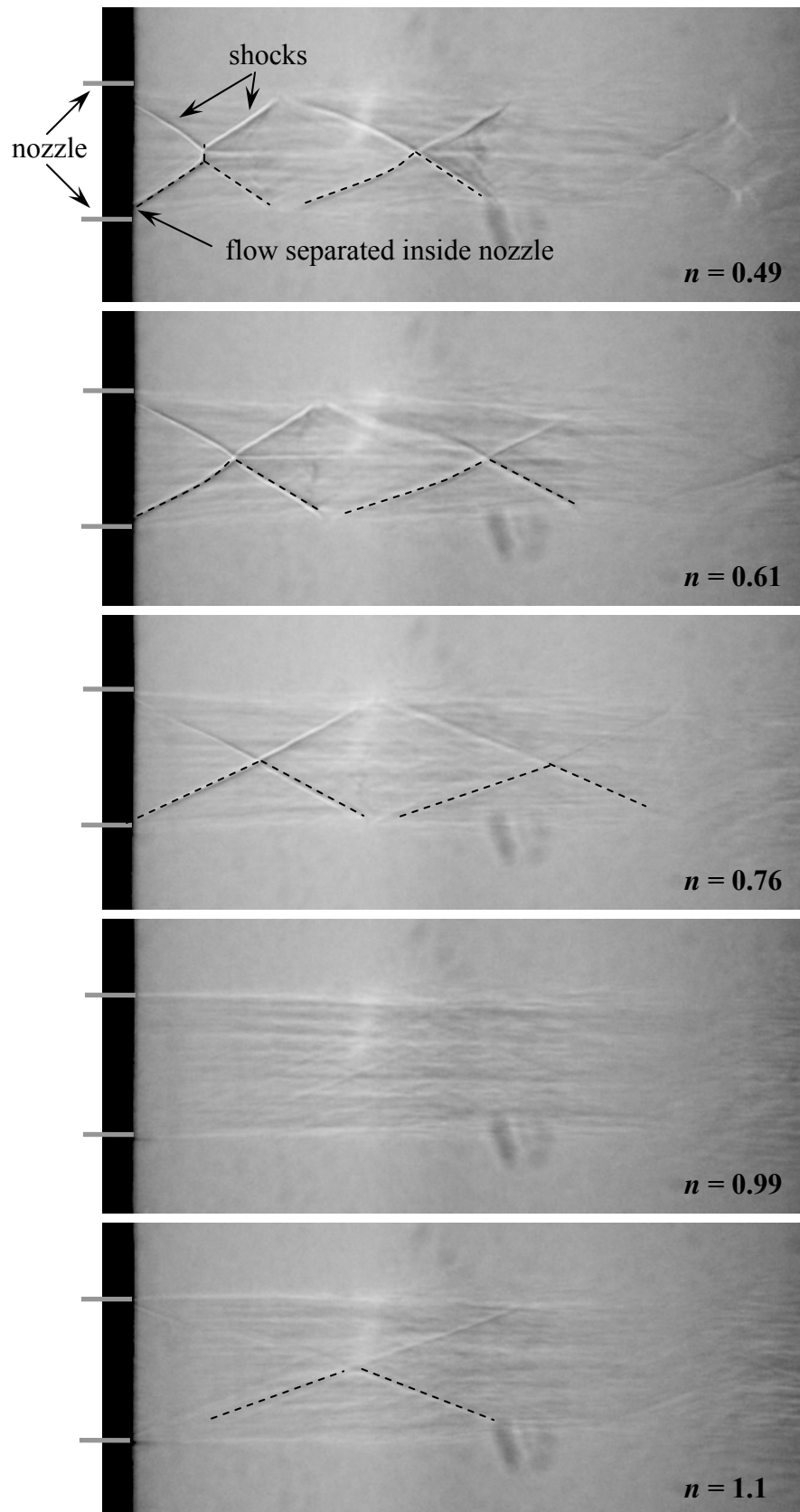
Fig. 3.15. Shadowgraph pictures of a supersonic free jet emanating from a conical nozzle for different off-design degrees *n*. In the lower part of the pictures shock structures have been enhanced by dashed lines.

The cellular, almost periodic structure of supersonic free jets represents their most prominent feature. Commonly, the spatial distance between two subsequent shock reflections at the jet boundary is called the "wavelength" of a free jet. In Fig. 3.15 typical shadowgraphs of supersonic free jets with a flow Mach number of $M_e = 2.78$ at the nozzle exit are shown for different off-design degrees n. The characteristic shock structures, the so-called "diamond patterns", are clearly visible. Based on such pictures the locations x_b of shock reflections at the axis have been determined for jets formed by the nozzle used in the present experiments. The distance between two subsequent shock reflections, $l_{b,i} = x_{b,i+1} - x_{b,i}$, corresponds to the "wavelength" defined above.
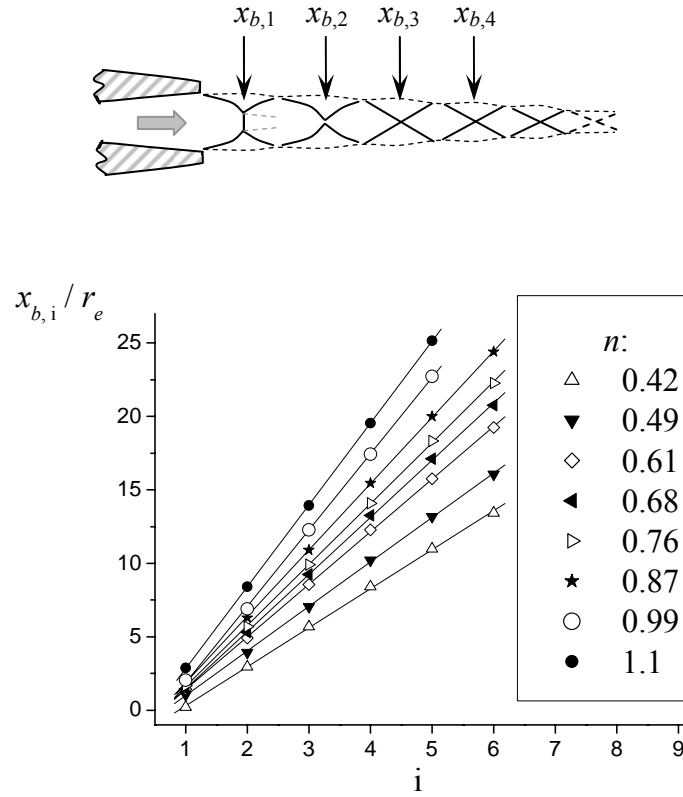
Fig. 3.16. Positions of the shock reflections $x_{b,i}$ for different off-design degrees n. Index $i = 1$ corresponds to the first reflection behind the nozzle exit.
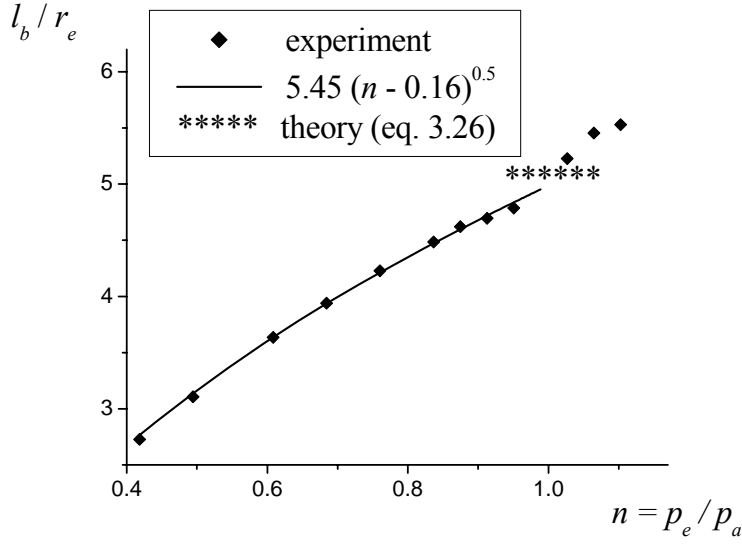
40

Fig. 3.17. Wavelength l_b as a function of n: experimental values (diamonds) and approximation by a $n^{0.5}$ law in the range of overexpanded jets ($n < 1$), (solid line).

In Fig. 3.16 the locations of shock reflections, x_b, are represented for different degrees of off-design n. As can be seen the experimental data are well approximated by straight lines. Hence, for the jet parameters considered here it may be assumed that the distance between two subsequent shock reflections does not depend on the distance from the nozzle edge. The "wavelength" l_b depends only on the off-design degree n of the jet. In Fig. 3.17 the wavelength l_b, scaled by the radius of the nozzle exit r_e, is shown as a function of the off-design degree n.

It has been considered [Pack 1948] that the wavelength of a free jet depends on the degree of overexpansion as $n^{0.5}$. In Fig. 3.17 a good agreement of experimental data with a $n^{0.5}$ law is found. Also, in the figure a theoretically predicted value of the wavelength of an ideally expanded jet is shown by a line formed by asterisks. The corrected version [Dillmann 1994, 1995] of Pack's formula for the wavelength of a supersonic free jet was used:

$$l_b = 2r_e \sqrt{M_{id}^2 - 1},$$ (3.26)

where M_{id} is the flow Mach number of an ideally expanded jet.

The periodic structure of supersonic free jets is also well observed in Pitot-pressure measurements. In Fig. 3.18 profiles of the Pitot-pressure measured along the axis of jets are shown for different off-design degrees n. The measured pressure is normalized by the reservoir pressure. Irregularities in the profiles indicate the non-uniform distribution of flow parameters in the jet as well as the positions of shocks in the flow.

Let us consider the example of an overexpanded jet (Fig. 3.18, $n = 0.76$). Downstream of the nozzle exit the Pitot-pressure decreases slightly because the flow that is somewhat conical is accelerating until the Mach disk is reached. As noted above a short subsonic zone is formed behind the Mach disk. Downstream of this zone a momentum transfers from the outer region of the jet, where the total pressure is greater than behind the Mach disk, to the central part of the jet occurs and the flow is again accelerated up to supersonic velocities. The pressure rise corresponds to the distance $x \sim 2r_e$ from the nozzle exit where the Pitot-tube is in the supersonic region behind the subsonic zone. A bow shock is formed ahead of the Pitot-tube, but the flow Mach number is low yet and the total pressure loss due to the shock is not great. The abrupt character of the pressure rise is conditioned by the relatively big opening of the Pitot-tube which is larger than area of the Mach disk. Thus, when the tip of the Pitot-tube is downstream of the Mach disk but is close enough to one, the bow shock ahead of the Pitot-tube and the Mach disk are combined into one shock structure. The Pitot-pressure in this case is equal to the one in the supersonic flow upstream of the Mach disk. The situation is changed abruptly when the Pitot-tube is moved far enough from the Mach disk and in the flow the bow shock ahead of the Pitot-tube and Mach disk can exist separately. In this case the flow ahead of the bow shock is supersonic but the flow Mach number is low yet and the total pressure loss due to the shock is not great. Estimates show that the peak of Pitot-pressure corresponds to the flow Mach number of 2.

With increasing distance from the nozzle, from $x = 2r_e$ to $x = 5r_e$, the flow Mach number increases along the axis and, correspondingly, the Pitot-pressure decreases. Before reaching the next point of the interaction of shocks on the jet axis the Pitot-tube comes through the region of the increased flow Mach number that is formed by the expansion waves that are reflected from the jet boundary. For such regions ($x = 4.5$-$5r_e$) a strongly decreasing Pitot-pressure is characteristic. This behavior of the pressure is repeated in every jet barrel until the flow becomes fully subsonic.

A similar behavior of the Pitot-pressure is observed in the case of underexpanded jets. The only difference is the presence of expansion waves within the first shock cell of the underexpanded jet. This can be seen in the Pitot-pressure profiles.

Radial profiles of the Pitot-pressure can be analyzed in the same manner. We note only main features. In Fig. 3.19 radial profiles of the Pitot-pressure measured in a free jet having a degree of off-design of $n = 0.99$ are presented. Data are compared at different cross sections: at the nozzle exit ($x \approx 0$) and in the far-zone ($x = 22$-$32r_e$) of the jet where the flow is shockless. In Fig. 3.20-3.21 radial profiles of the Pitot-pressure of overexpanded ($n = 0.76$) and underexpanded ($n = 1.1$) jets are shown. The distance from the nozzle exit, at which radial profiles were measured, are marked in the axial-profile of the pressure that is also included in the figures. An intersection of the bow shock ahead of the Pitot-tube and a shock wave of the jet results in a local increase of the pressure in the radial profile [Kalghatgi & Hunt 1976] see, e.g. Fig. 3.20*f, g*. Similarly, expansion waves appear in the profile as a local decrease in the Pitot-pressure, e.g. in Fig. 3.20*k, l*. A small decrease of the Pitot-pressure at the center of the radial profile corresponds to the mixing region behind the Mach disks (e.g. in Fig. 3.20*i, j*). In this region the flow that passed through the plane Mach shock has a smaller total pressure.
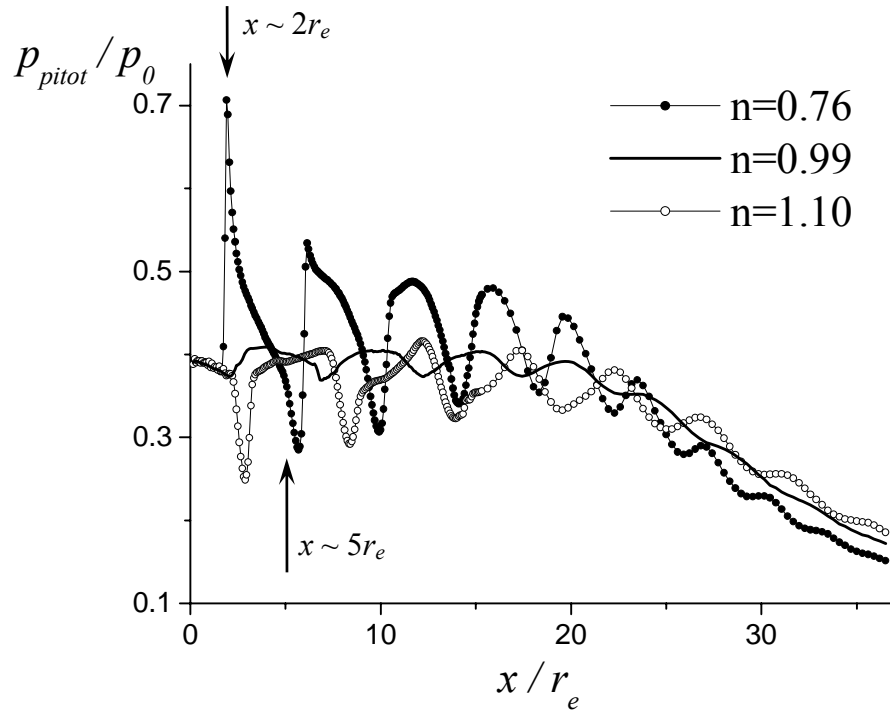
Fig. 3.18. Axial-profiles of the Pitot-pressure measured in free jets with different degree of off-design n.
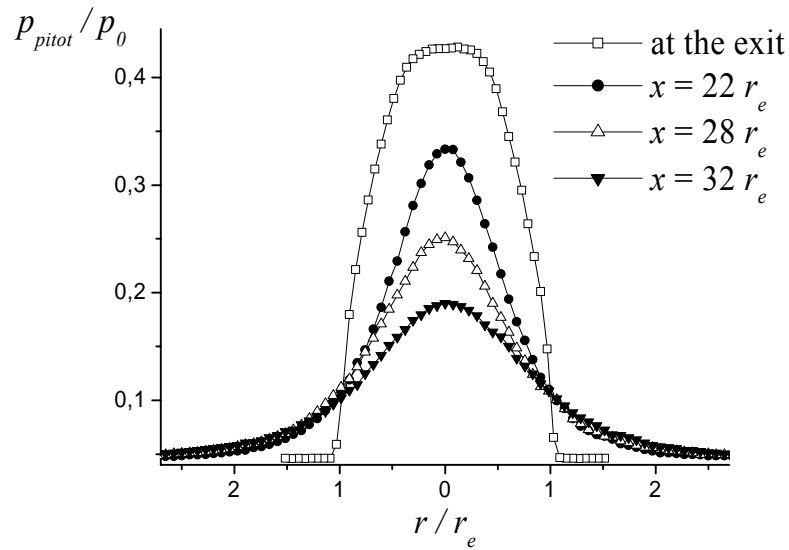
Fig. 3.19. Radial profiles of the Pitot-pressure at the nozzle exit and in the far-zone of a free jet ($n = 0.99$).
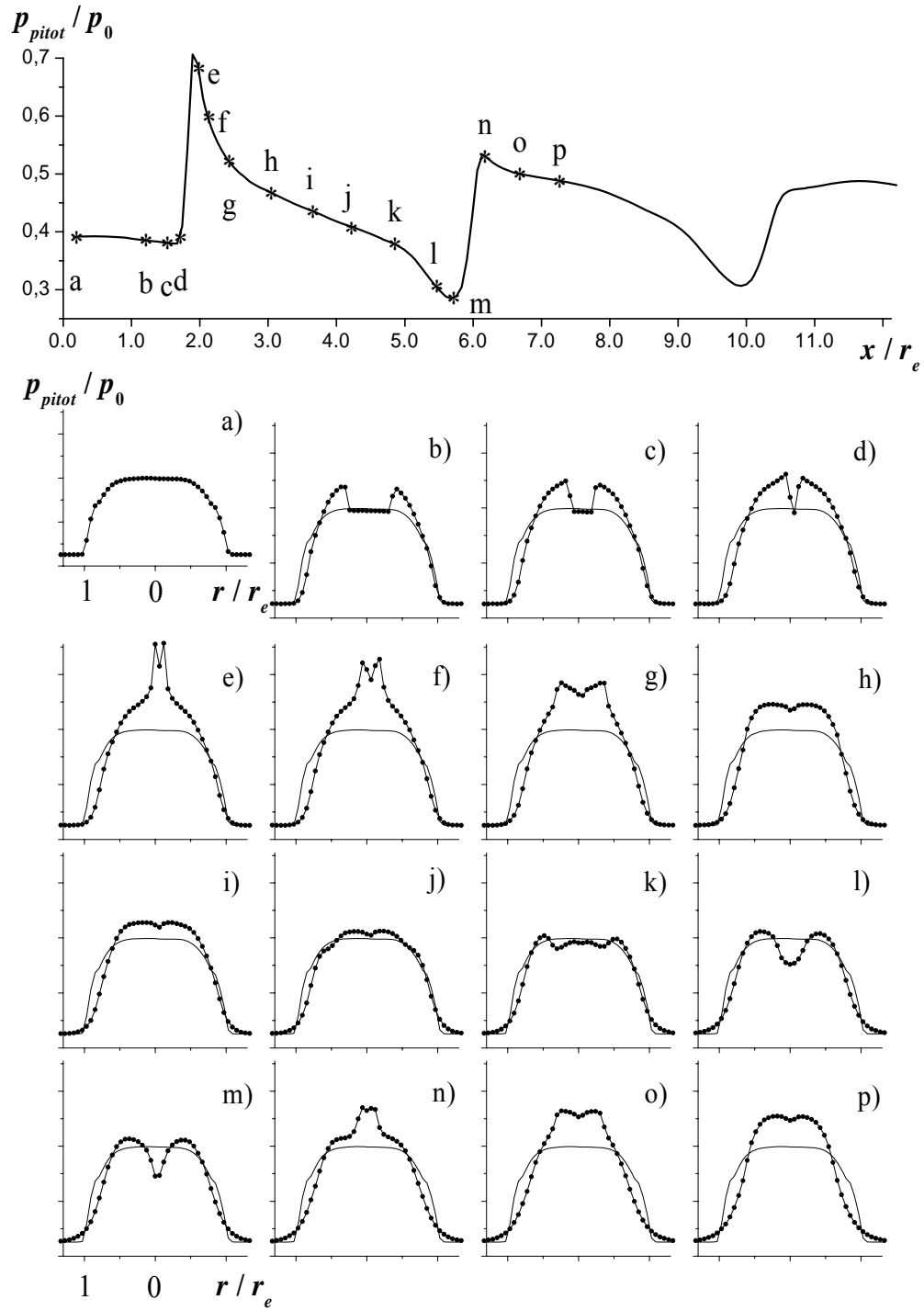
Fig. 3.20. Axial profile (top figure) and radial profiles (*a* - *p*) of the Pitot-pressure measured in a free jet having a degree of off-design of $n = 0.76$. In each figure (*a* - *p*) with radial profiles the radial distribution of the Pitot-pressure measured in the free jet at the nozzle exit is shown by a thin line. The axial locations of the radial profiles are depicted in the top figure.

44
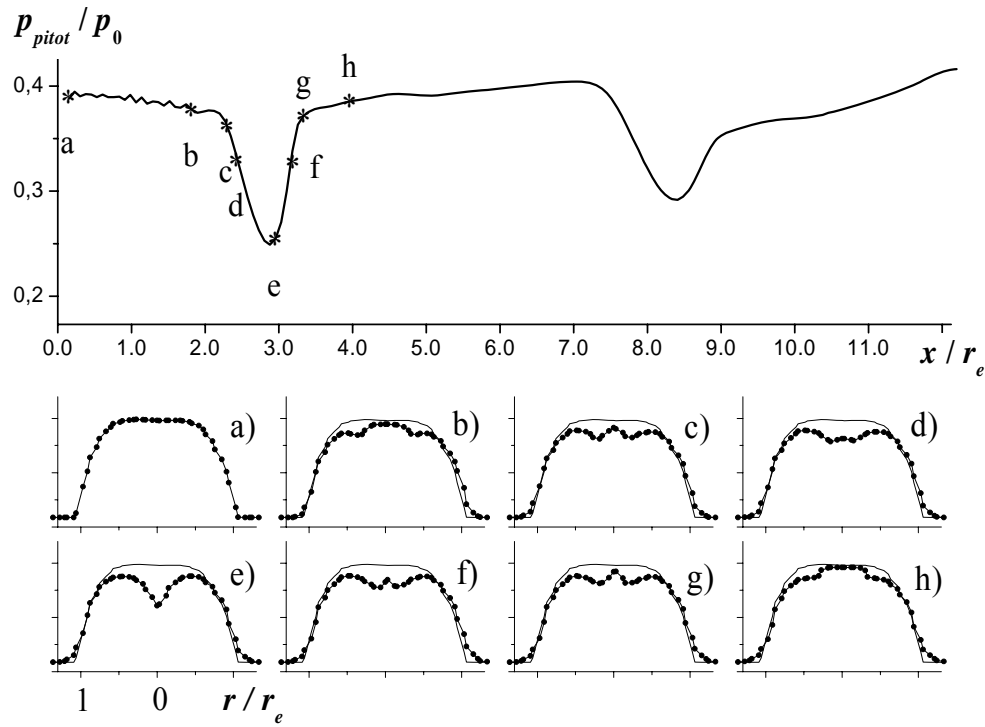
Fig. 3.21. Axial profile (top figure) and radial profiles (*a* - *h*) of the Pitot-pressure measured in a free jet having a degree of off-design of $n = 1.1$. In each figure (*b* - *h*) with radial profiles the radial distribution of the Pitot-pressure measured in the free jet at the nozzle exit is shown by a thin line. The axial locations of the radial profiles are depicted in the top figure.

As can be seen in Fig. 3.18-3.21 already small deviations of the off-design degree of the jet from $n = 1$ result in essential changes in the axial and radial distributions of flow parameters in the jet. Such non-uniformities of the jet have a strong influence on phenomena occurring during the impingement of a jet on an obstacle. Steady and, particularly, unsteady characteristics of jet impingement depend on the off-design degree of the jet and on the position of the obstacle relative to the "diamond structure" of the jet.

3.2 Perpendicular jet impingement on a flat plate

The character of the jet-plate interactions depends strongly on the shocks that are present in over- and underexpanded jets. Under certain conditions a flow field with a recirculation zone occurs in the shock layer ahead of the plate. As will be shown, flow fields with a recirculation zone can be highly unsteady. In the following sections a general description of the flow field in the impingement region is given. Special attention is laid on characteristics of jet impingements resulting in recirculating flows. Different regimes of supersonic jet impingement on a flat plate that were studied experimentally for steady as well as for unsteady cases are discussed.

3.2.1 General description of the flow field in the impingement region

The flow field in the region of interaction of a supersonic jet with a flat plate is characterized by the presence of complicated shock structures and supersonic and subsonic zones (Fig. 3.22). Schematically the impingement zone can be divided into three regions as follows: (1) the free jet upstream of any local interaction effects due to impingement; (2) the shock layer where the strong interaction of the jet with the plate surface produces a change in the flow direction; (3) the wall jet consisting of a radial flow along the surface beyond the point at which the strong interactions of impingement cause any local effects [Donaldson & Snedeker 1971]. These three regions can be considered separately, but they are not independent of each other. Although the free jet upstream of the stand-off shock ahead of the plate does not depend directly on phenomena in the shock layer it does so indirectly: through the shear layer at the jet boundary information about processes occurring in the impingement zone can be transferred upstream into the core of the free jet.

Due to the interaction of the jet with the plate a strong stand-off shock, a so-called plate shock, is formed ahead of the plate. Behind the plate shock the flow is subsonic. Due to a strong negative radial pressure gradient on the plate the flow is accelerated along the surface. Since the gas expands in radial direction the gas in the wall jet can reach supersonic velocities again. In this case the structure of the wall jet is similar to the one of free jets: periodical shock structures and supersonic/subsonic parts are present. At some distance from the center of impingement the wall jet becomes fully subsonic, as in the case of free jets. The essential difference between the wall jet and the free jet is a strong momentum loss due to friction at the wall.

An important quantity which can be measured in experiment is the pressure p_{plate} on the surface of the plate. That is called a *plate pressure* in the following. In Fig. 3.23 a typical distribution of the plate pressure in the impingement zone of a jet impinging perpendicularly onto a wall, is shown. The pressure has a maximum at the center. At a radial position that corresponds with the width of the jet ($r / r_e \sim 1.0$) it decreases strongly. In the wall jet region ($r / r_e > 1.5$) several pressure peaks are present because compression and expansion waves are formed alternately due to the repetitive reflection of waves from the boundary of the wall jet and from the plate in the wall jet region [Carling & Hunt 1974].
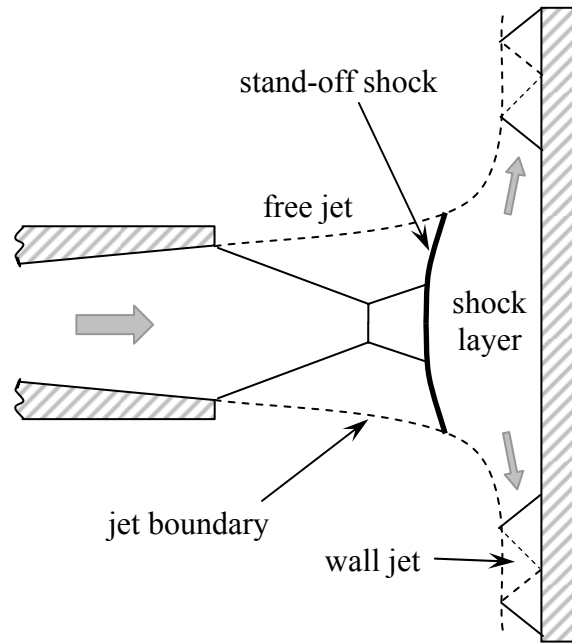
Fig. 3.22. Sketch of the flow field in the impingement region of a supersonic jet.
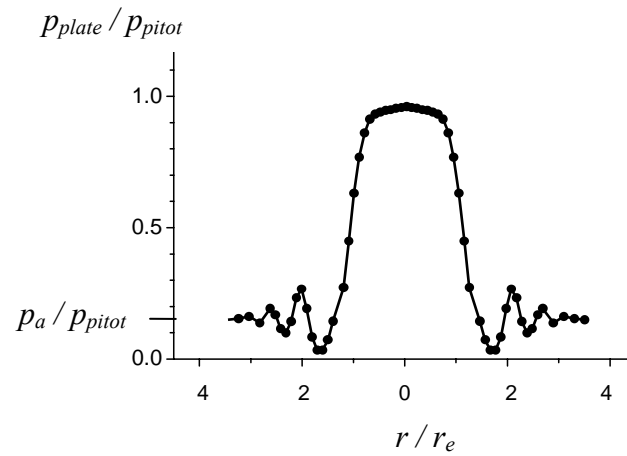

Fig. 3.23. Supersonic jet impingement: typical radial pressure distribution on a plate.
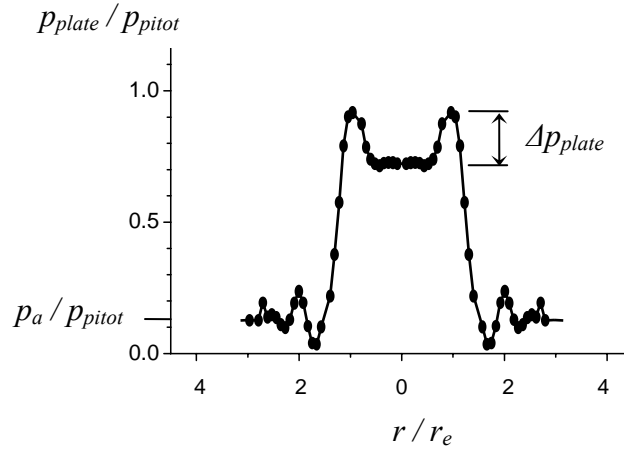The pressure is normalized by the Pitot-pressure in the free jet.

Fig. 3.24. Supersonic jet impingement: radial pressure distribution on a plate (normalized by the Pitot-pressure in the free jet) when a recirculating flow is present in the shock layer.

Under certain conditions the maximum of the plate-pressure distribution is located off the center. Hence, at the center the pressure is smaller than at the periphery, e. g., at $r/r_e \sim 1.0$ (Fig. 3.24). Locally, this results in a positive gradient of the plate pressure between the center and the location of the maximum pressure. It is known that this can indicate the presence of a bubble of slowly recirculating fluid in the shock layer [Kalghatgi & Hunt 1976]. The diameter of this bubble may be up to 0.8 times the jet diameter and its height can be sufficiently large to force the plate shock to change its shape and stand-off distance (Fig. 3.25).

3.2.2 Recirculation zone in the shock layer ahead of the plate

The most commonly used indicator of the appearance of a recirculation bubble is a plate-pressure distribution as shown in Fig. 3.24, having a relatively low pressure region at the center and an annular high pressure peak in the periphery. It has been suggested [Ginzburg et al. 1973, Gubanova et al. 1973, Kalghatgi & Hunt 1976] that positive pressure gradients on the wall below the shock layer occur as a result of the interaction between the plate shock and oblique shocks in the jet. When these shocks intersect each other a triple shock structure is formed (cf. chapter 3.1.3). A slip line extends from the triple point to the plate and divides the flow into two regions. In the peripheral region the stagnation pressure is greater than in the region between slip line and axis. Flow mixing occurs along the slip line. The mixing layer reaches the surface of the plate. Gas from the peripheral region that has a higher stagnation pressure decelerates and raises the pressure in the flow near the plate, initiating a recirculating flow.
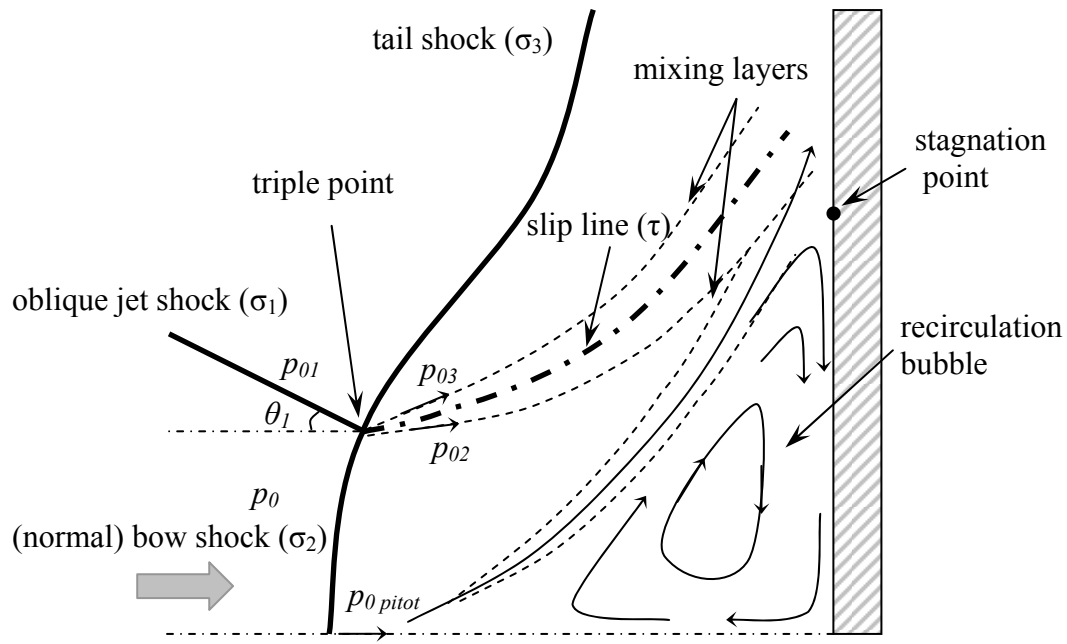
Fig. 3.25. Sketch of a flow field with a recirculation zone.

In the following the different stagnation pressures behind the interacting shocks will be calculated. In Fig. 3.25 the triple shock configuration is presented. The section of the plate shock which is downstream of the nozzle shock is known as the "tail" shock, while the remainder is termed the "bow" shock. It can be seen from the shock geometry that the stagnation pressure p_{03} and p_{02} on the tail-shock side and on the bow-shock side of the slip line originating at the triple point will both be greater than the stagnation pressure $p_{0\,pitot}$ at the jet axis where the streamlines pass through a normal shock. Values of the ratios $p_{02} / p_{0\,pitot}$ and $p_{03} / p_{0\,pitot}$ have been calculated from triple shock theory (cf. eq. 3.24) and are plotted in Fig. 3.26 against the inclination angle θ_1 of the incident shock. The flow Mach number was assumed to be $M = 2.78$, as in the experiments. It can be seen that p_{03} is substantially larger than p_{02} even in the case of a very weak incident shock σ_1. (Note: an angle of inclination of $\theta_1 = 21°$ corresponds to a weak Mach wave ($J_1 = 1$) in a flow with a Mach number of $M = 2.78$.) It can be seen that the difference between the stagnation pressures p_{02} and p_{03} calculated at the triple point is normally much greater than the pressure peak Δp_{plate} measured on the plate (Fig. 3.24). The essential feature is a shear layer which approaches a subsonic boundary layer and raises the stagnation pressure of the fluid just above the boundary layer. It is clear that the magnitude of the pressure peak on the plate depends on length, width and other characteristics of the shear layer.
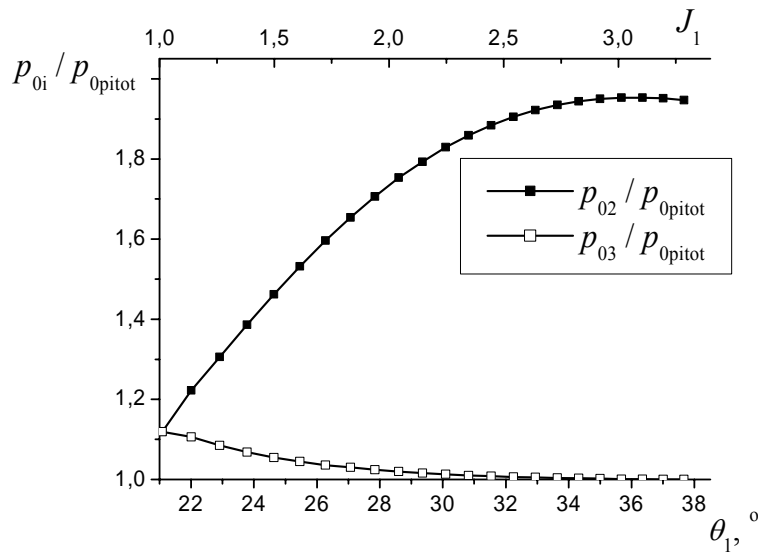
Fig. 3.26. Ratios of stagnation pressures for a triple shock structure as a function of the angle of inclination θ_1 of the incident shock. Mach number of the oncoming flow: $M = 2.78$. The angle of inclination θ_1 and the intensity J_1 of the incident shock are connected by eq. 3.14.

According to this mechanism, the main factors which determine whether a steady recirculation bubble can occur are outlined. Firstly, it is the area of the plane bow shock, since it determines how much fluid will pass inboard of the slip line and therefore how closely the slip line will approach the plate. The second factor influencing the pressure rise is the difference between the stagnation pressure in the peripheral flow and the stagnation pressure on the axis (p_{03} - $p_{0\,pitot}$). For a given pressure difference the amount of mixing along the slip line is clearly also of importance. The width of the mixing region is proportional to the length of a shear layer. Thirdly, it is the pressure rise needed to separate the boundary layer, which depends on the structure of the boundary layer. Based on these lines Kalghatgi & Hunt (1976) give a criterion for the presence of a recirculation bubble and a qualitative agreement with experiments is shown. Although a qualitative criterion for the occurrence of a recirculation bubble is obtained by Kalghatgi & Hunt, the mechanism of bubble formation is still not understood.

It has been noted that unsteady flow situations can occur when recirculation bubbles are present [Ginzburg et al. 1973, Henderson 1966]. These authors state that they have seen, by means of a schlieren system, the plate shock to be fluctuating between a peaked shape and a flat shape. This suggests that a bubble is being formed and swept away. No complete explanation of this phenomenon was given, since the unsteady dynamics of bubble formation and destruction are not understood.

Analogous phenomena occurring due to the interaction of shocks are also present in other flows. One example is given by unsteady supersonic flows over spiked bodies. In this case (Fig. 3.27) a separation zone is periodically generated on the spike, grows vigorously in size, and then vanishes. Several authors [Antonov et al. 1976, Antonov & Gretsov 1977, Zapryagaev & Mironov 1990] have investigated the physical pattern of flows with fluctuations of the separation zone. Although a rigorous theory does not exist, the main characteristics of the phenomenon as a function of the

geometrical parameters of the configuration and physical characteristics of the free stream have been found. The physical model of the formation and disappearance of the recirculation zone is similar to the one given for impinging jets.

Another example given here is the effect of wall-jetting in the case of Mach reflections. The non-stationary reflection of a plane shock wave propagating over a planar wedge (Fig. 3.28) has been investigated quite extensively and details on this type of reflection can be found in [Ben-Dor 1991]. It is shown that under certain conditions a strong wall-jet may be formed behind the incident shock and some part of the (initially) plane shock becomes locally convex in forward direction. Furthermore, Henderson et al. (2003) and Vasilev et al. (2004) also showed that the strong jetting flow is unstable and the behavior of shock-jet configurations usually has a locally oscillatory character.
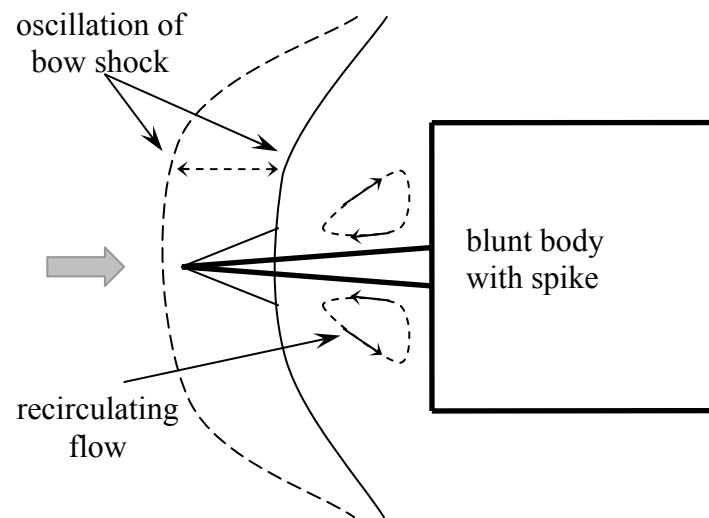
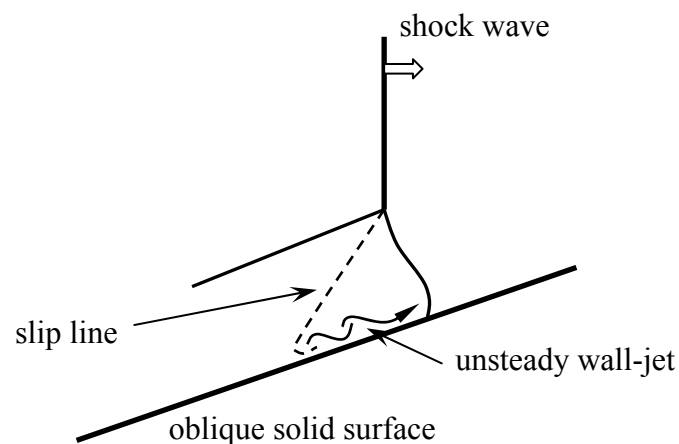Fig. 3.27. Unsteady supersonic flow over a spiked body: formation of a recirculation bubble.

Fig. 3.28. Wall-jetting in Mach reflection.

3.2.3 Characteristics of normal jet impingement on a flat plate

In Fig. 3.29 typical shadowgraphs are shown of shocks formed ahead of a plate when a supersonic jet impinges onto the plate. At the nozzle exit the flow Mach number equals $M_e = 2.78$ and the time of exposure is given by $t_{exp} = 10$ μs. In the shadowgraphs shown the nozzle-to-plate distance x and the off-design degree n were changed. As can be seen the geometry of the plate shock, its stand-off distance and behavior depend strongly on the parameters x and n. For example, at the same distance of $x = 2.3r_e$ the plate shock is flat for an off-design degree of $n = 0.99$ and convex for $n = 0.76$. Similarly, also a change of the distance between the nozzle and plate leads to a variation of the shock characteristics. When the nozzle-to-plate distance x is increased ($n = 0.76$), e.g. from $2.3r_e$ to $7.1r_e$, the shock geometry changes periodically from flat to convex and inversely. At certain distances, e.g. at $x = 6.3r_e$, the plate shock becomes strongly unsteady. In this case the stand-off distance varies strongly within a time which is shorter than the time of exposure of the shadowgraph (10 μs). This results in the somewhat blurred shadowgraph corresponding with this case.

Not only the shape of the plate shock changes but also its distance from the plate. In Fig. 3.30 the stand-off distance h of the plate shock is plotted as a function of the nozzle-to-plate distance x for a jet having a degree of off-design of $n = 0.76$. Note that in the case of convex plate shocks the maximum distance which occurs always on the jet axis was taken. The stand-off distance of the shock is constant for a wide range of nozzle-to-plate distances. However, the stand-off distance h increases periodically. In the range of x considered here an increase of h occurs twice, at $x \sim 2r_e$ and $x \sim 6r_e$. These values of the nozzle-to-plate distance agree well with those locations in a free jet (i. e., in a jet that does not impinges on an obstacle) where the nozzle and jet shocks, respectively, are reflected at the axis (cf. Fig. 3.16). In the shadowgraphs it can be seen that if a convex plate shock is formed it appears always slightly upstream of that location where the nozzle shocks are reflected in the free jet. In this case conditions are well appropriate for the formation of a recirculating flow in the shock layer. The displacement effect of the recirculation bubble results in the convex shape of the plate shock.
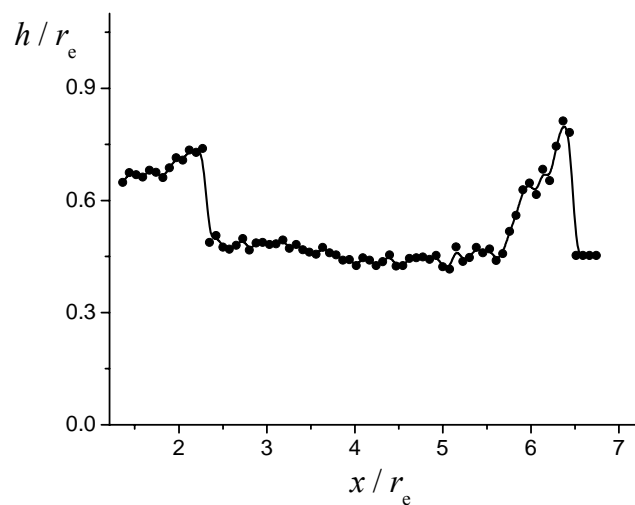
Fig. 3.30. Stand-off distance h of the plate-shock as a function of the nozzle-to-plate distance x ($n = 0.76$).

$n = 0.99, x = 2.3r_e$

$n = 0.76, x = 2.3r_e$

$n = 0.76, x = 2.8r_e$

$n = 0.76, x = 5.5r_e$

$n = 0.76, x = 6.3r_e$
(unsteady)

$n = 0.76, x = 7.1r_e$
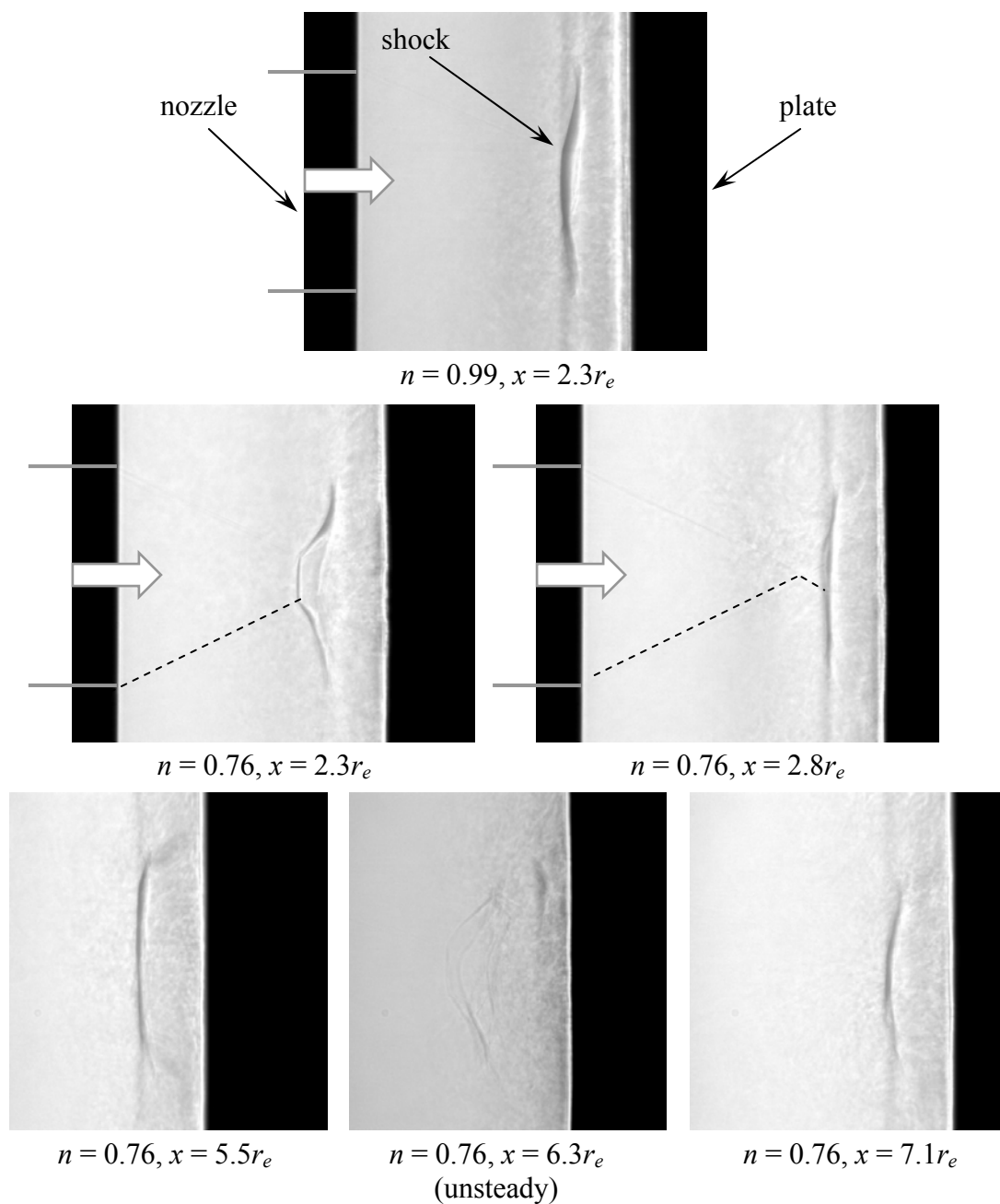
Fig. 3.29. Shadowgraphs of the shock ahead of a plate at different nozzle-to-plate distances x (exposure time: 10 µs). In the lower part of some pictures the position of the nozzle shocks have been indicated by dashed lines.
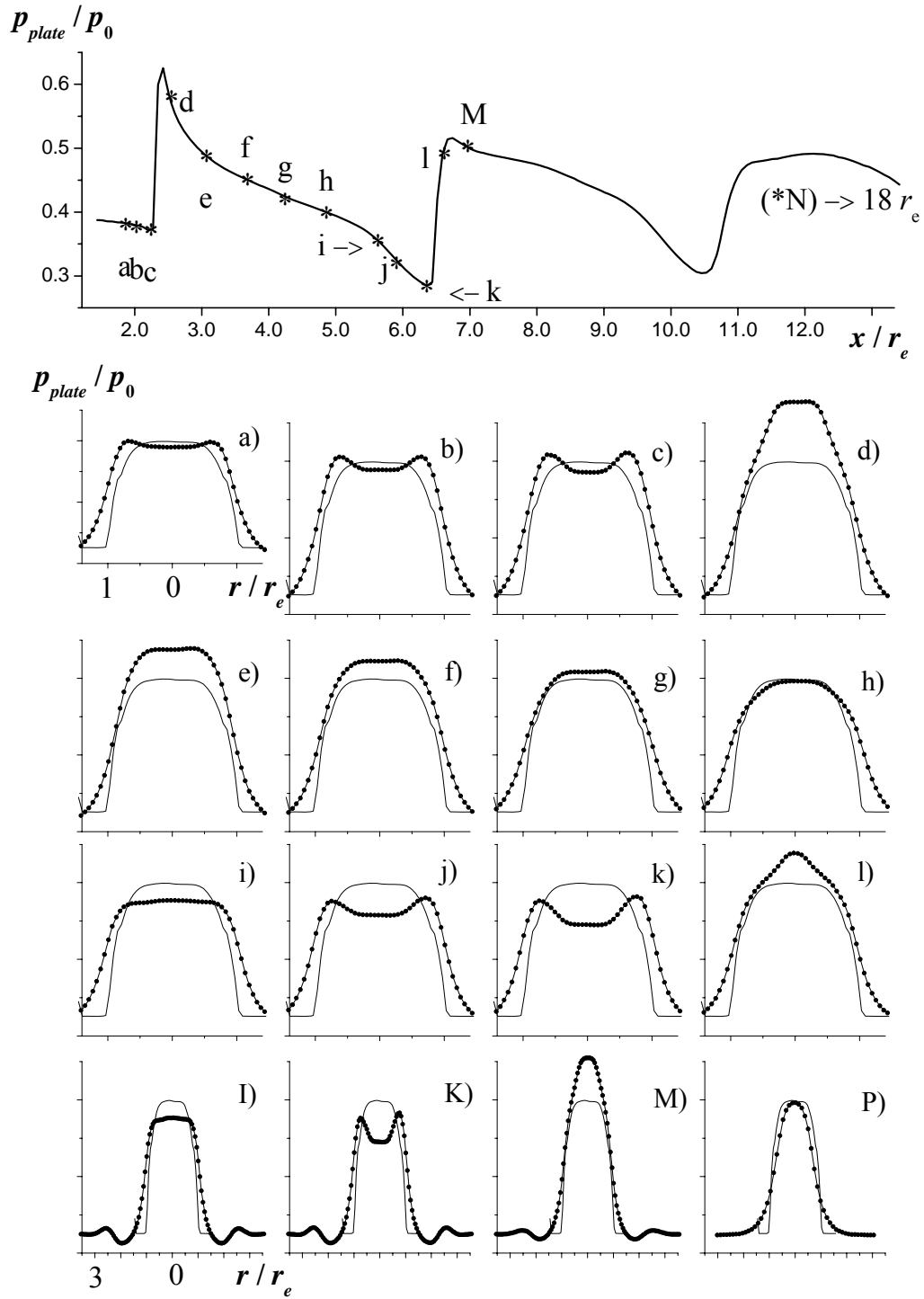
Fig. 3.31. Axial (top figure) and radial (figures a - p) profiles of the pressure measured on the plate surface in the impingement region of a jet with $M_e = 2.78$ and $n = 0.76$. In each figure with radial profiles the radial distribution of the Pitot-pressure measured in the free jet at the nozzle exit is shown for comparison. The axial locations of the radial profiles are indicated in the top figure

54
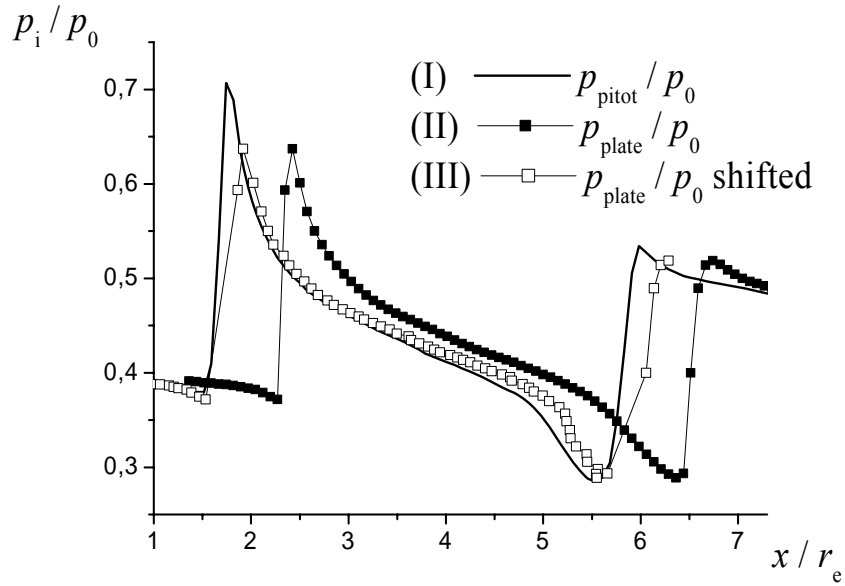
Fig. 3.32. Comparison of axial profiles of the Pitot-pressure and the pressure on the plate surface.

Measurements of the pressure performed on the surface of the plate confirm the explanation given above of the change of the shape of the plate shock being caused by the displacement effect of the recirculation bubble. In Fig. 3.31 axial and radial profiles of the pressure on the plate are shown. The data were obtained under the same conditions as above, i.e., at the nozzle exit the Mach number equals $M_e = 2.78$ and the degree of off-design is given by $n = 0.76$. Let us consider radial pressure profiles which were obtained for those nozzle-to-plate distances that correspond with changes in the shape of the plate shock, i.e., $x \sim 2r_e$, $x \sim 6r_e$ (Fig. 3.31a, b, c and Fig. 3.31j, k). In all these cases the pressure profiles are similar to the profile shown in Fig. 3.24, i.e., the maximum is located off the axis at a radial position $r > 0$. As has been discussed above (cf. section 3.2.2) such plate-pressure distributions having a positive radial gradient, are characteristic of the formation of a recirculation zone in the shock layer ahead of the plate.

The axial distribution of the pressure on the plate surface is similar to the axial profiles of the Pitot-pressure measured in the free jet (compare Fig. 3.31 and Fig.3.20). Both, ahead of the plate and ahead of the Pitot-tube a normal shock is formed and the pressure is determined at a stagnation point. Agreement between the pressures obtained is particularly good if we take into account the stand-off distance of the shock from the plate. In Fig. 3.32 three axial profiles of the pressure are shown: (I) the Pitot-pressure measured in the free jet, x corresponds to the position of the open end of the Pitot-tube; (II) the plate pressure as a function of the nozzle-to-plate distance x and (III) of the plate pressure as a function of the distance $x_{new} = x_{(plate)} - h$ between the nozzle exit and the plate shock. The stand-off distance of the bow shock from the Pitot-tube is negligibly small (about 0.2 mm or $0.06r_e$). Hence, in the case of the Pitot-pressure and the shifted plate-pressure profiles the parameter x represents the distance between the nozzle exit and the plane shock ahead of the Pitot-tube and the plate, respectively. The agreement between the Pitot-pressure and the shifted plate-pressure profile is obvious. Hence, the position of the plate shock with respect to the nozzle exit determines the pressure on the plate. In view of this let us consider the influence of an increase of the stand-off

distance of the plate shock on the plate-pressure (at a constant nozzle-to-plate distance x). At nozzle-to-plate distances, where the shock stand-off distance assumes a maximum value (e.g. at $x \approx 6.3r_e$), an increase of the shock-to-plate distance corresponds to a decrease of the plate-pressure. Note that in experiments a strong oscillation of the plate shock is observed exactly for such distances. Thus a motion of the shock away from the plate leads to a change of the plate-pressure from higher values to lower ones. Note that in the axial pressure profiles regions of high and low values of the plate-pressure correspond to radial profiles without and with a maximum off the axis (e.g., Fig. 3.31l and k). In this manner the change of the position of the plate-shock corresponds with a transition between the two typical radial distributions of the plate-pressure, or, respectively, between two flow fields: with and without recirculation bubble.

It is necessary to note that the same conformity of the shock behavior and pressure distributions has also been found for other degrees of off-design of the jet (n = 0.61, 0.76, 0.87, 0.99, 1.1).

3.2.4 Correlation between shock motion and plate-pressure variation

As shown above the plate shock is essentially unsteady at those nozzle-to-plate distances that correspond to the formation of a recirculation bubble. High-speed films of the flowfield in the impingement zone ahead of the plate and high-frequency pressure measurements show strong oscillations both, of the shock as well as of the plate-pressure when a recirculation zone is present. In order to study the connection between shock and pressure oscillations synchronized pressure measurements and visualizations of the plate shock have been performed. The results of these measurements have then been related to each other by means of a correlation function.

In performing the synchronized measurements many series of 5-exposure shadowgraph pictures have been obtained together with pressure oscillograms that were taken during the time of the five exposures. From the shadowgraphs the stand-off distances h_{ij} of the plate shock were determined. Here, the index i denotes the shadowgraph and j, $j = 1, .., 5$, the different shock locations corresponding with the 5 exposures on shadowgraph number i. The correlation function $r_{corr}(t)$ relating to a particular nozzle-to-plate distance is defined as follows:

$$r_{corr}(t) = \frac{1}{\sigma_p \cdot \sigma_h} \sum_{i,j} \left(p_i(t - \tau_{i,j}) - \overline{p} \right) \left(h_{i,j} - \overline{h} \right), \qquad (3.27)$$

where t is the time, $\tau_{i,j}$ is the time of each exposition number j of the shock on shadowgraph number i and $p_i(t)$ is the pressure oscillogram. Statistical means $\overline{p}, \overline{h}$ and standard deviations σ_p, σ_h are calculated from the same sample of shadowgraph-oscillogram pairs. Typically, fifty pairs are evaluated per sample.

In Figures 3.33-34 pressure oscillograms and correlation functions are plotted for several nozzle-to-plate distances x. In all cases the pressure oscillates sinusoidally about some mean value. However, in the case of the greater nozzle-to-plate distance, $x = 6.52r_e$ (Fig. 3.33e), also pressure bursts occurring non-regularly are present. Nonetheless, in all cases the correlation function has a physically significant extremum at the same time: $t_{corr} \approx 7$ μs (cf. Fig. 3.34). The other extremums of the correlation function only reflect the periodical behavior of the pressure. At the time $t = t_{corr} \approx 7$ μs values of the correlation functions are always close to minus one ($r_{corr}(t) \approx$ -1.0).

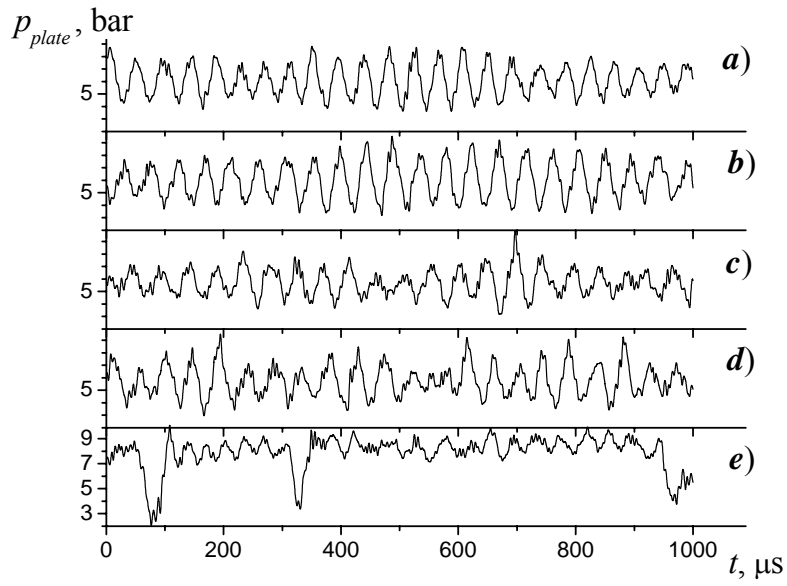Fig. 3.33. Plate-pressure oscillograms at different nozzle-to-plate distances: *a*) $x = 6.06r_e$, *b*) $x = 6.21r_e$, *c*) $x = 6.29r_e$, *d*) $x = 6.36r_e$, *e*) $x = 6.52r_e$.
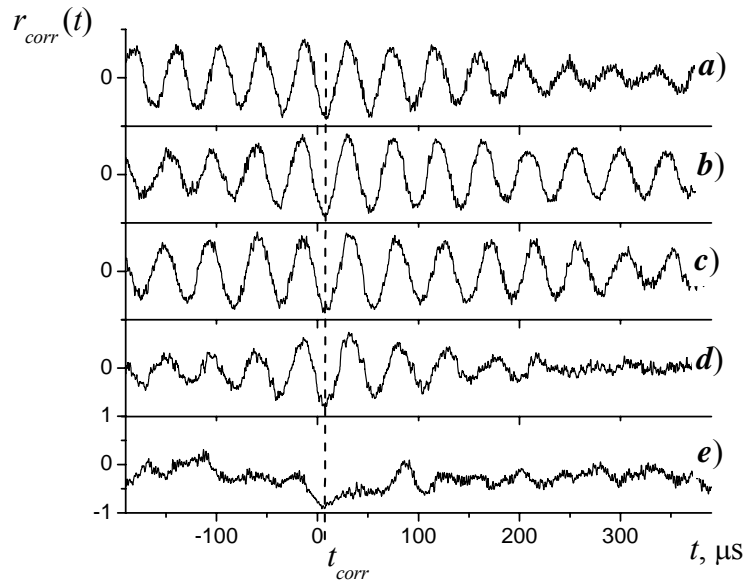

Fig. 3.34. Correlation function $r_{corr}(t)$ for experimental data obtained at different nozzle-to-plate distances: *a*) $x = 6.06r_e$, *b*) $x = 6.21r_e$, *c*) $x = 6.29r_e$, *d*) $x = 6.36r_e$, *e*) $x = 6.52r_e$.
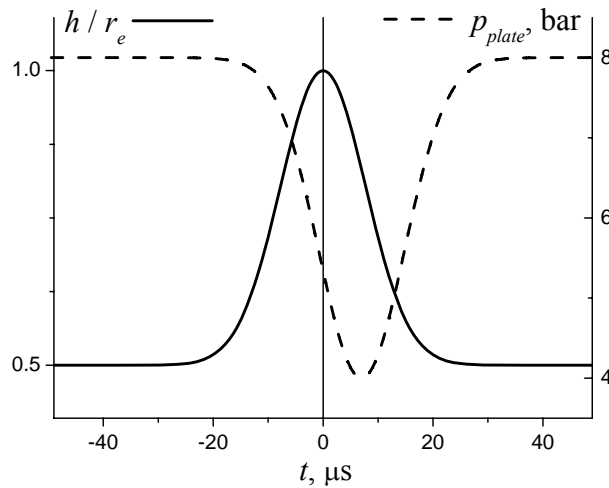
Fig. 3.35. Sketch of the response of the plate-pressure on the motion of the plate-shock.

This shows that there exists a strong correlation between the oscillation of the shock and the variation of the pressure. Furthermore, the pressure change is in anti-phase to the shock oscillation and has a time lag of about $t_{corr} \approx 7$ μs. This behavior model is sketched in Fig. 3.35.

The negative correlation (i.e. anti-phase oscillation) confirms that the behavior of the mean value of the plate-pressure depends on the nozzle-to-shock distance as was discussed above (cf. Fig. 3.32). In this manner the non-periodic pulsation of the pressure in the case of a nozzle-to-plate distance of $x = 6.52 r_e$ (Fig. 3.33e) can be explained by the motion of the plate shock from a position after the location x_b of the reflection of the oblique shocks to a position in front of the reflection of the oblique shock at the axis. This corresponds to unfavorable and favorable conditions for the occurrence of a recirculation bubble. Thus conditions are so that a recirculation bubble can be formed and destructed in rapid succession.

The experiments clearly show that the motion of the plate shock determines the variation of the flow field in the impingement region. Since the formation of a recirculating flow ahead of the plate is caused by shock interactions the flow field is very sensitive to the position of the plate shock in the impinging jet. As long as the formation of recirculation bubble reorganizes the flow field strongly this, in one's turn, should affect the plate shock. The response of the plate-pressure to the motion of the plate shock is delayed by several microseconds (t_{corr}). This has an influence on the time characteristics of resonance system formed.In order to study the time characteristics of the flow oscillations more closely a spectral analysis of the pressure oscillograms was performed. This is the subject of the next section.

3.3 Flow oscillations at normal impingement of a jet

Supersonic impinging jets generate acoustic waves. The spectrum of the waves and self-excitation characteristics of the jet-obstacle interaction are determined by feedback mechanisms and resonances caused by the shock structures in the jet. However, the connection between the production of sound and the structure of the oscillating flow is still not well understood. The complicated structure of the flow in the impingement and the wall-jet regions as well as changes in the jet structure that depend on the degree of over-/underexpansion, nozzle-to-plate distance and plate size, are the reason why it is difficult to connect features of flow oscillations with unsteady behaviors of the shock structures. Furthermore, presently it is still very complicated to predict theoretically/numerically unsteady flow regime of the impingement.

Here, different regimes of supersonic jet impingement and corresponding oscillation characteristics were studied experimentally. In particular, the interaction between unsteady flow fields with a recirculation zone and self-sustained oscillations in the impinging jet are considered in the following.

3.3.1 Importance of acoustic waves

It is known that supersonic jets are inherently unstable. Unsteadiness can be caused in a variety of ways, for example, by turbulent mixing at the jet boundary, by turbulence convected out of the jet nozzle or it can also be generated by intrinsic hydrodynamic instabilities of the flow field. In the flow field of a supersonic jet the most highly sheared region is the mixing layer at the circumference of the jet immediately downstream of the nozzle exit. Hence this is a location that is most favorable for the origin of flow instabilities. Here, two types of instabilities can be distinguished. The first one, corresponding with short wavelengths, is scaled according to the mixing-layer thickness. The second one includes large-scale instabilities (long wavelengths) with a scale length equal to the diameter of the jet [Tam1972, Tam & Burton 1984]. The latter type of instabilities control the dynamics and mixing of the jet fluid and are the dominant source of jet mixing noise. For non-ideally expanded jets the presence of shock cell structures inside the jet flow leads to the radiation of additional noise. The additional noise consists of two components. One has a discrete frequency and the other is broadband [Tam & Hu 1989].

Acoustic waves are also generated when supersonic jets impinge on an obstacle. Based on spectral analysis pressure oscillations can again be divided into broadband noise and resonance-like discrete tones, so-called *impinging tones*. It is known [Umeda & Ishii 1993, Varnier & Raguenet 2002] that for an impinging jet the level of broadband noise is increased compared to that of free jets. In addition to the commonly known sources of sound of supersonic jets, such as mixing noise and shock associated noise, the increased levels may also be attributed to acoustic reflections from the plate and to the generation of additional noise by sources in the jet impingement and wall-jet regions of the flow field.

The resonance-like behavior of sound-producing oscillations is generally explained using a feedback loop [Tam & Ahuja 1990, Henderson 2002]. According to this explanation the energy for the feedback loop is provided by instability waves in the shear layer of the jet. These waves are generated by acoustic excitation in the region near the nozzle exit. The waves grow as they propagate downstream and manifest

themselves as large-scale vortical structures. Upon impingement on the plate, these large structures generate coherent pressure fluctuations which result in acoustic waves of great intensity. The acoustic waves travel back through the ambient medium and, upon reaching the nozzle exit, excite the shear layer of the jet. In such a way the feedback loop is closed.

It is clear that flow oscillations which generate acoustic waves also result in pressure oscillations in the shock layer ahead of the plate. In the present work the oscillations of pressure on the surface of the plate have been studied. In this the conditions of the jet impingement, i.e., the degree of off-design of the jet and the nozzle-to-plate distance, have been varied.

3.3.2 Oscillation characteristics of normal jet impingement on a flat plate

At the center of the impingement region oscillograms of the plate-pressure have been obtained for different nozzle-to-plate distances. For the spectral analysis a Discrete Fast Fourier Transformation has been applied. A typical spectrum is shown in Fig. 3.37. In such spectrograms it is often possible to distinguish several peaks. The peaks can be arranged in order of theirs magnitude as one *main* and several *secondary* peaks.

For analysis it is useful to consider a two-dimensional representation of several spectrograms in which amplitudes of spectral lines are represented by a gray level. This representation, called a multi-configuration spectrogram hereafter, is similar to that used in acoustics where frequencies are plotted versus time, for example, in speech analysis. Here, instead of time the abscissa represents different nozzle-to-plate distances, i.e., different configurations. A typical multi-configuration spectrogram is shown in Fig. 3.38. The multi-configuration spectrogram consists of 93 spectrums obtained every half millimeter of the nozzle-to-plate distance in the range of $x = 4.5$ - 50.5 mm, or, respectively, $x = 1.4r_e$ - $15.3r_e$.

Let us consider main features of such multi-configuration spectrograms. The maximum gray level, and, respectively, maximum intensity of the spectral lines, are combined into short inclined lines marked as *main peaks*. These main peaks usually lie in a small range of frequencies, with the mean frequency shown as f_{max}. Side maximums of spectrums (*secondary peaks*) form curves which always run from top to bottom when x is increased. Hence the frequency of secondary peaks decreases monotonically with increasing nozzle-to-plate distance. At certain distances x a darkening is present in the range of low frequencies (marked as low-frequency burst in Fig. 3.38). In these cases the spectrogram has usually no pronounced peaks. This may be interpreted as the presence of non-periodical pressure pulses. Finally, it is necessary to mention that there are also some small peaks which are generated by electronics and have no relation to phenomena in the gas flow. Since characteristic frequencies of the apparatus do not depend on the flow these peaks are represented by weak horizontal lines. Vertical white lines have been added in order to show the position of every tenth measurement, i.e. these lines correspond to nozzle-to-plate distances that are 5 mm apart, and, thus, the white lines are not related to pressure oscillations.

In Fig. 3.39-3.41 multi-configuration spectrograms of plate-pressure oscillations are shown for impinging jets having three different degrees of off-design: overexpanded ($n = 0.76$), close to ideally expanded ($n = 0.99$) and underexpanded ($n = 1.1$) jets. In addition to the multi-configuration spectrogram the figures contain several extra diagrams. Before beginning the discussion let us describe the meaning of these diagrams in detail.
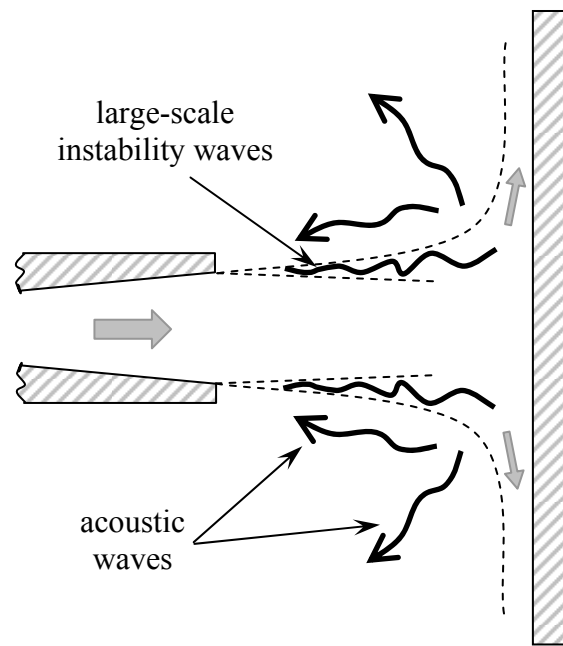
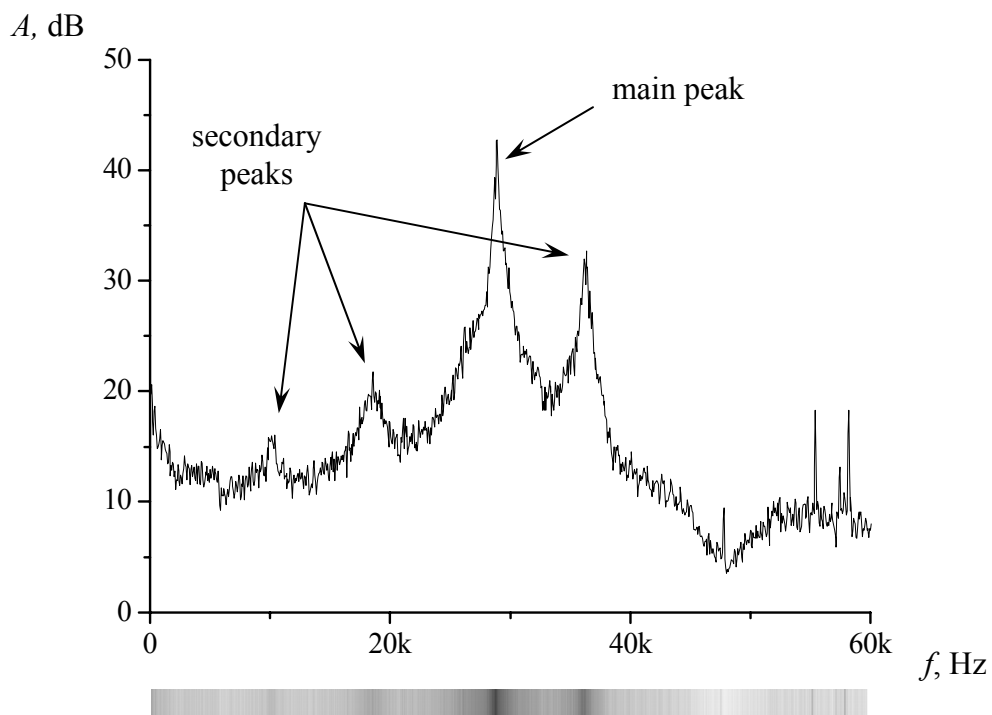Fig. 3.36. Schematics of the feedback loop of an impinging jet.

Fig. 3.37. A typical spectrum and its representation by a strip showing the intensity by gray-levels.
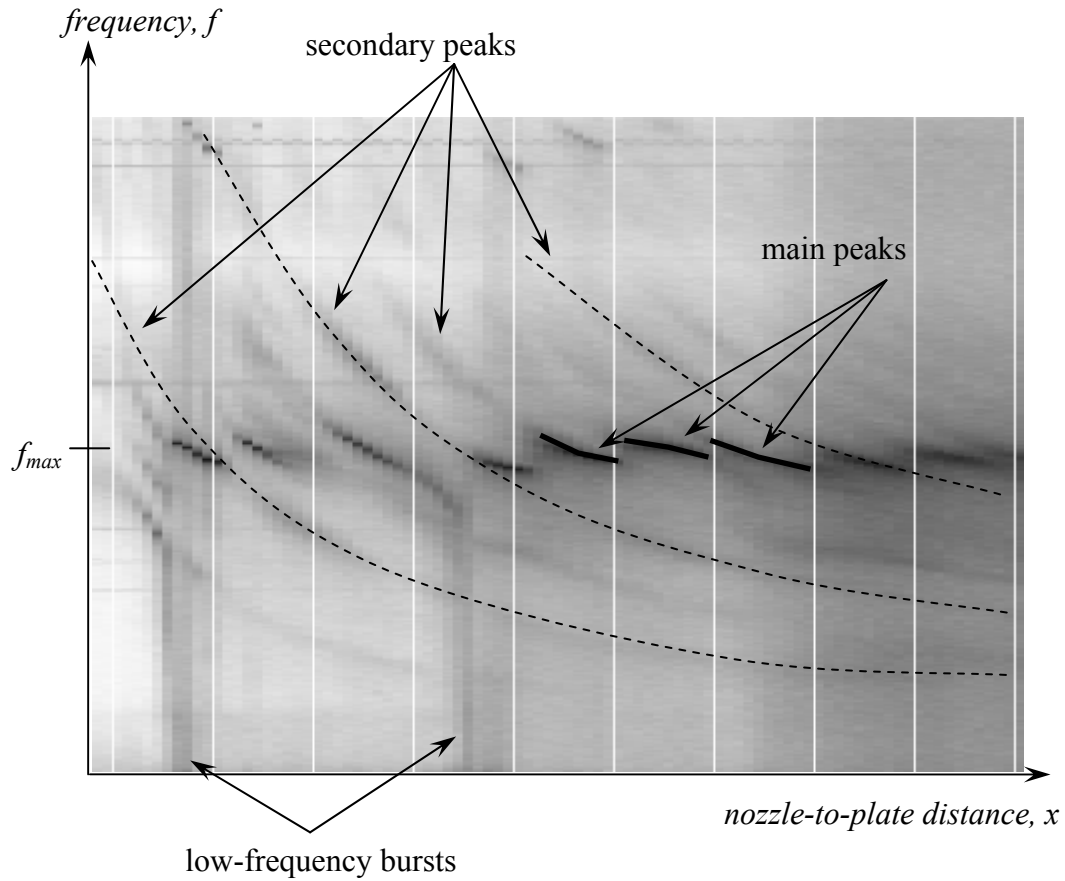
Fig. 3.38. Sketch of a pressure multi-configuration spectrogram. Three of the main and secondary peaks have been enhanced by solid and dashed lines, respectively.

The spectrogram and all curves are shown as a function of the nozzle-to-plate distance x. The scale of the abscissa which is the same in all diagrams is represented in two units: in millimeters and in terms of the radius of the nozzle exit, r_e. Each figure includes four diagrams: the multi-configuration spectrogram of plate-pressure oscillations (top figure); the mean value of the pressure and its standard deviation, which characterizes the mean amplitude of the pressure oscillation (curve 1); the spectral amplitude of the main peaks (curve 3) and the amplitude of the 12-kHz spectral line which is taken as a representative of the magnitude of low-frequency (and also "white") noise (curve 2); and, finally, the value of the stand-off distance h of the plate-shock (curve 4). Intensities of the spectral lines of the multi-configuration spectrogram are represented by a gray level (a scale in dB is shown on the right side of the image). Mean values of the pressure (curve 1) are normalized by the reservoir pressure. Spectral amplitudes of the main peaks (curve 3) are shown in dB, relatively to the background noise (curve 2). The stand-off distance of the plate-shock is normalized by the radius of the nozzle exit r_e. Accurate measurements of stand-off distances were performed only for $x < 7r_e$ because the field of view of the diagnostic system was limited.

Fig. 3.39 Characteristics of plate-pressure oscillations as a function of nozzle-to-plate distance x for a jet having a degree of off-design of $n = 0.76$. Note that spectral amplitudes of main peaks (3) are shown in dB, related to the background noise (2) (for details see text).

Fig. 3.40. Characteristics of plate-pressure oscillations as function of nozzle-to-plate distance x for a jet having a degree of off-design of $n = 0.99$. Note that spectral amplitudes of main peaks (3) are shown in dB, related to the background noise (2) (for details see text).
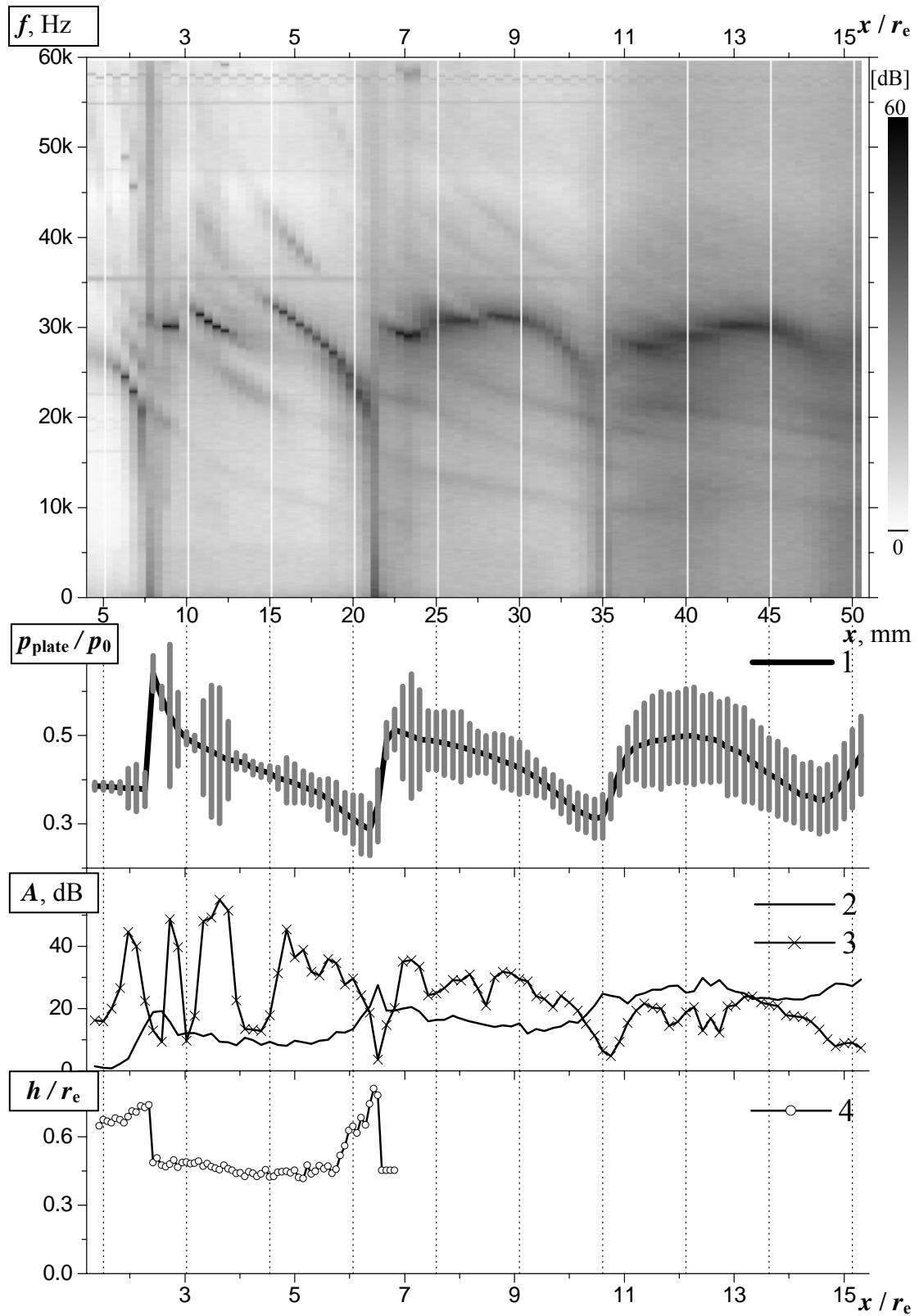
Fig. 3.41. Characteristics of plate-pressure oscillations as function of nozzle-to-plate distance x for a jet having a degree of off-design of $n = 1.1$. Note that spectral amplitudes of main peaks (3) are shown in dB, related to the background noise (2) (for details see text).
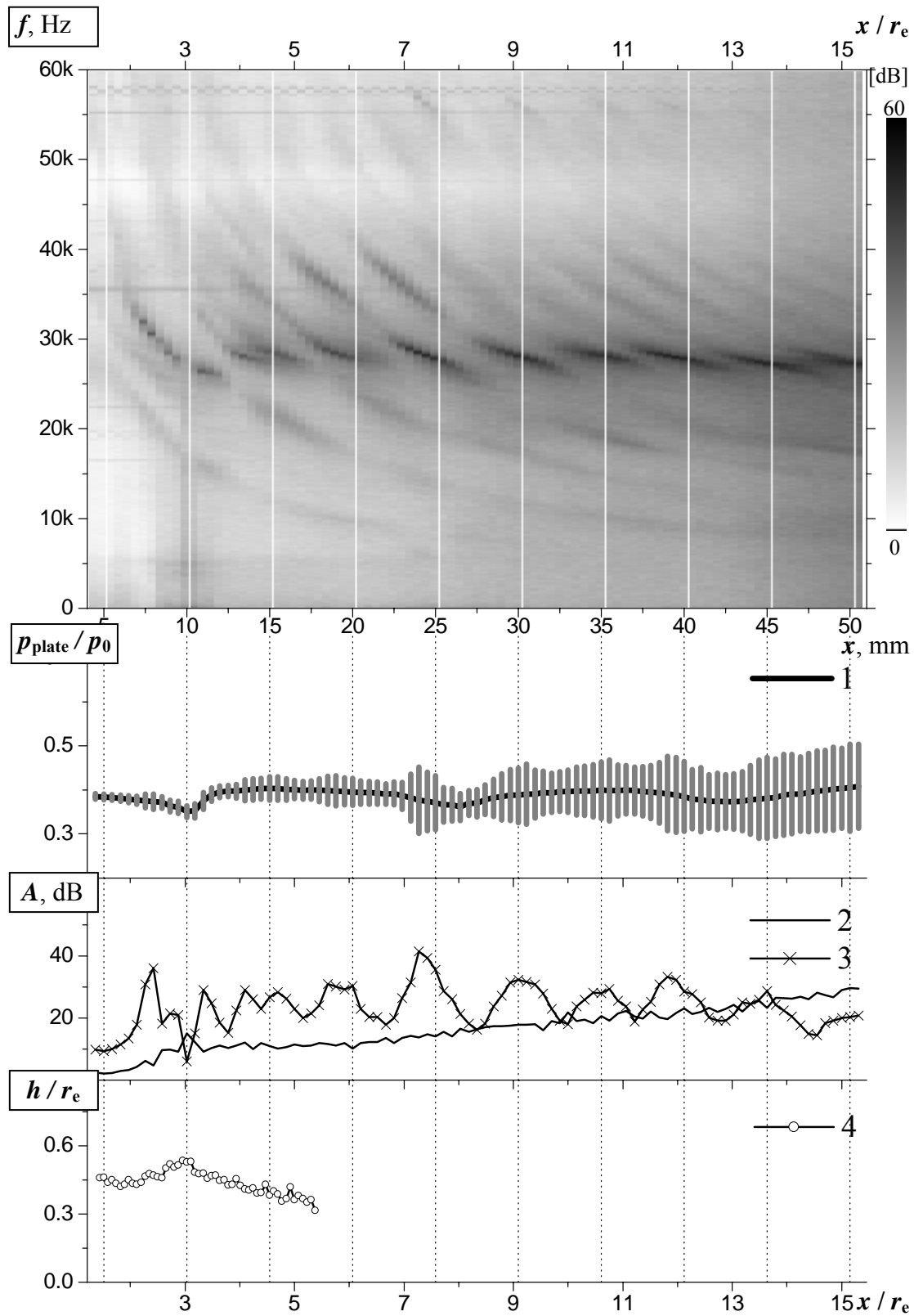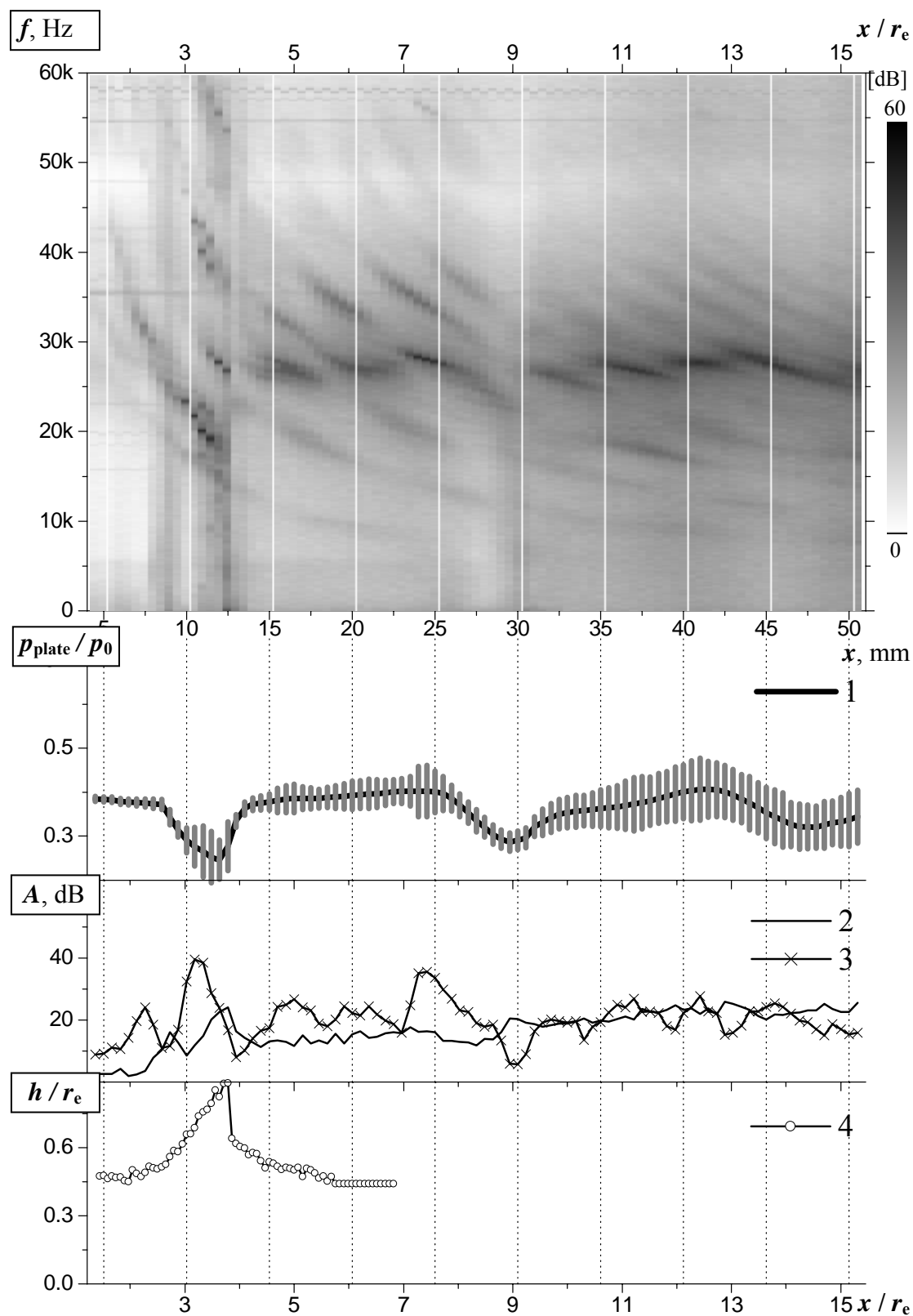
Up to now discrete tones generated by impinging jets have been considered to be caused by one source only. However, at least two different components of pressure oscillations are recognized by the method of data representation used in the present work. In figures 3.39-3.41 these components are represented by main and secondary peaks. A comparison of the multi-configuration spectrogram images using the *Image Marker* program (see Appendix) shows that secondary peak curves have the same position in each spectrogram within the limit of accuracy. It means that flow oscillations represented by these peaks are independent of the degree of off-design of the jet. It seems also that these flow oscillations are independent of the shock structures in the jet. Secondary peaks change their position in the spectrum smoothly with the nozzle-to-plate distance. In contrast to the behavior of the secondary peaks, the frequency of the main peak depends on parameters of the jet. The shock structures in the jet (which change with the degree of off-design) have a strong influence on the position of the main peaks. Furthermore, some changes in the spectrum are associated with changes of the thickness of the shock layer ahead of the plate. In the following these aspects of flow oscillations relating to both secondary and main peaks, are discussed in detail.

Firstly, let us consider oscillations presented by secondary peaks. The character of the secondary peak curves (multiplicity and dependence on inverse nozzle-to-plate distance, $1/x$) allows to assume that a resonant excitation of instabilities corresponds to these curves. It has been shown in the last paragraph that the curves are practically independent of parameters of the jet, such as the degree of off-design. Hence, also an instability corresponding with these oscillations is independent of the jet parameters and we can associate the oscillations of discrete frequencies with the acoustic field excited due to the feedback mechanism discussed earlier in section 3.3.1 (see Fig. 3.36). The impingement tone frequency f_j may be determined from the following formula [Krothapalli et al. 1999]:

$$\frac{j + \varphi}{f_j} = \int_0^x \frac{\mathrm{d}x}{c_c(x)} + \frac{x}{c_a} .$$ (3.28)

Here, x is the distance between the plate and the nozzle exit, and $c_c(x)$ and c_a are the convection velocity of downstream-traveling large structures and the speed of acoustic waves traveling upstream in the ambient gas, respectively. j is an arbitrary integer and φ represents a phase lag. Note that the phase of the acoustic wave and of the convected disturbance may not be exactly the same at both the nozzle exit and the source of the instabilities.

In order to predict impingement tone frequencies using the above formula, accurate values of the velocity of large-scale structures traveling downstream are needed. Krothapalli et al. (1999) give results of measurements by a PIV technique. The measured convection velocity of vortical structures in the shear layer of a free supersonic jet was found to be about $0.6u_0$, where u_0 is the fully expanded jet velocity. For impinging jets the propagation speed of the large structures exhibits significant variations with the nozzle-to-plate distance. For example, the authors note an increase of the convection velocity from $0.5u_0$ to $0.6u_0$ when the nozzle-to-plate distance is changed from $x = 10r_e$ to $x = 25r_e$. Underexpanded supersonic jets with parameters in the range $n = 2.5$-5.0 and M = 1.5 were considered.
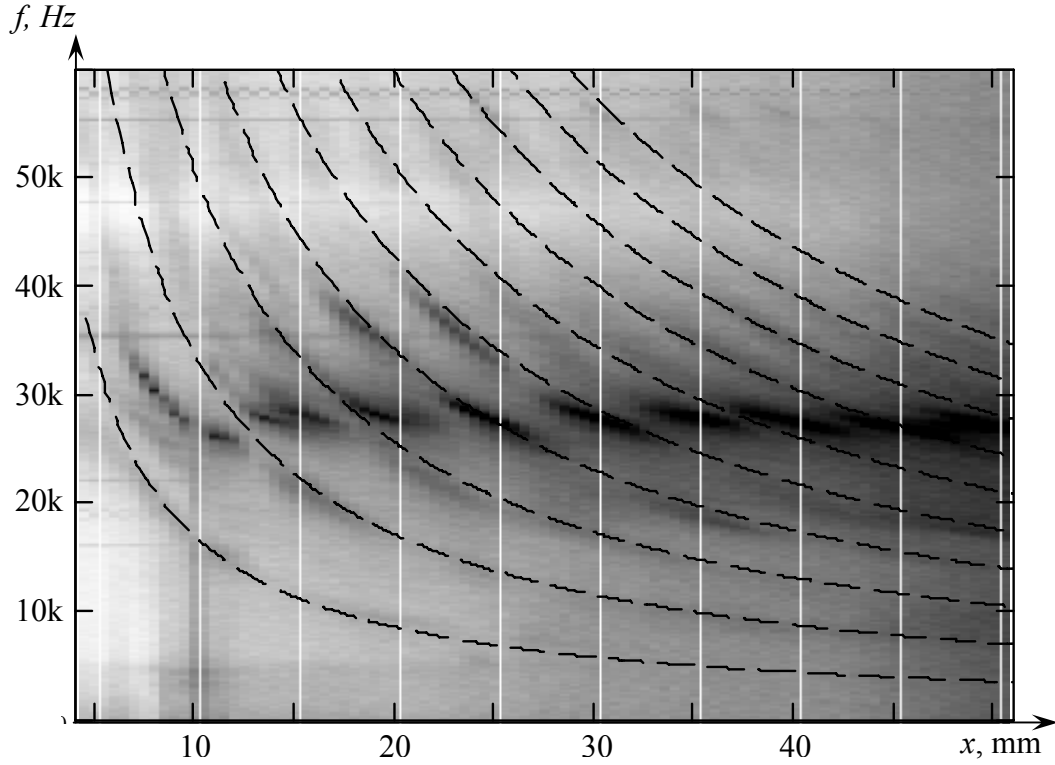
Fig. 3.42. Estimates of discrete secondary tones of the impinging jet added to a multi-configuration spectrogram (n = 0.99 has been chosen as example).

Based on this, resonance frequencies are fitted to the curves in Figs. 3.39-3.41. The following values of parameters are used: $j = 1,..,10$, $\varphi = 0$, $c_a = a_a$ (a_a: sound speed in the ambient gas) and the convection velocity is approximated by the formula:

$$c_c(x) = a_a + 0.01 \frac{x}{r_e} \cdot u_0 \equiv \left(0.55 + 0.01 \frac{x}{r_e} \right) \cdot u_0. \tag{3.29}$$

Note that under the conditions of the experiments the sound speed a_a in the ambient air equals $0.55u_0$. Results for the frequencies f_j are presented in Fig. 3.42. As can be seen the calculated values of impingement tone frequencies (dashed lines) describe the general behavior of the secondary peak curves in the multi-configuration spectrogram well. Some differences between experimental results and predicted values (for great nozzle-to-plate distances (in the far zone)) can be corrected by using of a better approximation for $c_c(x)$ than eq. 3.29.

Thus secondary peaks in the pressure spectrograms are the result of the large scale instability waves being excited due to a feedback loop through the ambient still gas. It is not yet clear the mechanism by which the instabilities reach the surface of the plate at the impingement center, where the pressure transducer was installed. The disturbances may propagate through the subsonic shock layer in a radial direction from the peripheral zone, but they may also influence the shock ahead of the plate which is unstable for transversal disturbances [Panda 1998]. It is also possible that disturbances penetrate into the jet core upstream of the plate shock, e.g., near the nozzle exit or even within the nozzle, by propagating upstream through the boundary layer of the nozzle flow. Corresponding velocity fluctuations in the jet core have been confirmed by PIV measurements [Elavarasan et al. 2000, 2001].

In most publications concerning acoustic waves produced by impinging jets the spectrums of oscillations have been described by a law similar to eq. 3.28. It is clear that the main peak frequencies in the spectrograms which depend strongly on shocks in the flow cannot be approximated by eq. 3.28 in which shocks are not taken into account. The behavior of main peaks can be explained symbolically by adding another element into the chain of elements of the feedback loop. This extra element can be considered as some kind of a complex filtering or resonance system whose characteristics depend on parameters of the impinging jet.

The main characteristics of such frequency filters are a master frequency (or resonance frequency) and a pass bandwidth. These characteristics determine a range of frequencies which can be transmitted by the filter or resonator. It is typical that the coefficient of transmission decreases smoothly from a maximum value for the master frequency to smaller values for side frequencies.

In the case of impinging jets the shock layer ahead of the plate could play the role of such a filtering (resonance) system in the feedback mechanism of oscillations. In a rough approximation the shock layer can be considered as a gas volume with permeable boundaries. In such systems gas oscillations have well-defined resonance frequencies [Meyer & Guicking 1974, Landau & Lifshitz 1987]. The resonance frequencies f_{res} depend inversely on a characteristic length L_{res} of the oscillating gas volume:

$$f_{res} \propto \frac{1}{L_{res}}. \tag{3.30}$$

Let us now consider those features of flow oscillations that are represented by the main peak in the spectrum, and discuss the relation of these features to a shock layer that has properties of a filtering and resonance system.

Firstly, it is the presence of a mean frequency, defined above as f_{max}, corresponding with the main peaks in the spectrograms. The system selects a narrow frequency range around f_{max}. The amplitude of oscillations is at a maximum for oscillations with this mean frequency f_{max} and decreases with a deviation from f_{max}. This is clear from the diagrams of the spectral amplitude of the main peaks (curve 3) in Fig. 3.39-3.41.

The correspondence between the range of frequencies transmitted by the filtering system and the thickness of the shock layer is remarkable. For example, in Fig. 3.39 the stand-off distance h of the plate shock (curve 4) increases in the neighborhood $x \sim 6r_e$ and the frequency of the main peak decreases significantly compared to the mean frequency at other distances x. Such a behavior of the frequency corresponds to the one expected from equation 3.30 in which the characteristic length L_{res} can be substituted by the shock layer thickness h.

The influence of the parameters of the flow in the shock layer on the range of allowed frequencies are also remarkable. One of the characteristics of mass exchanges during oscillations of the shock layer is the gas density within the shock layer. Both, changes in the degree of off-design of the jet and changes of the mean pressure in the shock layer result in a change of the gas density in the shock layer. By comparing, Fig. 3.39-3.41 it can be seen that an increase in the degree of off-design n leads to a decrease in the mean frequency f_{max}. Furthermore, a decrease in the mean value of the plate-pressure corresponds to a change in the range of frequencies transmitted by the filter (see, for example, Fig. 3.39 curve 1 at distances $x \sim 7\text{-}9r_e$).

The direct influence of the shock layer ahead of the plate on flow oscillations produced by the impinging jet is also confirmed by phenomena which are related to the excitation of *low-frequency bursts* in the spectrogram. At distances x where *low-*

frequency bursts are visible in the spectrograms (e.g. at $x \approx 6.5r_e$ in Fig. 3.39) the pressure oscillogram consists of non-periodical pulses of different duration (similar as, for example, in Fig. 3.33). In these cases the spectrum has no pronounced peaks. The occurrence of low-frequency bursts corresponds remarkably well to those plate positions for which the amplitude of the plate-shock oscillations is maximal. For these plate positions a decrease in the level of sound produced by the impinging jet have been observed.

In Fig. 3.43*b* the range of values of the stand-off distance *h* of the plate shock is shown as a function of the nozzle-to-plate distance *x* in the range of $x \approx 6r_e$-$7r_e$ for an impinging jet with a degree of off-design $n = 0.76$. Parameters of the corresponding pressure oscillograms are depicted in Fig. 3.43*a*. First, the spectral amplitude of the 12-kHz spectral line which has been chosen to represent the magnitude of the low-frequency part of the spectrum is plotted. In addition spectrums of pressure oscillations at three nozzle-to-plate distances (A, B, C) are provided. In Fig. 3.43 it cab be seen that at a nozzle-to-plate distance of $x \approx 6.5r_e$, at which non-periodical pressure pulses occur, the corresponding spectrum (Fig. 3.43*a*-B) has no pronounced peak, and the level of low frequency components of the spectrum is increased in comparison with neighboring points. At the same distance, $x \approx 6.5r_e$, (Fig. 3.43*b*) the amplitude of the oscillating plate shock is maximal. Furthermore, as has been observed in the shadowgraphs, at this particular nozzle-to-plate distance the shape of the plate shock varies between a conical and a flat shape, while for other nozzle-to-plate distances the plate shock remains either conical or flat and only the stand-off distance *h* of the plate shock varies.
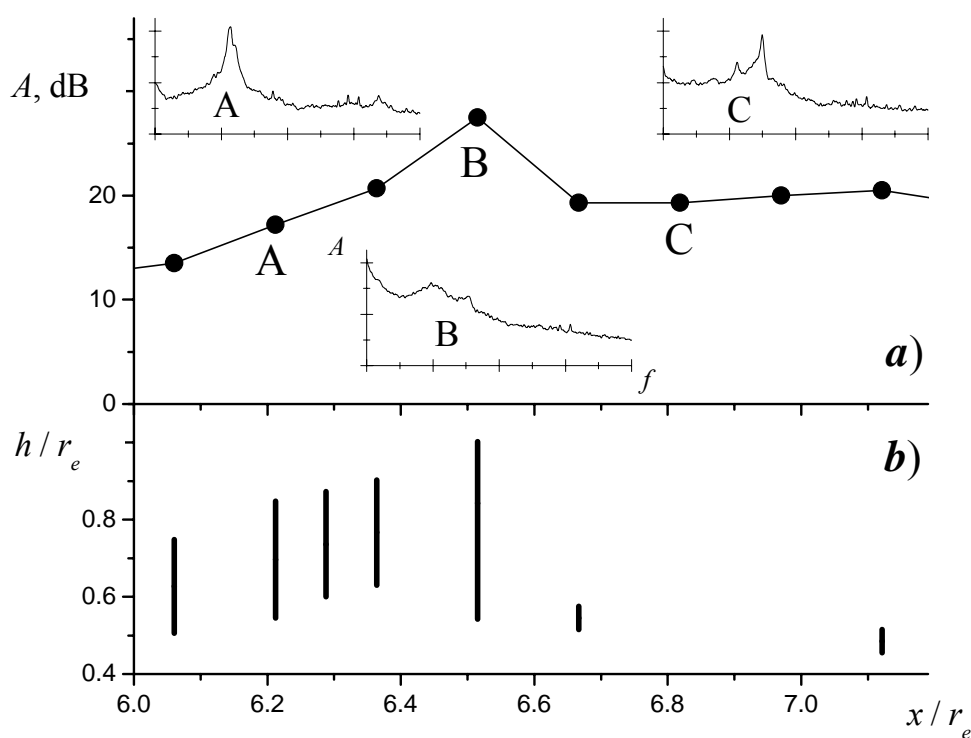

Fig. 3.43. Level of low-frequency oscillations of plate-pressure (*a*) and shock oscillations (*b*) as a function of nozzle-to-plate distances *x*. Sketches of spectrums are also shown in the top figure (*a*) at three different nozzle-to-plate distances (A, B, C).

In view of the above, the essential change in the behavior of the plate-pressure at position B can be explained by a change of the flow field in the shock layer due to a repetitive formation and destruction of recirculation bubbles. A growth of the recirculation bubble in the shock layer leads to an increase in the stand-off distance of the plate shock and, thus, to an increase in the thickness of the shock layer. This results in changes in the parameters of the resonance system which is represented by the shock layer. In particular, the frequency f_{res}, corresponding to eq. 3.30, decreases. At the same time necessary conditions for the existence of a recirculation bubble depend on the shape and position of the plate shock, as has been described in section 3.2.2. In this manner the process of bubble formation contributes directly to the process of impinging tone generation.

An estimate of the characteristic time of such processes confirms the explanation that low-frequency bursts are caused by a non-periodical formation and destruction of the recirculation bubble. Let us approximate the fraction of mass of gas participating in the pulsating process in relation to the entire mass of the gas in the recirculation zone. In order to simplify the theoretical model used in this estimate let us consider a cavity of length L, depth D, and width W that is driven by a flow of velocity u_∞. Oscillations of the shear layer are accompanied by a pulsating exchange of mass near the back edge of the cavity (Fig. 3.44). An analysis of such process has been given by Zapryagaev & Mironov (1987) as follows.
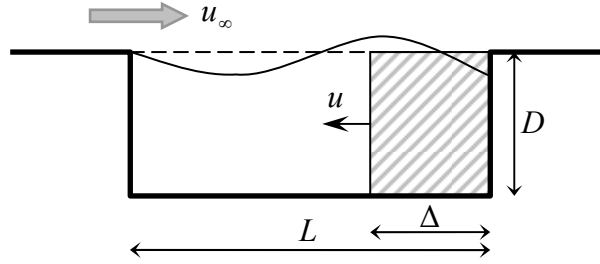
Fig. 3.44. Pulsating mass exchange in a driven cavity.

It is assumed that the mass δm of the gas participating in the mass exchange with the external flow occupies a volume V with a characteristic longitudinal dimension Δ. It follows from the continuity equation that

$$\frac{\delta m}{\delta t} = DW\left[\frac{\partial}{\partial t}\int_0^{\Delta(t)}\rho(x,t)\,\mathrm{d}x\right],\tag{3.31}$$

where ρ is the density of the gas in the cavity. The characteristic time δt of inflow (outflow) is given by $\delta t = 1/(2f)$, where f is the frequency of the oscillation. This allows us to evaluate the gas flow rate as

$$g = \frac{\delta m}{\delta t} = \frac{DW\rho_0\Delta}{\delta t} = 2\rho_0 DWf\Delta.\tag{3.32}$$

On the other hand, differentiation of the integral in eq. 3.31 gives

$$g = DW\left[\int_0^{\Delta}\frac{\partial\rho}{\partial t}\,\mathrm{d}x + \rho(\Delta,t)\frac{\partial\Delta}{\partial t}\right] \cong DW\left[\frac{2p_f f\Delta}{a_0^2} + \rho_0 u\right].\tag{3.33}$$

70

In eq. 3.32 and 3.33, we took $\rho = \rho_0$ (ρ_0 is the time-averaged density). Also,

$$u = \frac{\partial \Delta}{\partial t}, \quad \frac{\partial \rho}{\partial t} = \frac{1}{a_0^2}\frac{\partial p}{\partial t} \cong \frac{1}{a_0^2}\frac{p_f}{\delta t} = \frac{2p_f f}{a_0^2},$$ (3.34)

where a_0 is the speed of sound in the cavity and p_f is the amplitude of the pressure oscillation. We will assume that the inflowing gas forms a plane fluid piston whose velocity is equal to the acoustic velocity fluctuation u of the compression wave it generates. In a plane acoustic wave u and ρ are connected by the impedance relation

$$u = \frac{p_f}{\rho_0 a_0}.$$ (3.35)

Comparing eq. 3.32 and 3.33 and using eq. 3.35, we obtain an expression of the size of the mass transfer region

$$\Delta = \frac{p_f a_0}{2f\left(\rho_0 a_0^2 - p_f\right)}.$$ (3.36)

Let us apply this equation to oscillations of the recirculation bubble in the impingement zone ahead of the plate. The dimensionless quantity $\overline{\Delta} = \dfrac{\Delta}{L}$ characterizes the fraction of mass exchange, $\dfrac{\delta m}{m_0}$, connected with oscillations in the cavity. Assuming that in the recirculation bubble a_0 and ρ_0 are equal to the values of the stagnation parameters of the gas after a normal shock, and that the characteristic length L equals approximately the radius of the recirculation zone (in the present case this radius is about $r_e/2$, i.e., $L \approx 1.5$ mm), we calculated the value of $\overline{\Delta}$ for the case of an impinging jet having a degree of off-design of $n = 0.76$. Results of the estimate are shown in Table 3.2. In this as an amplitude p_f a measured mean value $p_f \approx 0.1 p_0$ is used.

Table 3.2. Estimate of the mass exchange in an oscillating recirculation bubble.

$a_0 \approx a_{03}$	$\rho_0 \approx \rho_{03}$	$p_f \approx 0.1 p_0$	$\overline{\Delta}, f = 30$ kHz	$\overline{\Delta}, f = 20$ kHz
350 m/s	10 kg/m^3	$2 \cdot 10^5$ Pa	0.7	1.1

As can be seen the mass exchange in a recirculation bubble due to an oscillating flow is significant. Thus, the size of the recirculation bubble and, respectively, the stand-off distance of the plate shock may change. For frequencies lower than $f_{lim} \approx 20\text{-}22$ kHz a recirculation bubble can completely be formed and destroyed in every half-period of the flow oscillation. The strong low-frequency pulsations of the shock location could lead to a change between conditions corresponding with a flow with and without a recirculation zone. Such pulsations have a non-periodic accidental character that results in the low-frequency bursts in the pressure spectrums and in the elimination of the resonance peak. Note that the limiting frequency f_{lim} coincides with the lowest existing frequency of the main peak which is assumed at those nozzle-to-plate distances that are close to the distance where low-frequency bursts occur (see spectrogram in Fig. 3.39).

To conclude, there are at least three types of impinging tone generation. The first one is connected with a spreading of flow instabilities through the jet core and shock layer. These oscillations are characterized by a strong dependence on shock layer parameters and are represented by the main peaks in the spectrograms. The second type of oscillations that is represented by secondary peaks in the spectrograms is due to instability waves propagating through the shear layer formed at the jet boundary. The third type of flow instabilities that occur only under particular conditions involves the unsteady trigger-like behavior of the recirculating flow occurring in the shock layer. Such pulsations have a non-periodic accidental character that result in the low-frequency bursts of the pressure spectrums and in an elimination of the resonance peaks.

It can be noted that the coexistence of the first two types of oscillations makes it difficult to distinguish them in experiments. This can explain some variances in experimental and theoretical data which can be found in the literature. In most cases authors assume only one type of oscillations combined with its harmonics, for example Tam & Ahuja (1990) and Krothapalli et al. (1999). However, as has been shown above, flow oscillations relating to mean and secondary peaks are independent of each other and can simultaneously exist in the impingement region. The dynamics of the recirculation bubble and its connection with the third type of flow oscillations has been studied for the first time here.

4. Particle dynamics at the flow impingement

Rigid particles of different powder materials that are carried by a supersonic jet issuing from a conical nozzle and the interaction of particle-laden jets with an obstacle are considered. Particles are added to the flow ahead of a converging-diverging nozzle and are accelerated by the expanding gas. After leaving the nozzle they move within the free jet and pass through shocks which are usually present because the gas is not normally ideally expanded by the conical nozzle. When the supersonic jet impinges on an obstacle a shock layer is formed with a bow shock ahead of it. Particles penetrate through this shock layer and impinge on the plate if their inertia is great enough. Upon impact particles can adhere to the surface or they are reflected from it.

In many technical processes, as for example in different methods of spray deposition, obtaining high velocities of particles that impinge on obstacles such as substrates, is of primary importance [Gilmore et al. 1999, Dykhuizen et al. 1999]. In order to accelerate particles up to velocities required, measures which are often conflicting with each other are taken. For example, an increase of the nozzle length leads to an increase of time available for particle acceleration thus resulting in an increase of the particle velocity. At the same time in a long nozzle the boundary layer grows to a greater thickness thus affecting the velocity characteristics of the gas flow adversely. Similarly, an increase of the stagnation density of the gas also results in two opposing effects: particles are accelerated more intensively in the nozzle, but in the shock layer ahead of the obstacle the deceleration is also greater. Also, particles of various densities and sizes behave in different ways. Heavy particles are less well accelerated than light ones, but due to their greater inertia they are also less well decelerated in the shock layer ahead of the substrate. This list of conflicting parameters can be continued.

In the following particle motions in the impinging flow will be studied theoretically and experimentally. Particle velocities calculated by using approximate methods will be compared with velocities determined experimentally. In addition, features of particle behavior in the thin shock layer ahead of an obstacle have been studied. In doing so the method of multi-exposure visualization described above is successfully applied to compressible two-phase flows.

4.1 Acceleration of particles by a gas flow

In this chapter the motion of rigid particles in supersonic gas flows is considered. A numerical method, the so-called Euler-Lagrange method, is applied to calculate the two-phase flow within the nozzle. Some features and limitations of the method are discussed. Results of computations are compared with measured values. Experimental data of the particle motion in the free supersonic jet are presented for various conditions, such as different stagnation parameters of the gas and particles of different size and density.

4.1.1 Equation of motion for a single particle in a gas flow

The force acting on a single particle moving through a fluid consists of a sum of several components: Stokes drag (an aerodynamic force), force due to pressure gradients, force due to an accelerating motion, Basset force, external forces (electromagnetic, gravity), etc. As has been shown [Sow 1967, Sommerfeld 1991, Sommerfeld 1994] under certain conditions the motion of rigid particles in a supersonic gas flow is determined by aerodynamic forces only and the other components are negligible. In this case the equation of motion for a single spherical particle is as follows:

$$m_p \frac{\mathrm{d}u_p}{\mathrm{d}t} = s_p C_d \frac{\rho(u - u_p)|u - u_p|}{2}. \tag{4.1}$$

Here u and u_p are the velocities of the gas and particle, ρ is the density of the gas, m_p and s_p are the mass and cross-sectional area of the particle, and $\mathrm{d}u_p/\mathrm{d}t$ is the particle acceleration. C_d is the effective aerodynamic drag coefficient. Assuming that the particle is of a spherical shape the parameters m_p and s_p can be calculated as follows:

$$m_p = \frac{4}{3}\pi \cdot r_p^3 \cdot \rho_p, \qquad s_p = \pi \cdot r_p^2, \tag{4.2}$$

where ρ_p is the density of the particle and r_p is the particle radius.

It is useful to introduce estimates of the process of equilibration between gas and particle velocities. Let us consider the case of an acceleration of a single particle in a constant gas flow, where $x_p(t=0) = 0$ and $u_p(t=0) = u_{p0} = 0$. Assuming a negligible change of the drag coefficient, the solution of eq. 4.1 gives the motion of a particle as function of the duration of stay in the flow as follows:

$$u_p(t) = u\left[1 - \frac{1}{\frac{t}{\tau_p}+1}\right], \qquad x_p(t) = u\tau_p\left[\frac{t}{\tau_p} - \ln\left(1 + \frac{t}{\tau_p}\right)\right], \tag{4.3}$$

where

$$\tau_p = \frac{8}{3} \cdot \frac{\rho_p}{\rho} \cdot \frac{r_p}{\Delta u \cdot C_d}. \tag{4.4}$$

Here parameter τ_p is a characteristic time of velocity relaxation. Δu is the difference between the initial velocities of the gas and particle in general, $\Delta u = |u - u_{p0}|$. When $u_{p0} = 0$ this equals $\Delta u = u$. Thus a characteristic length of velocity relaxation is given by:

$$\sigma_p = u\tau_p = \frac{8}{3} \cdot \frac{\rho_p}{\rho} \cdot \frac{r_p}{C_d}. \tag{4.5}$$

In the general case, for calculating two-phase flows, it is necessary to know an exact law of particle motion; in particular, the drag coefficient C_d needs to be known. The drag coefficient depends on many parameters such as the relative particle Reynolds and Mach number, the concentration of particles in the gas flow, the shape and surface quality of the particle and other parameters [Ceylan et al. 2001, Tran-Cong et al. 2003, Rein et al. 2003]. In practice, in order to evaluate the motion of rigid particles in a gas flow many theoretical and semi-empirical approximations of the unknown exact laws are made. In this a trade-off between the accuracy of the solution and computational

costs needs to be found. Such method is applied here in order to estimate numerically parameters of two-phase supersonic flows as described in the following.

4.1.2 Acceleration of particles in supersonic nozzles

The Euler-Lagrange approach (described in e.g. Sommerfeld 1991) allows to calculate numerically the two-phase flow in the cold spray nozzle. In this method it is assumed that the rigid particles have a negligible influence on the gas flow since the particle concentration is small. Based on this assumption the procedure is divided into two parts: calculation of the pure gas flow in the nozzle and, then, calculation of the motion of single particles within the steady (calculated) gas flow. A detailed description of the numerical method used in the present work can be found in Alkhimov et al. (2001). In this method, for obtaining the flow field of the gas the one-dimensional theory is used and all parameters depend on the axial coordinate x. The influence of the boundary layer is taken into account by subtracting the displacement thickness that is calculated as described in section 3.1.1 from the nozzle geometry. The particle motion is computed using eq. 4.1. The drag coefficient C_d is expressed as a function of the particle Reynolds number Re_p and Mach number M_p:

$$\mathrm{Re}_p = \frac{2r_p \rho |u - u_p|}{\mu}, \qquad \mathrm{M}_p = \frac{|u - u_p|}{a}, \qquad (4.6)$$

that are formed with the relative velocity between the gas and the particle. μ is the viscosity of the gas and a is the sound speed of the gas. Based on the Henderson's [Henderson 1976] semi-empirical correlation between C_d and Re_p and M_p is used:

$$C_{d,1} = \frac{24}{\mathrm{Re}_p + 4.17\mathrm{M}_p \sqrt{\gamma} \exp(-0.349\frac{\mathrm{Re}_p}{\mathrm{M}_p})} + 0.424\mathrm{M}_p \sqrt{\gamma}(1 - \exp(-\frac{\mathrm{M}_p}{\mathrm{Re}_p})) +$$

$$+ \left(\frac{4.5 + 0.38(0.03\mathrm{Re}_p + 0.48\sqrt{\mathrm{Re}_p})}{1 + 0.03\mathrm{Re}_p + 0.48\sqrt{\mathrm{Re}_p}} + 0.1\mathrm{M}_p^2 + 0.2\mathrm{M}_p^8\right)\exp(-0.5\frac{\mathrm{M}_p}{\sqrt{\mathrm{Re}_p}})$$

$$C_{d,2} = 0.9 + \frac{0.34}{\mathrm{M}_p^2} + 1.86\sqrt{\frac{\mathrm{M}_p}{\mathrm{Re}_p}}\left(2 + \frac{4}{\gamma \mathrm{M}_p^2} + \frac{1.496}{\mathrm{M}_p \sqrt{\gamma}} - \frac{0.25}{\gamma^2 \mathrm{M}_p^4}\right)\left(1 + 1.86\sqrt{\frac{\mathrm{M}_p}{\mathrm{Re}_p}}\right)^{-1}$$

$$C_d = \begin{cases} C_{d,1}, & \mathrm{M}_p \le 1 \\ C_{d,2}, & \mathrm{M}_p \ge 1.75 \\ C_{d,1}(1) + 1.33(\mathrm{M}_p - 1)(C_{d,2}(1.75) - C_{d,1}(1)), & 1 < \mathrm{M}_p < 1.75 \end{cases} \qquad (4.7)$$

Let us now consider results obtained by the Euler-Lagrange method. In order to compare numerical results with experimental data input-values of parameters were taken equal to parameters used in the experiments: geometry of the cold spray nozzle, stagnation pressure ($p_0 = 23$ bar) and stagnation temperature ($T_0 = 300$ K). In Fig. 4.1 - 4.2 gas and particle velocities, and the relative particle Mach number are shown as a function of the axial coordinate x. The origin of the coordinate x lies at the

critical section of the nozzle. Particles are injected upstream of the critical section. The initial velocity of the particles is supposed to be equal to the gas velocity. The nozzle length is given by $l_{nozzle} = 0.1$ m. Results of calculations are displayed for copper particles with radiuses ranging from 5 to 45 μm. It should be noted that in the experiments particles have never been spherical but irregularly shaped. Therefore, the radiuses considered in the calculation need to be taken as equivalent radiuses
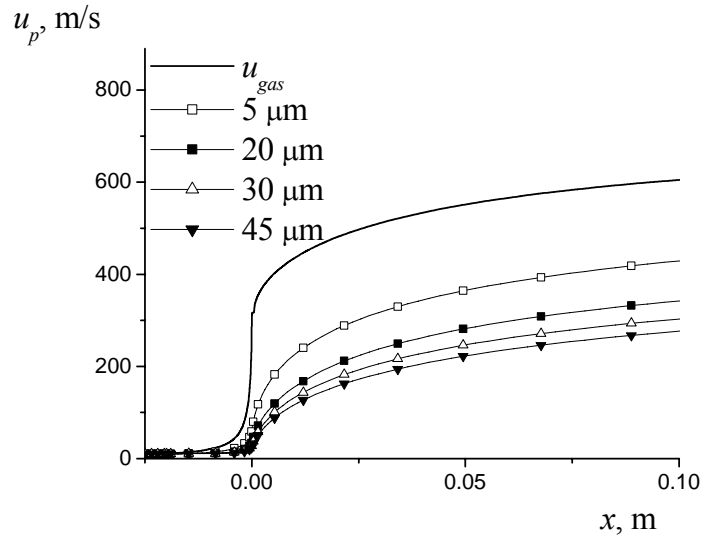

Fig. 4.1. Calculated gas and particle velocities in the nozzle as a function of the axial coordinate ($x = 0$ at the critical cross-section) for copper particles of different radiuses.
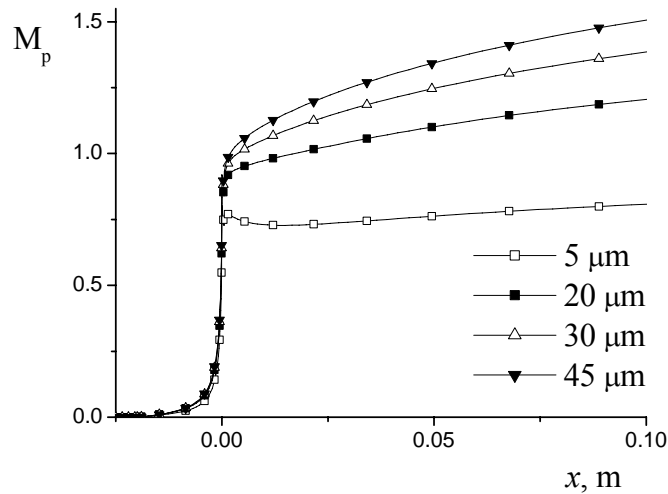

Fig. 4.2. Calculated relative Mach number in the nozzle as a function of the axial coordinate ($x = 0$ at the critical cross-section) for copper particles of different radiuses.

An essential velocity lag of particles in the gas flow is present even for small particles with radius of 5 μm. In order to accelerate particles up to high velocities a nozzle with a long diverging part (length of diverging part equals about 30 radiuses of the nozzle exit) has been used. Note that the relative particle Mach number is normally in the transonic regime. For this regime it is known that the drag of particles is very sensitive even to small flow inhomogeneities. In the nozzle flow such inhomogeneities are always present. Furthermore, in the present case particles are moving in the presence of many other particles. Hence, the acceleration of particles is sensitive to the presence of other particles in the flow in the transonic regimes. In Boiko et al. (2000, 2004) different configurations of particles in supersonic flows have been investigated. It has been shown that ahead of particles a collective bow shock can occur. Such collective effects change the acceleration of particles in the gas flow. In addition, it has been found that under certain conditions a transversal force occurs in a cloud of small particles accelerated by a gas flow. Due to this force the cloud spreads in a transversal direction relative to the gas flow. Hence collective effects do have an influence also on the radial distribution of particles in the jet.

As has been discussed above a general difficulty of calculating two-phase flows is to account for interactions between the two phases and rough approximations are normally introduced in order to save computational resources. Nevertheless, the applied method of calculation of particle velocities shows a good agreement with experimental data. Here, experimental data are available only outside the nozzle. A comparison of theoretical and experimental data will be given in the next section.

4.1.3 Investigation of two-phase flows issuing from a supersonic nozzle

Data of particle velocities were obtained by processing multi-exposure pictures of the two-phase flow as described in section 2.4.2. In Fig. 4.3-4.5 calculated and measured values of particle velocities are shown. The data were obtained under different conditions at a location on the axis of the jet at a distance $x = 4.3 \, r_e$ behind the nozzle exit. Particles having velocities within some range of values are present in the flow. The counts of measured particle velocities form a histogram which displays the distribution of values. Here and below such distributions are shown. Experimental data are represented by a velocity histogram that has been normalized by its maximum value and approximated by a Gaussian curve. In addition, the mean value of the velocity and the standard deviation are shown. In Fig. 4.3 velocities of particles having radiuses in different ranges and materials of different densities are depicted. The measurements were performed for particles of copper (Cu, $\rho_p = 7900 \, \text{kg/m}^3$) and aluminum (Al, $\rho_p = 2700 \, \text{kg/m}^3$) and radiuses in two different ranges ($r_p = 12\text{-}20 \, \mu\text{m}$ and $r_p = 30\text{-}45 \, \mu\text{m}$). The computation of particle velocities has been performed for particles having radiuses equaling the bounding values of these ranges. In all figures the calculated range of particle velocities is marked by a filled rectangular box. The general trend of the dependence of the velocity on particle size and material can be recognized from an analysis of the relaxation parameters (eqs. 4.4 - 4.5). The shorter is the relaxation time τ_p and length σ_p, the smaller is the velocity lag of particles relative to the gas flow, and, consequently, the absolute value of the particle velocity at the nozzle exit is greater. Hence, a decrease of the particle density ρ_p and/or the particle radius r_p results in an increase of the particle velocity, since the relaxation time decreases (eq. 4.4) when these quantities are decreased. This is well recognizable in Fig. 4.3
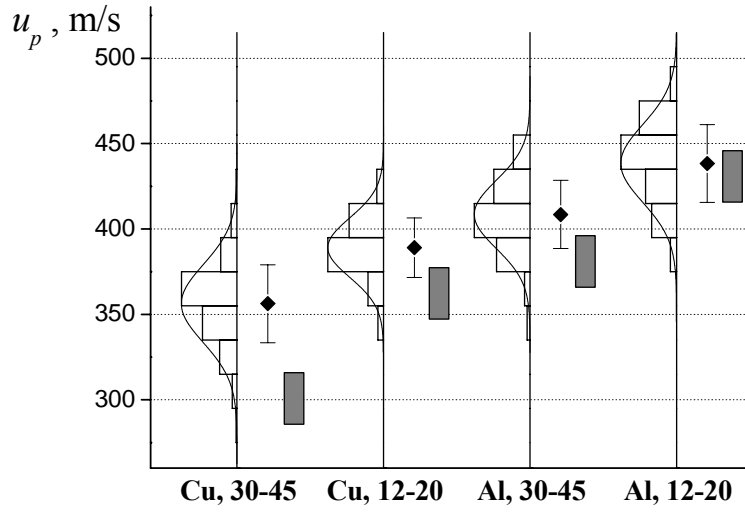
Fig. 4.3. Measured (histogram, mean value and standard deviation) and calculated (filled box) particle velocity u_p for copper (Cu) and aluminum (Al) particles. Radiuses in two ranges (r_p = 12-20 μm and r_p = 30-45 μm) are considered. The histograms are approximated by Gaussian curves.

In the same manner it is possible to explain changes in the particle velocity caused by changing the off-design degree n. In Fig. 4.4 the dependence of the velocity on the off-design degree n is shown for copper particles having a radius in the range of r_p = 20-30 μm. An increase of the off-design degree n, at otherwise same conditions, corresponds to an increase of the density ρ of the gas in the nozzle. This leads to a decrease of the relaxation time τ_p of the particle velocity (eq. 4.4). The corresponding by better acceleration of particles can well be seen in Fig. 4.4.

In Fig. 4.5 the particle velocity is shown as a function of the stagnation temperature T_0. The measurements were performed in a free jet which had an off-design degree of n = 0.8. Copper particles having radiuses in the range of r_p = 20-30 μm were used. The increase of the stagnation temperature T_0 causes an increase in the gas flow velocity. This also results in an increase of the particle velocity.

As can be seen in Fig. 4.3-4.5 the calculated velocities are always slightly smaller than the measured ones. This can be explained by the simplifying assumptions taken in the calculations, as described above. Nevertheless, considering the simplicity of the method, the numerical results mirror changes of particle velocity at different conditions well and, furthermore, the predicted values of the velocities are close to the measured values. The mean deviation of calculated particle velocities from experimental results is 10 % .

In the computations no account is taken of the non-uniformity of the radial distribution of different parameters of the two-phase flow. In the experiments, radial distributions of particle velocities and particle of a normalized concentration n_p were determined in the free jet at the same distance from the nozzle exit (x = 4.3r_e) as before. Copper particles with radiuses in the range of 20-30 μm were studied. In Fig. 4.6 the mean velocity and the standard deviation are presented as a function of the radial position r (normalized by the nozzle exit radius r_e). Similarly, the radial distribution of the normalized particle concentration is shown in Fig. 4.7 for the same location.
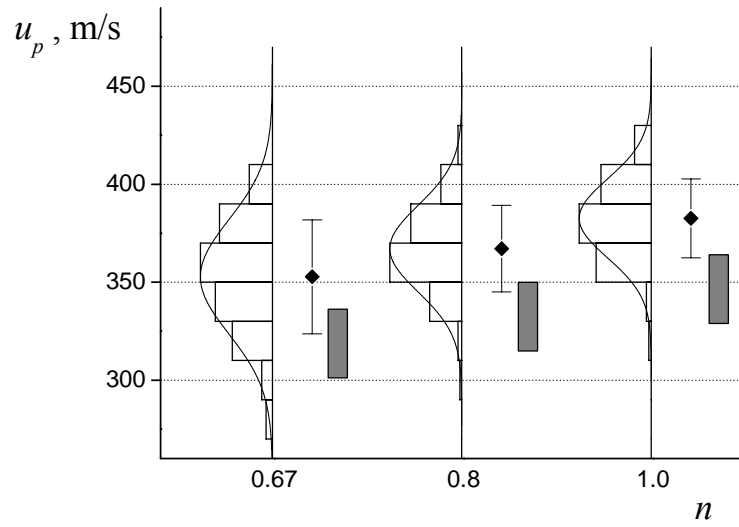
Fig. 4.4. Measured (histogram, mean value and standard deviation) and calculated (filled box) particle velocity u_p as a function of the degree of off-design of the jet, n. Particles of copper having radius of $r_p = 20 - 30$ μm were used. The histograms are approximated by Gaussian curves.
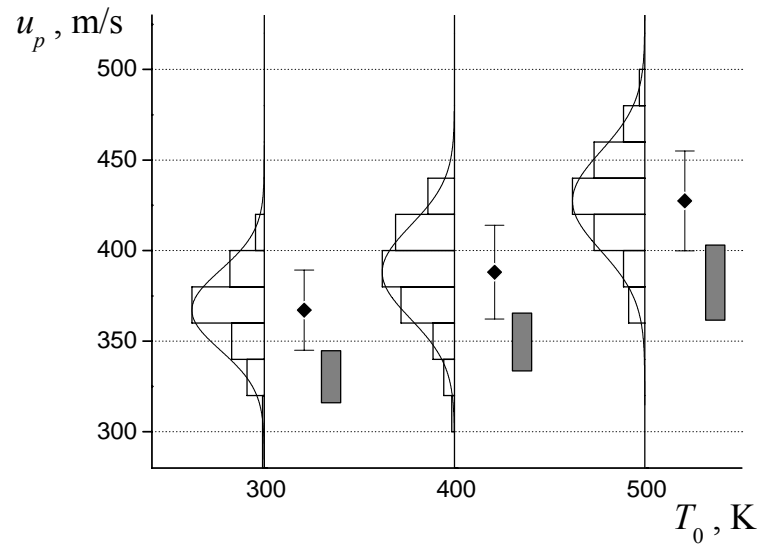

Fig. 4.5. Measured (histogram, mean value and standard deviation) and calculated (filled box) particle velocity u_p as a function of the stagnation temperature of the jet T_0. Particles of copper having radius of $20 - 30$ μm were used. The histograms are approximated by Gaussian curves.
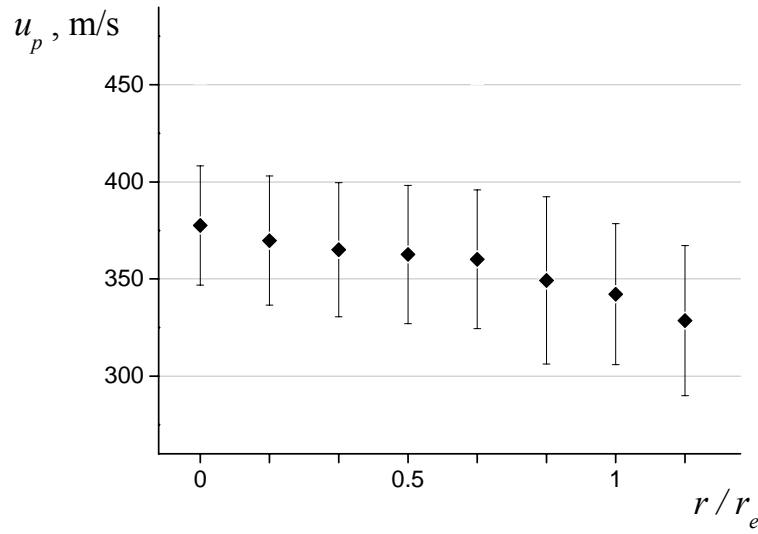
Fig. 4.6. Radial distribution of the velocity of particles (copper, $r_p = 20 - 30$ μm) in the free jet ($n = 0.8$) measured at $x = 4.3r_e$.
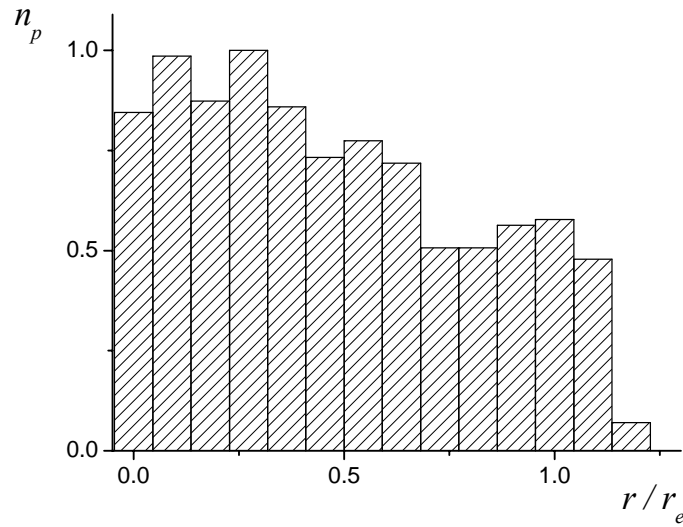
Fig. 4.7. Radial distribution of particles (copper, $r_p = 20 - 30$ μm) in the free jet ($n = 0.8$) measured at $x = 4.3r_e$. The particle concentration n_p is scaled by its maximum value.

The radial distributions of both, the velocity and the concentration of particles in the jet are close to uniform with a small decrease from the jet axis to the periphery. This is remarkable, in particular, for the particle concentration. Taking into account that particles are injected into the nozzle flow from a relatively small pipe on the axis of the flow, a statistical approach for estimating the particle distribution results in a Gaussian distribution rather than in a uniform one [Klinkov et al. 2004]. A possible explanation of the uniform distribution could be the influence of collective effects occurring in two-phase flows when particles move under transonic flow conditions (see chapter 4.1.2.).

4.2 Behavior of particles in the impingement zone

When a supersonic two-phase jet impinges onto an obstacle a bow shock is formed ahead of the obstacle. Behind the bow shock the gas flow is abruptly decelerated and becomes subsonic. Particles cannot follow the gas phase without a delay. After passing through the bow shock particles are slowly decelerated within the shock layer and if their inertia is large enough, they impact on the obstacle with a finite velocity. Depending on the conditions of the impact particles can adhere to the obstacle or they are reflected from the obstacle with some finite velocity. Reflected particles can again be accelerated by the gas towards the obstacle. The process of particle reflection is repeated until a particle adheres to the obstacle or moves out of the shock layer in the radial wall jet. In this manner a cloud of reflected particles can be formed ahead of the obstacle. When this cloud is thick enough incoming high-velocity particles can be scattered by the cloud. Therefore, the cloud of reflected particles can have an influence on the parameters of incoming particles and change the conditions of the first particle impact on the obstacle. The behavior of reflected particles depends on parameters describing the gas flow in the shock layer. In particular, it will be shown that an unsteady shock layer results in a change in time of the characteristics of the cloud. The high-speed multi-exposure shadowgraphy has been used to study the main characteristics of the behavior of particles within the shock layer ahead of the plate. In order to interpret the experimental results theoretical estimates of particle dynamics have also been obtained as is described in the following sections.

4.2.1 Deceleration of particles in the shock layer

Let us consider the motion of a single rigid particle in the flow field ahead of a plate at supersonic jet impingement. The influence of the plate shock on the particle motion is negligible since the time of interaction is short compared to the characteristic time of particle relaxation [Thomas et al. 1993, Sommerfeld & Decker 1995]. However, the particle decelerates in the shock layer which is characterized by a high density and a low velocity of the gas. Parameters of the gas flow in the shock layer can be evaluated by gas-dynamics (cf. chapter 3, eqs. 3.2-3.4, 3.15-3.18). As soon as the gas flow has been determined the motion of particles can be calculated by equations 4.1-4.2. For a first estimate the velocity u of the gas flow within the shock layer can be taken as zero. In this case the solution of equation 4.1 is as follows:

$$u_p(t) = \frac{u_{p0}}{\dfrac{t}{\tau_p} + 1},$$

(4.8)

$$x_p(t) = \sigma_p \cdot \ln\left(\frac{t}{\tau_p} + 1\right),$$

(4.9)

where u_{p0} is the initial velocity of the incoming particle. Here τ_p and σ_p are relaxation characteristics at zero gas velocity $u = 0$ (cf. eqs. 4.4-4.5):

$$\tau_p = \frac{8}{3} \cdot \frac{\rho_p}{\rho} \cdot \frac{r_p}{u_{p0} \cdot C_d},$$

(4.10)

$$\sigma_p = u_{p0} \cdot \tau_p = \frac{8}{3} \cdot \frac{\rho_p}{\rho} \cdot \frac{r_p}{C_d}. \qquad (4.11)$$

When the thickness of the shock layer is given by h, the residence time ($t_{res.in}$) of an incoming particle in the shock layer and the velocity ($u_{imp.in}$) of a particle right before impact on the plate can be evaluated from eqs. 4.8-4.9 as follows:

$$t_{res.in} = \tau_p \left(e^{\frac{h}{\sigma_p}} - 1 \right), \qquad (4.12)$$

$$u_{imp.in} = u_{p0} \cdot e^{-\frac{h}{\sigma_p}}. \qquad (4.13)$$

In Table 4.1 estimates relating to the motion of particles in the shock layer are presented for particles typically used in the experiments.

As can be seen in Table 4.1 the shock layer has a strong influence on small and light particles. Then, the relaxation length σ_p is comparable with the thickness of the shock layer h. The residence time $t_{res.in}$ of different particles is similar and equal to several microseconds for the given range of conditions. Thus, under conditions typically used in the present work, most of the particles reach the plate surface without being significantly influenced by the shock layer. The velocities of the particles remain practically the same as in the free jet ahead of the shock layer.

Table 4.1. Estimates of particle dynamics in the shock layer.

Parameters of the gas in the jet	$p_0 = 2.2 \cdot 10^6$ [Pa], $T_0 = 300$ [K], M = 2.78, $u_{gas.jet} = 605$ [m/s], $\rho_{gas.jet} = 2.5$ [kg/m^3]			
Parameters of the gas in the shock layer after the plate shock	$u_{gas.SL} = 167$ [m/s], $\rho_{gas.SL} = 9.1$ [kg/m^3]			
Parameters of the gas ahead of the plate	$u_{gas.plate} = 0$, $\rho_{gas.plate} = 10.3$ [kg/m^3]			
General parameters	$h_{SL} = 1.5$ [mm], $C_d \approx 1$			
	Different particles			
Material	Aluminium		Copper	
Density, ρ_p [kg/m^3]	2700		7900	
Radius, r_p [μm]	5	50	5	50
Relaxation parameters (in the shock layer)				
τ_p (eq. 4.10) [s]	$6.9 \cdot 10^{-6}$	$9.8 \cdot 10^{-5}$	$2.4 \cdot 10^{-5}$	$3.7 \cdot 10^{-4}$
σ_p (eq. 4.11) [m]	$3.5 \cdot 10^{-3}$	$3.5 \cdot 10^{-2}$	$1 \cdot 10^{-2}$	$1 \cdot 10^{-1}$
Deceleration in the shock layer				
Initial velocity (in free jet), u_{p0} [m/s]	510	360	435	275
$t_{res.in}$ (eq. 4.12) [s]	$3.7 \cdot 10^{-6}$	$4.3 \cdot 10^{-6}$	$3.7 \cdot 10^{-6}$	$5.5 \cdot 10^{-6}$
$u_{imp.in}$ (eq. 4.13) [m/s]	330	345	375	270
Coef. of deceleration [$u_{imp.in} / u_{p0}$]	0.65	0.96	0.86	0.99

4.2.2 Formation of a cloud of reflected particles ahead of the plate

Upon impact on a plate a particle can adhere to the surface or it can be reflected. In the latter case the kinetic energy of the particle can be reduced. It is possible to define a coefficient of restitution as the ratio of the particle velocity after and before the impact. The coefficient of restitution plays an important role in models of particle-obstacle adherence [Papyrin et al. 2003, Assadi et al. 2003, Van Steenkiste et al. 2002]. However it is difficult to determine this parameter. In theoretical work it is necessary to consider many phenomena such as a formation of dislocations in the materials, melting, plastic deformation and an influence of atomic forces. In order to determine the coefficient of restitution experimentally it is necessary to observe tracks of individual particles before and after a collision.

Let us consider the behavior of reflected particles. After impact reflected particles move upstream and can even penetrate trough the plate shock into the supersonic part of the jet. Whether a particle reaches the plate shock depends on its deceleration in the opposing gas flow and on its initial velocity that is determined by the coefficient of restitution and the impact velocity. The smallest values (critical) of the coefficient of restitution at which reflected particles just reach the plate shock have been calculated based on eqs. 4.1 and are presented in Table 4.2. Gas parameters in the shock layer and particle velocities before the impact are the same as in Table 4.1. Since normally no reflected particles are observed upstream of the plate shock this estimate of the coefficient of restitution provides an upper bound for this coefficient.

Under typical conditions as considered in table 4.2 the estimate shows that the value of the critical coefficient of restitution is quite small in a wide range of given particle parameters. Note that the time $t_{res.ref}$ needed for reflected particles to just move upstream to the shock is an order of magnitude larger than the residence time $t_{res.in}$ of incoming particles (compare Table 4.1 & 4.2). Therefore, reflected particles can accumulate in the shock layer and form a cloud ahead of the plate. Particles of the cloud are again accelerated towards the plate by the gas flow. The process of particle reflection is repeated until a particle sticks to the plate surface or is carried out of the shock layer by the radial wall jet.

When the cloud of reflected particles is dense enough incoming high-velocity particles can be scattered by this cloud. Therefore the cloud can influence the parameters of incoming particles and change conditions of particle impact on an obstacle. Characteristics and the dynamic behavior of the cloud of reflected particles have been studied experimentally. This is the subject of the next chapter.

Table 4.2. Estimates of relaxation parameters of reflected particles. Parameters of the gas flow in the shock layer are the same as in Table 4.1.

	Different particles			
Material	Aluminium		Copper	
Density, ρ_p [kg/m^3]	2700		7900	
Radius, r_p [μm]	5	50	5	50
Relaxation parameters (in the free jet)				
τ_p (eq. 4.4) [s]	$2.4 \cdot 10^{-5}$	$2.4 \cdot 10^{-4}$	$7 \cdot 10^{-5}$	$7 \cdot 10^{-4}$
σ_p (eq. 4.5) [m]	$1.4 \cdot 10^{-2}$	$1.4 \cdot 10^{-1}$	$4.2 \cdot 10^{-2}$	$4.2 \cdot 10^{-1}$
Deceleration in the shock layer after reflection				
$t_{res.ref}$ [s]	$1.3 \cdot 10^{-5}$	$5 \cdot 10^{-5}$	$2.5 \cdot 10^{-5}$	$9 \cdot 10^{-5}$
Critical coef. of restitution	0.4	0.12	0.22	0.09

4.2.3 Investigation of the cloud of reflected particles in steady shock layers

Multi-exposure shadowgraphs of the cloud of reflected particles have been obtained by the method described above in chapter 2.4. The diagnostic method of multi-exposure visualization is particularly well suited for studying processes in the thin shock layer ahead of a plate in supersonic impingement flows. By varying the number and duration of light pulses, and the intervals between individual pulses the motion of both, the bow shock and particles in the shock layer can be directly observed.

Except where noted otherwise all results presented below were obtained at the same flow parameters of the gas: the stagnation pressure and temperature equaled 22 bar and 300 K, respectively. At this stagnation pressure the jet is nearly ideally expanded. Particles of aluminium, copper, iron and zinc were used with a typical radius in the range of 5-50 μm. As an obstacle a steel plate with dimensions of 90 x 200 mm was used. At these conditions particles impinging onto the plate do not adhere to the plate surface and do not form a coating. This enables one to study particle-plate interaction under quasi-constant conditions.

Shadowgraphs have been taken under conditions where the flow is steady. In such cases the shadowgraphs clearly show that reflected particles usually remain in the shock layer and do not penetrate upstream through the plate shock. Only rarely, big particles can be observed upstream of the plate shock. Such particles can be distinguished from incoming particles due to their extremely small velocity and because a distinct bow shock is formed ahead of the particle. Frequently, the bow shock of such particles causes a disturbance of the plate shock. An example is given in Fig. 4.8. Note that in an unsteady shock layer the behavior of particles is different from that in steady shock layers. This is described in the next section.

The radial distribution of particles in the shock layer ahead of the surface has been evaluated from photographs such as Fig. 4.8. The particle concentration n_p (normalized by its maximum value) is presented in Fig. 4.9. The plate was placed normal to the jet axis behind the nozzle exit at the same location ($x = 4.3 \cdot r_e$) where measurements were performed in the free jet (cf. Fig. 4.7). Furthermore, the histogram is again based on copper particles having radiuses in the range of 20-30 μm. These two histograms can, therefore, be directly compared. In the shock layer the radial distribution of reflected particles is rather Gaussian than uniform as it has been the case for particles in the free jet. Such a non-uniform distribution of particles in the cloud ahead of the plate can be expected for two reasons. The first one is that the diameter of the jet is relatively small and particles are reflected from the surface into random directions. The second reason is that particles from the periphery are carried out of the field of view by the radial wall jet. Both mechanisms of a redistribution of particles are not present in the free jet.
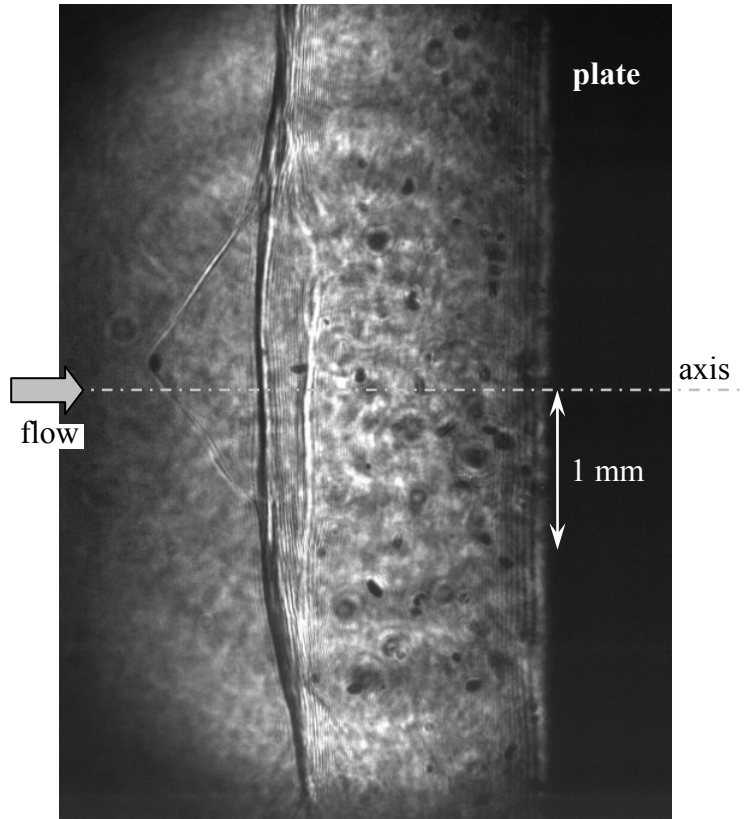
Fig. 4.8. Shadowgraph of particles in a steady shock layer showing also a single reflected particle upstream of the shock ahead of the plate.
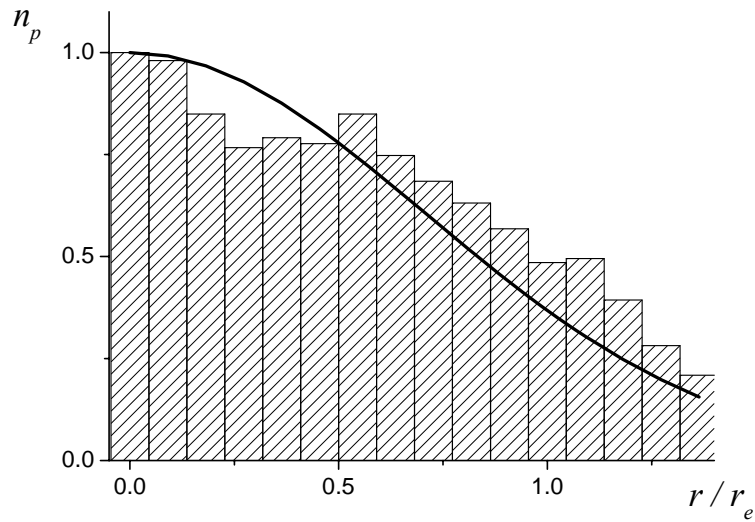

Fig. 4.9. Radial distribution of reflected particles (copper, $r_p = 20 - 30$ μm) in the steady shock layer. A Gaussian curve is fitted to the data.
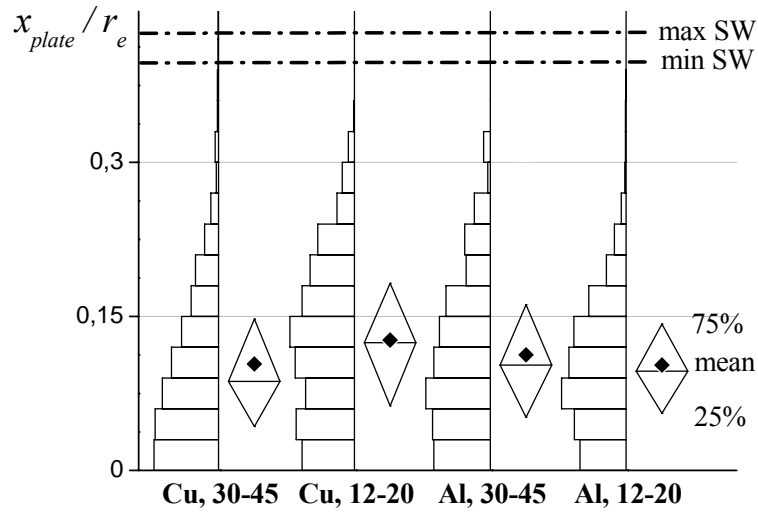
Fig. 4.10. Axial distribution of particles of different size and density within the steady shock layer. Quartiles of particle distributions and maximum (max SW) and minimum (min SW) locations of the shock are also shown.
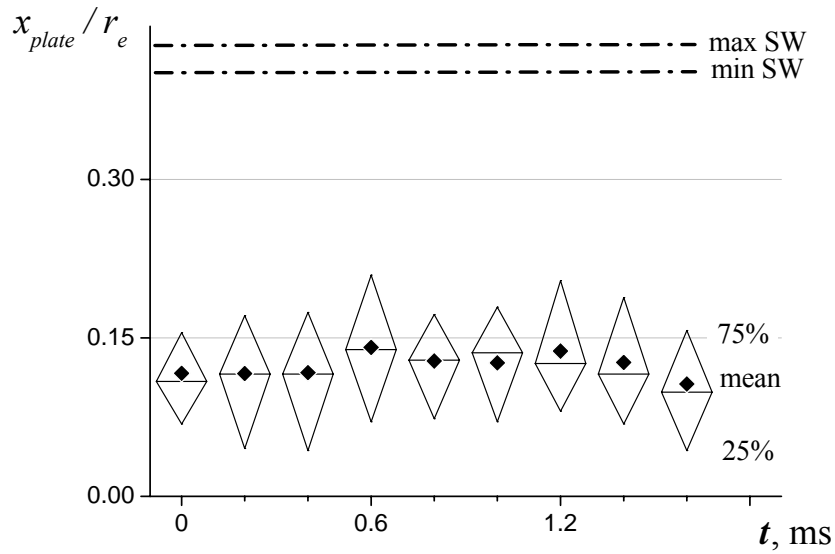

Fig. 4.11. Variation in time of the axial distribution of copper particles ($r_p = 20 - 30$ μm) in a steady shock layer. Quartiles of particle distributions and maximum (max SW) and minimum (min SW) locations of the shock are also shown.

The concentration of particles in the cloud ahead of the plate has also been determined as a function of the distance x_{plate} from the plate ($r \in [0, 0.5r_e]$). Results obtained for particles of different materials and sizes are shown in Fig. 4.10. In addition to the histograms, quartiles and mean values of the distributions are presented. The nozzle-to-plate distance ($x \approx 4\ r_e$) corresponds to the position of the cross-section where measurements of particle velocities were performed in the free jet (cf. chapter 4.1.3). At this location of the plate the plane plate-shock did not significantly change its shape and position in time. Only weak fluctuations of the plate shock about its mean position occurred. The dash-dotted line indicates the minimum and maximum position of the plate shock. As can well be seen a particle cloud is formed in the shock layer close to the wall. In the steady shock layer particles of different size and density are distributed in the same manner. Furthermore, the distribution does not change in time (cf. Fig. 4.11). Small differences can be explained by fluctuations in the flow and by a random distribution of particles after reflection.

In this manner quantitative estimates of particle concentrations in the jet and in the cloud have been obtained. In Table 4.3 data relating to reflected particles in the shock layer are compared with data for particles in the free jet. As can be seen, within the cloud the concentration of particles is one to two orders of magnitude greater than in the impinging jet. Nevertheless, the probability of a collision between incoming and reflected particles is low since the absolute quantity of reflected particles in the shock layer is small. Hence the cloud of reflected particles ahead of the plate has no direct influence on the incoming particles under these conditions.

4.2.4 Investigation of the behavior of reflected particles in oscillatory flows

Let us now consider characteristic features of the behavior of particles in the impingement zone of non-ideally expanded jets under conditions resulting in unsteady flows. Emphases will be laid on variations in time of the properties of the cloud of reflected particles in the unsteady shock layer. As was described in chapter 3, when the distance between nozzle exit and plate is changed while the stagnation conditions are kept constant a recirculation bubble can occur in the shock layer at certain nozzle-to-plate distances. In this case the flow ahead of the plate as well as shape and position of the bow shock oscillate strongly. This happens, for example, when the plate is located at a distance of $x = 6.2\ r_e$ behind the nozzle exit. The behavior of reflected particles in the cloud ahead of the plate also changes essentially. This was studied for the case of standard flow conditions which were described in sections 4.1.3 and 4.2.3 ($n = 0.8$, $T_0 = 300$). Particles of different density ($\rho_p = 2700\text{-}7900\ \text{kg/m}^3$) and size ($r_p = 10\text{-}50\ \mu\text{m}$) show similar behavior. The experimental results for the case of copper particles having radiuses in the range of $r_p = 20\text{-}30$ are presented below in this section.

Table 4.3. Comparison of the concentration of particles in the shock layer and in the impinging jet.

	Different particles			
Material	Aluminium		Copper	
Density, ρ_p [kg/m^3]	2700		7900	
Radius, r_p [μm]	12-20	30-45	12-20	30-45
Mass, m_p [kg]	$3.8 \cdot 10^{-11}$	$4.9 \cdot 10^{-10}$	$1.1 \cdot 10^{-10}$	$1.4 \cdot 10^{-9}$
Parameters in the impinging jet ahead of the shock layer				
Velocity, u_p [m/s]	435	415	390	360
Concentration [1/m^3]	$2 \cdot 10^8$	$5.4 \cdot 10^7$	$8.3 \cdot 10^8$	$3.3 \cdot 10^8$
Particle flux density [1/m^2·s]	$8.7 \cdot 10^{10}$	$2.3 \cdot 10^{10}$	$3.3 \cdot 10^{11}$	$1.2 \cdot 10^{11}$
Particle flux in jet [1/S_e·s] *1	$3 \cdot 10^6$	$0.8 \cdot 10^6$	$11 \cdot 10^6$	$4 \cdot 10^6$
Mass flux in jet [kg/S_e·h]	0.4	1.3	4.3	20.4
Parameters in the shock layer				
Concentration [1/m^3]	$3.5 \cdot 10^9$	$1.2 \cdot 10^9$	$9.5 \cdot 10^9$	$2.3 \cdot 10^9$
Surface concentration [1/S_e] *2	120	40	325	80
Probability of collision *3	0.1	0.2	0.3	0.4

*1 – mean number of particles traversing the cross-section at the nozzle exit S_e in one second;

*2 – mean number of particles located within the shock layer, the cross-sectional area of which equals to the cross-sectional area of the nozzle exit S_e;

*3 – probability of collision between incoming particles and reflected particles in the shock layer; parameter is represented by a ratio $\sum 4s_p / S_e$, where s_p is the cross-sectional area of a particle.
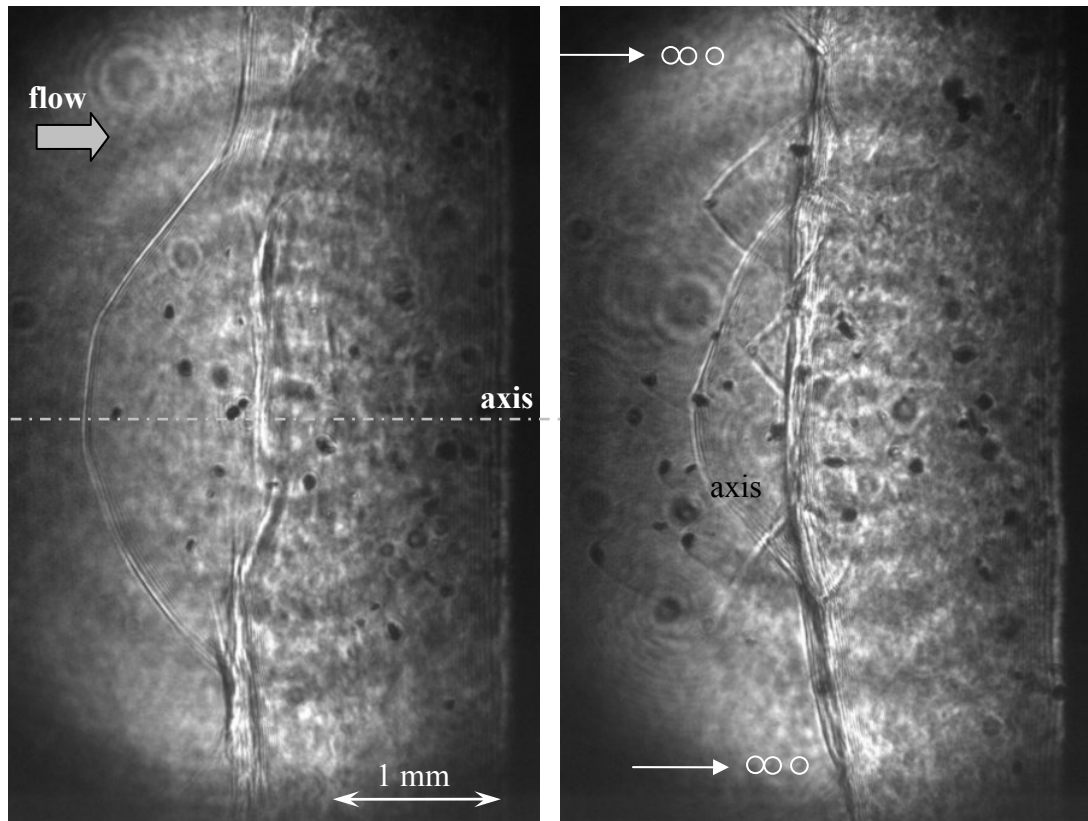
Fig. 4.12. Three-exposure shadowgraphs of particles in the unsteady shock layer at different phases of the plate-shock oscillation: convex plate shock (left) and plane shock (right). Exposures of two incident particles have been circled on the right picture.

In Fig. 4.12 typical shadowgraphs of reflected particles in the unsteady shock layer are shown at different stages of the motion of the plate shock. In Fig. 4.12*a* the distribution of particles is similar to the one in a steady situation and all particles are located within the shock layer although the shape of the plate shock is not flat. In Fig. 4.12*b* the plate shock is flat but now many particles are observed upstream of the shock in the supersonic jet. These shadowgraphs are three-exposure pictures. High-velocity particles are thus represented by a track of three images. Such tracks are marked by white circles in Fig. 4.12*b*. Upstream of the shock there are also particles that have just one image. Typically, in this case a bow shock can be seen ahead of the particle. It is obvious that such particles are slow and have moved to this location after having been reflected from the plate. Note that conditions of particle impact on the plate surface practically do not change when the nozzle-to-plate distance x is changed. In the preceding chapter we have shown that in steady flows reflected particles do not normally penetrate through the plate shock. There is thus no reason for reflected particles to reach the shock and, particularly, penetrate far upstream of the shock in unsteady flows.
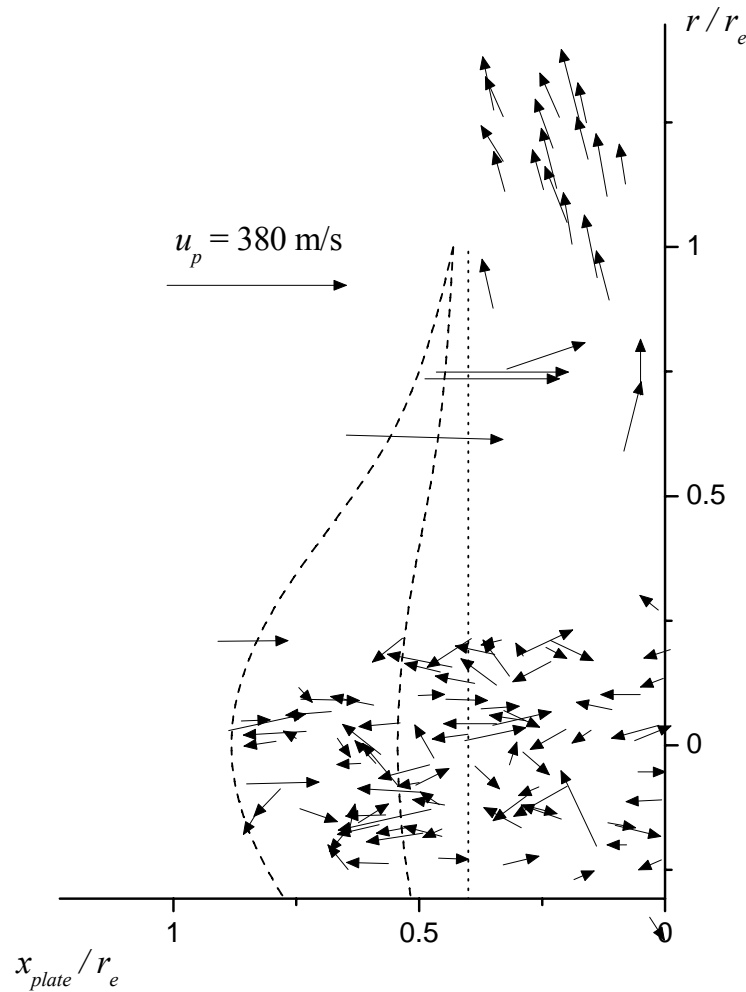
Fig. 4.13. Particle motion in an unsteady shock layer. Note that a great number of (reflected) particles move upstream. The extreme positions of the oscillating plate shock are indicated by dashed lines. The position of a plane steady shock (dotted lines) is also drawn.

In Fig. 4.13 information about the unsteady behavior of both, particles and the plate shock is summarized. Vectors of particle velocities and extreme positions of the plate shock are shown. For reference, the position of a plane steady shock is also drawn. Data are plotted in relative coordinates along (x_{plate}) and across (r) the jet axis. The mean velocity ($u_p = 380$ m/s) of the particles in the free jet is provided as a reference length. In the experiments copper particles were used having a radius of $r_p = 20\text{-}30$ μm. Note that data could not be obtained in that regions of the shock layer where the turbulent shear layer is present. This is due to density fluctuations disturbing the observation of particles.

As can be seen, in the particle cloud particles typically have a small velocity only and all directions of motion are present. This points at iterated reflections of particles at the plate and at interactions of particles with each other. The presence of low-velocity particles which move to the plate surface is obvious. Also particle tracks are recognizable at the plate surface as well as in the wall jet region in periphery. This shows that reflected particles do not always move radially out of the shock layer but can impact the plate more than once.
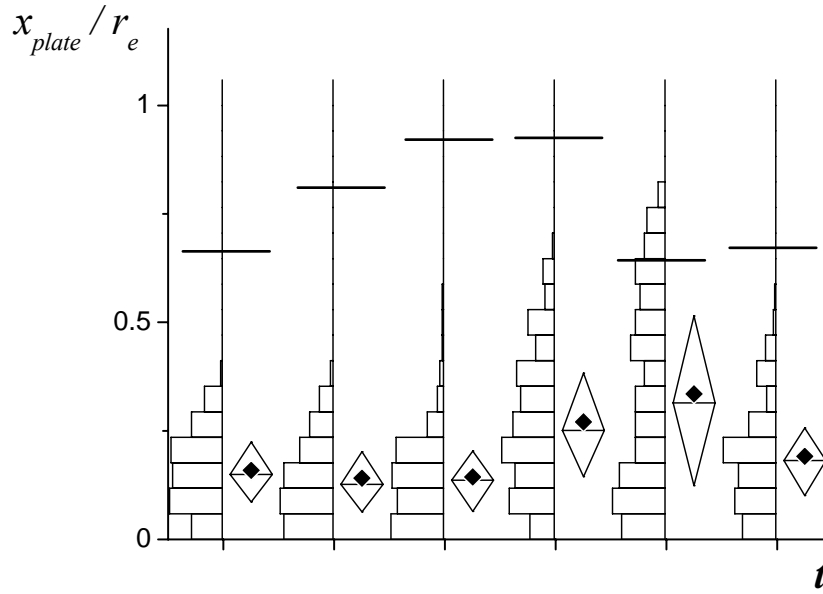
Fig. 4.14. Variation in time of the axial distribution of reflected particles in an unsteady shock layer (qualitative time dependence). Quartiles of particle distributions and locations of the shock (horizontal solid lines) are also shown.

Variations in time of the axial distribution of reflected particles in the unsteady shock layer are shown in Fig. 4.14. It can be seen that the particles are normally confined within the shock layer and stay close to the plate. However, at a time when the shock approaches the plate, reflected particles are also present upstream of the plate shock. From our experiments it is known that the motion of the shock corresponds to a change of the shock shape from convex to flat. As has been shown in chapter 3, this behavior of the plate shock is connected with the formation and destruction of a recirculation bubble in the shock layer.

Based on these observations the following explanation of the penetration of reflected particles into the flow upstream of the shock has been developed. The model is based on the oscillating shock and the periodic formation and destruction of a recirculation bubble in the shock layer. In Fig. 4.15 the oscillating shock layer with particles is shown at different times. In these pictures real positions of particles and the plate shock are represented by consequent stages taken from shadowgraphs. In the first picture (Fig. 4.15a) the distribution of particles is similar to the one of a steady flow situation. Particles form a cloud ahead of the plate surface. Then (Fig. 4.15b) a recirculation flow occurs in the shock layer. The shape of the plate shock is changed from flat to convex and, at the same time, the recirculation bubble grows. Due to changes in the flow field the cloud of reflected particles becomes extended over the whole thickness of the shock layer (Fig. 4.15c). In particular, particles are carried to the plate shock by the recirculating flow. In the final stage of the oscillation the shock approaches the plate and the shock-layer thickness decreases abruptly. The velocity of the reflected particles is small and, at least partly, directed upstream. Therefore, the particles remain upstream of the shock for some times (Fig. 4.15d). Only later they become accelerated by the flow and approach the plate anew.
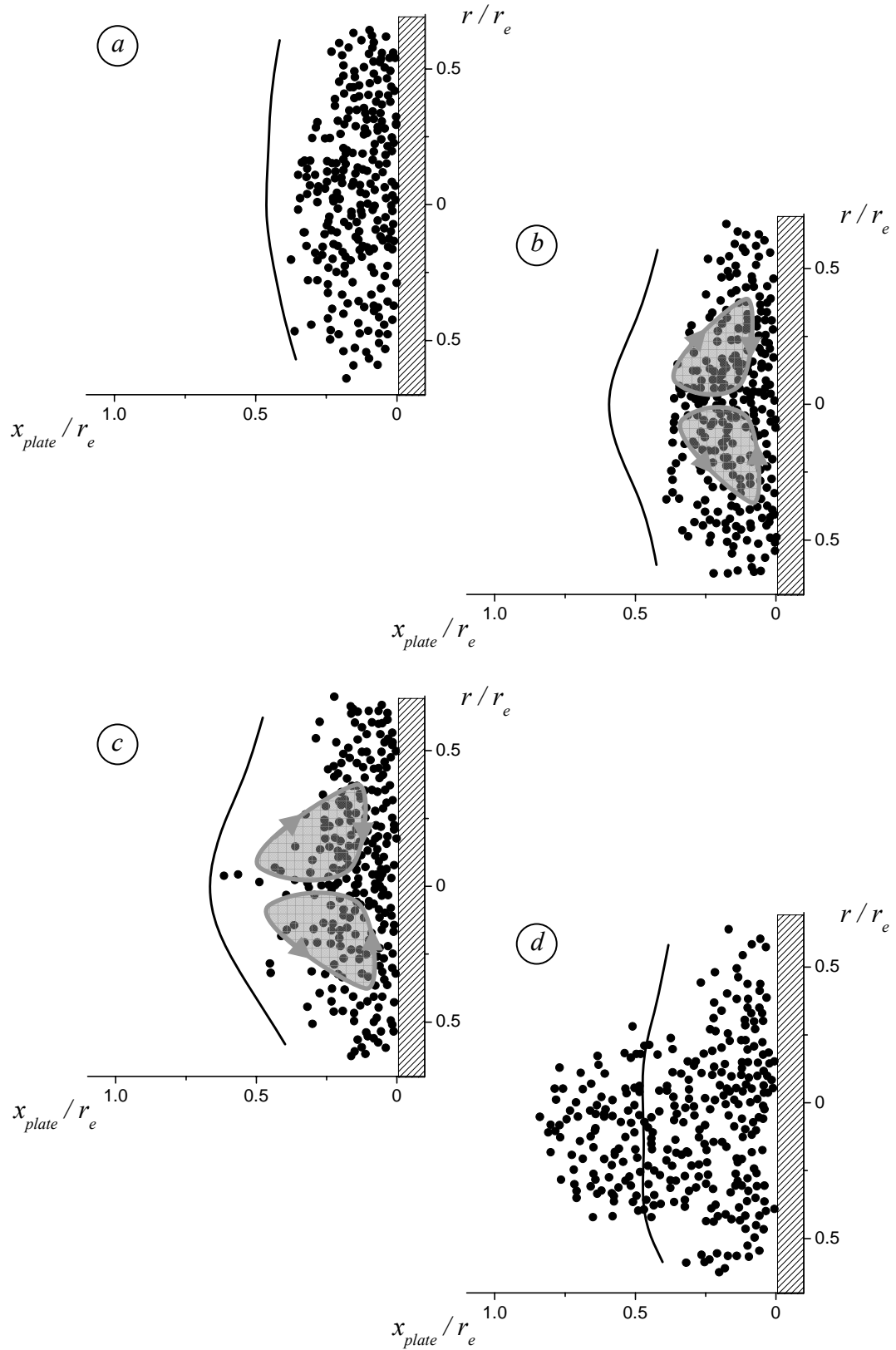
Fig. 4.15. Sketch of different phases of an oscillating shock layer with a recirculation bubble. Measured locations of reflected particles (points) and the plate shock (solid lines) are shown together with qualitative images (gray regions) of the recirculating flow.

94

A comparison of characteristic times of the shock oscillation and relaxation times of the particles agrees with this mechanism for non-regular low frequency shock pulsations. At the conditions of the experiments they happen, for example, when the plate is located at a distance of $x = 6.2\, r_e$ behind the nozzle exit. The same regime of plate-shock pulsations was considered in chapter 3.3. At slightly different conditions (cf. chapter 3.3) non-regular shock pulsations occur for a nozzle-to plate distance of $x = 6.5\, r_e$ (cf. Fig. 3.43)). The frequency of these oscillations is much smaller than 20 kHz. Hence, the interval between two successive shock pulses (cf. Fig 3.33e) is greater than the characteristic time of particle motion in the shock layer which equals $\tau_{res.ref} = 25\text{-}90\ \mu s$ (cf. Table 4.2). Therefore, the particle cloud has enough time to expand and fill the whole space between the upstream moving shock and the plate. When the shock moves back towards the plate the shock is very fast. Measured velocities of the plate shock reach up to values of $u_{SL} \approx 100$ m/s. Hence, it takes the shock about 10 μs to change its position. This time is much shorter than the relaxation time of particles in the impinging jet (cf. Table 4.2). Thus, particles remain upstream of the plate shock in the supersonic flow for some time until they reach the shock layer again.

In conclusion, let us discuss the importance of the results for one of the applications. In some processes, such as cold spray deposition, considering particle-substrate impacts is important. In models describing these processes the influence of reflected particles is normally considered to be negligible [Papyrin et al. 2003]. Indeed, the cloud of reflected particles has most likely no *direct* influence on incoming particles. However reflected particles can still play an essential part in the process of particle-obstacle interactions. Since reflected particles are carried by a gas flow they can impact on the plate surface repeatedly. Each subsequent particle-surface interaction occurs under different conditions. At the first impact particles have a high velocity. For this reason they remain in the shock layer for a short time and parameters of particles do not change under the influence of the shock layer. Particularly, the temperature of the gas in the shock layer is much higher than in the impinging jet. But the temperature of particles does not increase essentially on traversing of the shock layer for the first time [Alkhimov et al. 2000a, 2001]. In contrast with that, reflected particles have a long-term exposure to high temperatures in the shock layer. Furthermore, parameters of the particle change during an impact. Particles are deformed, adhesive properties of the surface are changed and the temperature is increased so that the particle can be melted locally or even completely. Thus the properties of reflected particles differ from that of newly incoming particles more than in the velocity. Conditions for the particle-plate interactions are totally different. Based on this it seems to be reasonable to account for the interaction between obstacles and reflected particles.

5. Particle-plate interactions

The interaction of particles and the substrate forms the final integral part of the general problem considered here, namely, the interaction between multi-phase jets and obstacles. In many practical applications, such as spray deposition or erosion, the interaction between particles and a substrate determines the quality of the whole process. Furthermore, on the one hand, the behavior of particle-laden impinging jets depends on results of particle impacts on the obstacle; on the other hand, characteristics of the particle-obstacle interaction are connected with parameters of the impinging flow. This interdependency is the reason why some interesting features of particle-substrate interactions will be considered in this chapter.

First, growth rate and shape of coatings that can be produced during long-term exposures of substrates to high-velocity particle flows are studied. Experimental results are presented for different materials and conditions of the impinging flow.

Second, it has been observed experimentally that under certain conditions light is emitted from the impingement region when particle laden jets are directed against the surface of a substrate. It is shown that the phenomenon of luminescence is caused by particle impacts. Preliminary experimental results obtained under different conditions of particle impacts are presented and mechanisms of the source of the luminescence are discussed.

5.1 Growth rate and shape of coatings

In this chapter we consider the interaction between particle-laden jets and substrates under conditions that result in the formation of a coating on the surface of the substrate. Impinging particles adhere to the substrate when the impact velocity of particles exceeds a threshold. Therefore, in the following only experimental conditions are considered that result in sufficiently high particle velocities. In order to study the importance of different material properties we consider situations in which the substrate is not moved and the particle laden jet impinges on the same region of the surface of the substrate. In this case a cone-shaped coating is formed, the shape being similar to the one which is formed when sand falls on a horizontal surface. The Cold Spray facility used has a supersonic nozzle with a circular cross-section. Thus a frustum-like or whole cone-shaped coating is produced when a two-phase jet is directed against a fixed flat substrate. High-speed shadowgraphy clearly shows one common feature of the coatings produced: a flat top. Several successive stages of the process of coating growth are shown in Fig. 5.1. Here, a flat plate of aluminium has been positioned in a gas flow with aluminium powder at a fixed nozzle-to-plate distance of $x = 6r_e$. The formed lump has the shape of a conical frustum with the base lying on the plate surface during all times of the coating growth. The height of the cone (or the thickness of the coating, h_{coat}) increases but the top of the cone remains flat until the cone becomes a pointed cone. A similar behavior has been observed for a wide range of conditions: different nozzle-to-substrate distances ($x = 4\text{-}12 \cdot r_e$), different stagnation temperatures of the gas flow ($T_0 = 300 - 650$ K), different materials of both, powder and substrate (Al, Fe, Cu, Zn).
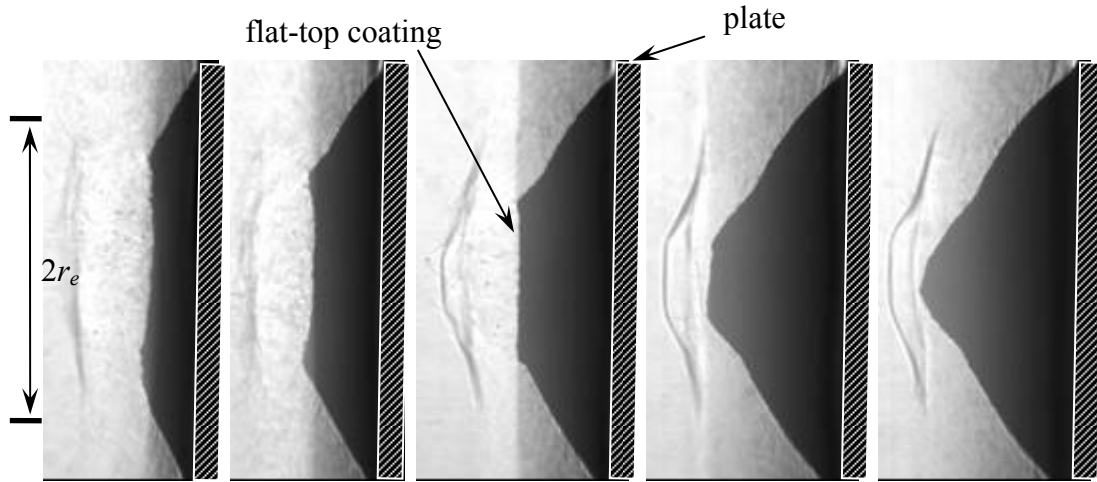
Fig. 5.1. Growth of a flat top coating (aluminium on an aluminium substrate): time increases from left to right. Particles (r_p = 5-50 μm) were accelerated by a gas jet having a flow Mach number of M = 2.8 and a degree of off-design n = 0.8. The nozzle-to-plate distance equals $x = 6r_e$.

Note the appearance of a so-called optical ghost in the digital photographs of Fig. 5.1. The optical ghost can particularly well be seen in the middle photograph of Fig. 5.1: on the left side of the image the gaseous phase is reproduced much brighter than on the right side. This ghost is caused by an effect based on a not complete charge removal on the CCD-chip. A detailed description of this phenomena can be found in the technical documentation of the CCD-camera ["PCO CCD imaging" company] (cf. chapter 2).

The flat shape of the growing coatings conforms to the distribution of particles in the impinging two-phase flow. As has been shown in chapter 4.1 the radial distribution of the particle concentration and velocity in the impinging jet is close to uniform at nozzle-to-plate distances used in the present coating experiments ($x = 4$-$12 \cdot r_e$). When it is assumed that the particle velocity and concentration determine the formation of a coating, a uniform radial distribution of the probability of particle adherence is to be expected. Thus the thickness, h_{coat}, of the coating should be constant in space everywhere except for the peripheral region of the impinging jet. At the boundary of the jet a mixing layer is formed in which the flow velocity is smaller than in the jet core. The conical shape is caused by "border" effects. It is clear that at the edge of the flat region conditions of particle adherence differ essentially from conditions relating to normal impact. Also, the probability of particle bonding on oblique surfaces is smaller than on plane surface since the normal component of the particle velocity, which is most important for obtaining adherence, decreases in this case.
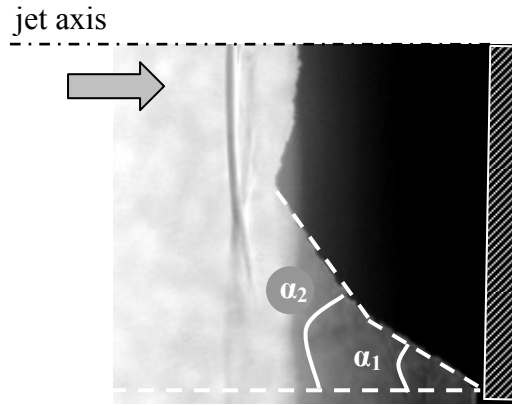
Fig. 5.2. Angles of the frustum formed by the coating layer: definitions.

We will now divide the surface of the cone formed during the coating process into three different conditional regions. The first one is the flat top where normal impacts of particles dominate. The second and third regions are different parts of the mantle of the frustum. Because the properties of the impinging flow are different in the core and the shear layer of the jet, the inclination of the cone varies. It is known that the probability of particle adherence decreases when the normal component of the impact velocity decreases. Therefore, at the same absolute value of the impact velocity particles stick most likely to the surface at normal impacts rather than at oblique ones. We now introduce the angle α between the mantle of the cone and the axis of the jet. The axis is practically equal to the direction of particle impingement. Typically, two angles can be discerned relating to the jet core and the shear layer. In Fig. 5.2 these angles are marked as α_2 (jet core) and α_1 (shear layer). Note that the separation between these two parts of the mantle of the cone is not sharp and that there is a smooth transition between them. Nevertheless, in most cases the two parts of the cone can be clearly distinguished.

It is interesting to compare shapes of coating cones formed by different materials. In Fig. 5.3-5.4 the dynamics of growing cones is shown for different powders. Except for using different powders the conditions were the same in all cases ($M = 2.8$, $n \approx 1.0$, $x \approx 8r_e$). In Fig. 5.3 the dependence on time of the angles α_1 and α_2 are shown for powder particles of aluminium, copper and zinc. Vertical solid lines indicate those times at which the area of the flat top of the coating cone has decreased to zero. In the experiments it has been observed, that after the flat top has disappeared the growth becomes slower and finally comes to a stop. Thereafter the inclination of the cone does not change.

Except for some sorts of aluminium, the behavior described in the last paragraph has been observed for all powders of zinc, copper and aluminium used in the experiments. In Fig. 5.5 shadowgraphs of coating cones are shown for the case where the growth has practically stopped (copper and zinc) and for the case of aluminium powder where the cone is still growing. Some aluminium powders show an extremely high capability of forming coating cones. In these cases the cone grew to a size larger than the field of view of the optical system. When this happened the process of coating was stopped for technical reasons. In Fig. 5.3-5.4 the experimental data are presented for such aluminium powder.
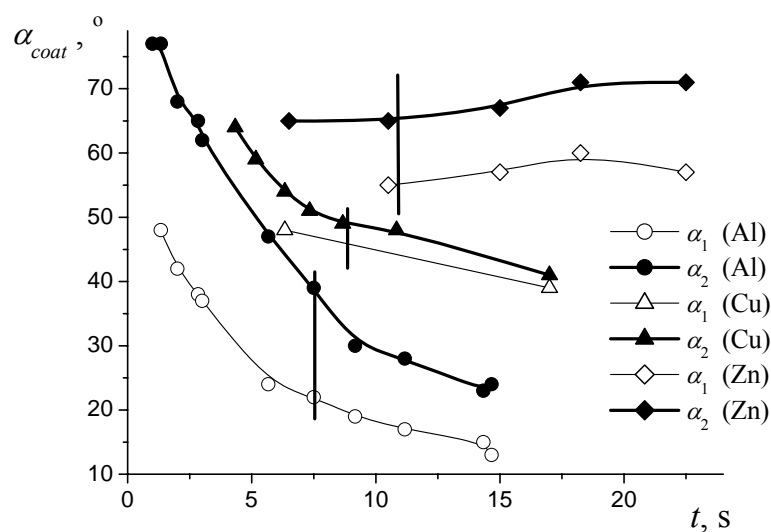
Fig. 5.3. Dynamics of growing coatings of different powders. The angles α_1 and α_2 of aluminium (Al), copper (Cu) and zinc (Zn) cones are shown as a function of time t. Vertical solid lines indicate those times when the area of the flat top of the corresponding coating cone decreases to zero.
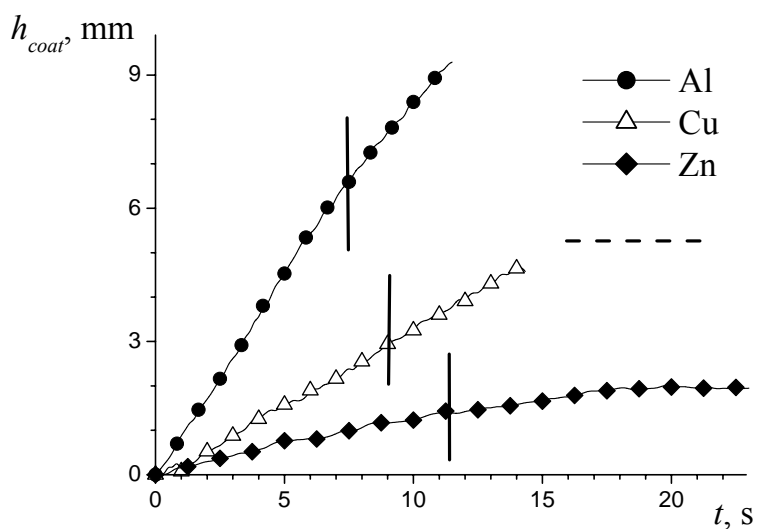

Fig. 5.4. Dynamics of growing coatings of different powders. The thickness h_{coat} of aluminium (Al), copper (Cu) and zinc (Zn) coatings are shown as a function of time t. The horizontal dashed line indicates the maximal thickness of the copper coating observed in the experiment. Vertical solid lines indicate those times when the area of the flat top of the corresponding coating cone decreases to zero.
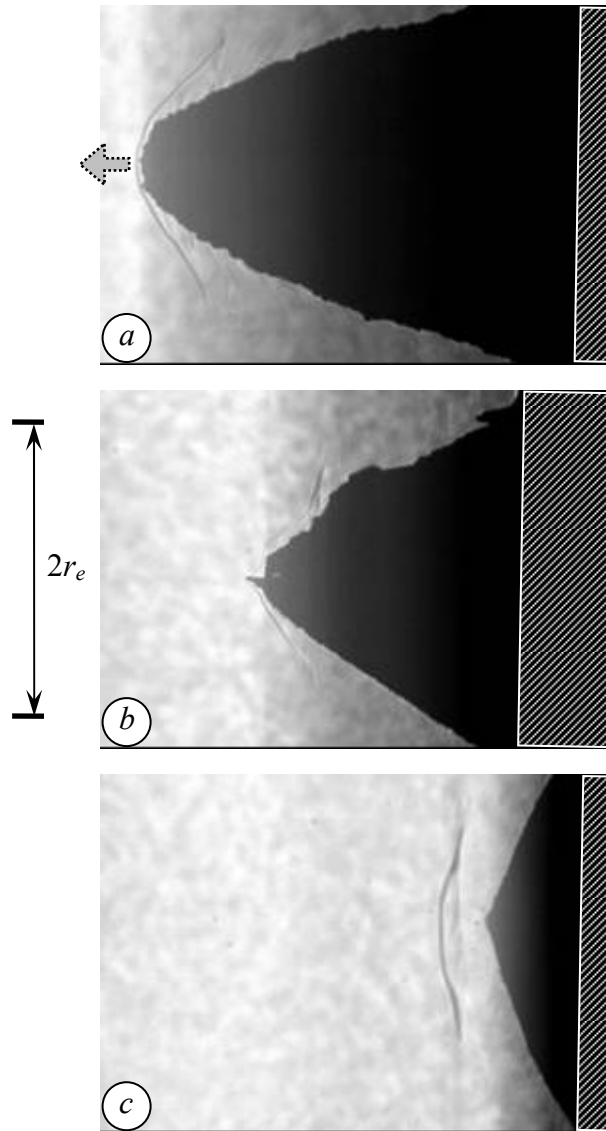
Fig. 5.5. Shapes of different coatings: aluminium (a), copper (b) and zinc (c) coatings on a steel substrate.

As can be seen in Fig. 5.3, the angles α_1 and α_2 decreases with time and, hence, with increasing height of the cone. An exception is the case where zinc powder was used. Here the angles remained practically constant during the time of measurement. This can be explained by the small height of the cone formed by zinc powder (cf. Fig. 5.4). For technical reasons measurements are not possible during the initial stage of the growth when the height of the cone is still very small. Thus measurements represent only times after the flat-top has disappeared and variations of the angles are small.

The mantle of the upper frustum is exposed to the flow in the jet core. The corresponding angle, which is obtained after the coating growth has come to a stop, α_2 characterizes qualitatively the ability of the powder to adhere to the surface after impact. As mentioned above the probability of particle adherence decreases with decreasing angle α_2. Hence, the ability of adherence is greater for powders which develop a smaller final angle α_2. Thus, according Fig. 5.3, the powders used can be arranged in the order of their bonding strength: aluminium, copper, zinc. The dynamics of the thickness of the coatings, shown in Fig. 5.4, also agrees with this order. Zinc powder shows the smallest growth rate as well as the smallest maximal height of the cone produced. In these considerations the volume flux of particles in the impinging jet has been assumed to be the same for all powders. Estimates based on experimental data show the same level of the volume flux for particles of copper and zinc and a slightly smaller one for particles of aluminium. Thus the arguments introduced above for arranging the ability of adherence of powders are still valid.

It is necessary to note the qualitative character of the data presented. In the experiments changing the powder leads to changing many other parameters, as for example, the particle and thus the impact velocity. As has been mentioned earlier powder particles of the same material and the same range of size but provided by different manufactures can show a different ability of forming a coating (cf. Fig. 5.1 and Fig. 5.5a that show aluminium coatings produced with nominally the same powders of different manufactures). Also, note that a comparison of coating shapes allows only to compare the adherence characteristics between particles rather than that between particles and a substrate. Thus, the dynamics of coating growth depends only on the powder but not on the substrate (provided that a first layer of a coating can be formed on the substrate).
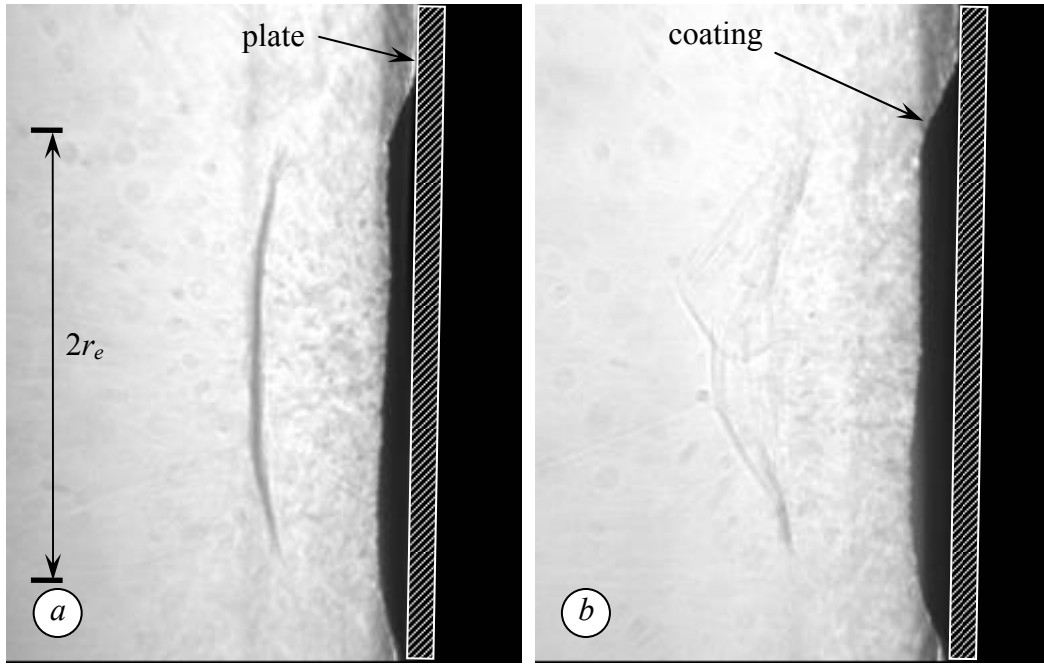
Fig. 5.6. Shadowgraph pictures of a growing coating in a steady (*a*) and unsteady (*b*) flow.

Finally, coating growths under steady and unsteady conditions of jet impingement have been compared. In experiments particles of aluminium having radiuses in the range of $r_p = 5\text{-}50$ μm have been sprayed onto an aluminium substrate. The impinging jet had standard parameters: a flow Mach number of $M = 2.8$ and a degree of off-design of $n = 0.8$. Steady and unsteady flow conditions have been obtained by adjusting the nozzle-to-plate distances to $x_{st} \approx 5r_e$ and $x_{unst} \approx 6r_e$, respectively. In Fig. 5.6 typical shadowgraphs are shown of a steady (*a*) and unsteady (*b*) shock layer ahead of the plate. Although the behavior of reflected particles differs clearly the geometry of the coatings does not change significantly. However, the experiments show a difference in the growth rates of the coatings under these two conditions. The following growth rates *k* have been observed at the beginning of the coating process, i.e., when the coating thickness ($h_{coat} < 1$ mm) is still small and its influence on the shock behavior is negligible: $k_{st} = 0.092 \pm 0.005$ mm/s and $k_{unst} = 0.071 \pm 0.005$ mm/s in the steady and unsteady case, respectively. As the coating thickness increases the growth rate *k* changes to a value of 0.070-0.075 mm/s in both cases. Note that in the both cases an increase of the coating thickness to values greater than 1.5-2 mm leads to a convex shape of the plate shock which initially was flat in the steady case. This convex shape of the shock is resulting not from the formation of a recirculation bubble in the shock layer (as in the unsteady case for thin coatings), but from the shape of the coatings which becomes conical. This can explain the equal growth rates of thick coatings for both steady and unsteady cases. The smaller growth rate under conditions of unsteady flows is still not understood.

5.2 Luminescence during particle impact

During experiments with impinging particle-laden jets light has been observed that was emitted from the region of particle impacts onto the substrate. The intensity of the light depends on many conditions, e. g., on the materials of the particle and the substrate, on the particle impact velocity and temperature. Here, first results of an investigation of the characteristics of the phenomenon of luminescence are presented and possible sources of radiation are discussed. Particles of aluminium, copper, zinc and iron having radiuses in the range of $r_p = 5$-50 μm were used in the experiments. The gas flow in the jet had the same standard parameters as described in chapter 3 and 4: a flow Mach number of M = 2.8 and a degree of off-design of $n = 0.8$.

Fig. 5.7 shows a typical picture of a light spot in the region of particle impacts. Fig. 5.7 also contains a sketch of the diagnostic method. All pictures presented in this chapter have been obtained by this method. The exposure time of each picture is $t_{exp} = 10$ ms. In order to protect optical elements and, in particular, the CCD-camera, a filter was used which allows a transmission of light only in the visible range, $\lambda = 0.4$-0.8 μm. The substrate has been moved past the jet with a velocity of $u_{sub} = 100$ mm/s. This corresponds to a shift of $0.3r_e$ within the exposure time of $t_{exp} = 10$ ms.
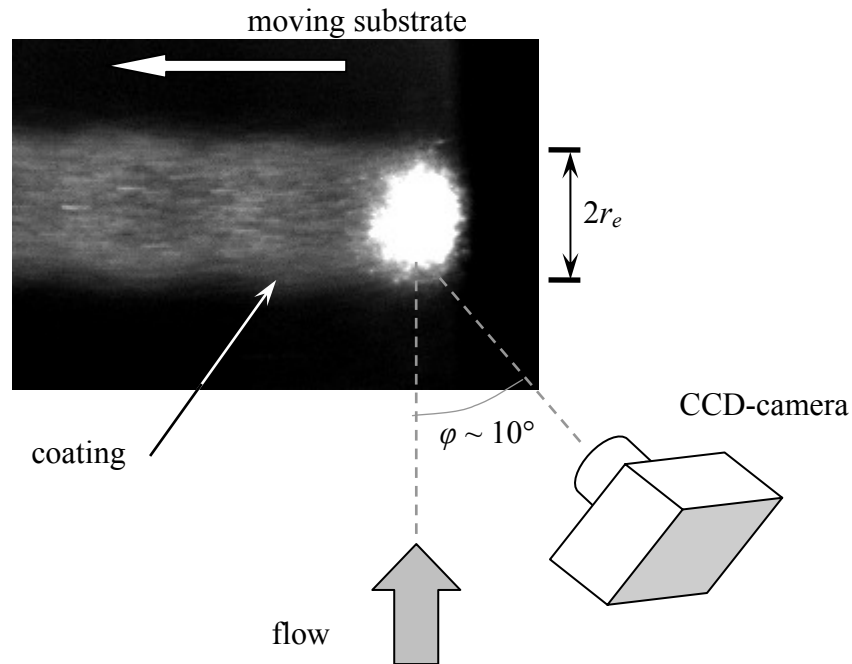

Fig. 5.7. Luminescence: light spot in the impact region of particles and sketch of diagnostics.
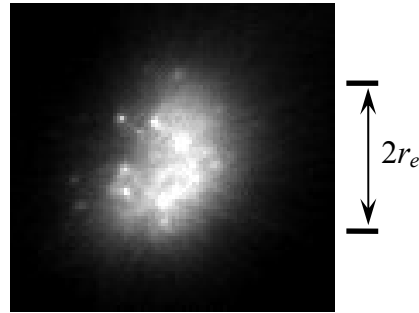
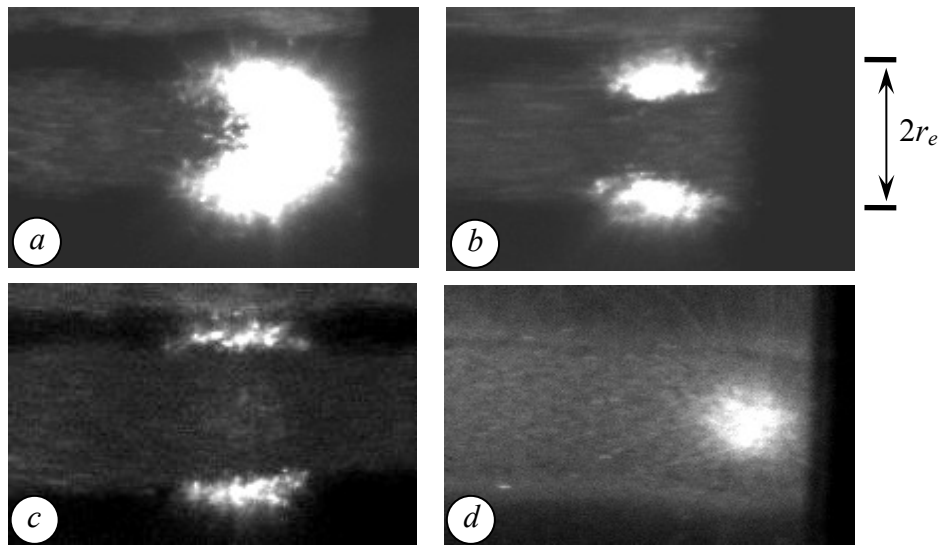Fig. 5.8. Typical light spot in the impact region of particles.

Fig. 5.9. The appearance of a light spot changes when the same strip of a substrate is repeatedly sprayed. Light spots as seen during first three passes of the jet over the strip (a, b, c) and during a pass over a completely coated strip (d) are shown. Note that in order to visualize the light the brightness of picture (d) has been essentially increased compared to the other pictures (cf. text).

In Fig. 5.8 a typical light spot is shown for the case of iron particles impinging on a steel substrate. In the photograph individual bright points can be distinguished in the region of the light spot. These flashes of luminescence can be traced to the impact of separate particles of iron. It is clear that the intensity of the luminescence depends on the parameters of impinging particles. Thus brighter points in the light spot can indicate the impact of individual particles having particular parameters such as a greater mass or greater impact velocity.

The intensity of the emitted light also depends on the conditions of the impacted surface. When several layers of a coating are applied to a single strip on a substrate by repeatedly moving the substrate through the jet, the intensity of the luminescence changes with the number of passes through the jet. In Fig. 5.9 typical distributions of the intensity of the light are shown. The photographs have been taken during the first, second and third passage of the strip through the jet (Fig. 5.9a-c), and in one case during a much late passage (Fig. 5.9d) where the strip was already fully covered by a coating.

Table 5.1. Light emission and formation of coatings at different conditions of particle-substrate impacts. Emission of light is marked by ○ (weak) and ☼ (bright). A formation of a coating is indicated by filled cells; in the case of empty cells a coating has not been formed. Crosshatched cells (Fe) indicate conditions that were not tested.

Powder	T_0, K			Substrate						
				Fe		Cu		Al		Zn	
Al			650		☼		☼		☼		☼
		500		☼		☼		☼		☼	
	300			○		○		○		○	
Fe			550		☼	▓	▓	▓	▓		░
	300			░		░		░		░	
Cu			500		○		○		☼		▓
	300			○				☼			
Zn			650		▓		▓		☼		▓
		500		▓		▓		☼		▓	
	300			▓		▓		○		▓	

As can be seen bright light is emitted from that regions where particles impact on the substrate surface rather than on a coating formed during a previous passages. Nevertheless, a weak radiation is also present in regions where particles impinge on a coating. The intensity of such light emissions is an order of magnitude smaller than in the case of particle-substrate impacts. In order to show the light spot more clearly the brightness of the picture has been increased in Fig. 5.9d. Luminescence like the one shown here has also been observed for different materials of powder and substrate (aluminium, copper, iron and zinc) and for different stagnation temperature of the jet ($T_0 = 300\text{-}650$ K). All powder-substrate combinations for which luminescence has been observed show a behavior similar to that presented in Fig. 5.9. Therefore, in the following the characteristics of the intensity of the light spot that occurs during the first passage of a clean substrate through the jet will be used for characterizing luminescence produced by different powder-substrate combinations. Qualitative information about light emission observed in different cases is summarized in Table 5.1. Data on whether a coating is formed or not is also included in the table.

As can be seen, the emission of the light does not correlate with the possibility of formating a coating. Zinc powder forms a coating on any substrate, but gives a bright light only when sprayed onto aluminium substrates. On the other hand aluminium and copper powder give light even at conditions (low temperature) where they do not form a coating. Most likely light emission is connected with the materials used, e. g., aluminium shows luminescence at all conditions, except for spraying iron powder on aluminium substrates while zinc and iron show only little luminescence.

Here it is necessary to describe two additional findings. The first one is that at conditions where a coating is not formed the intensity of the luminescence does not significantly change in time even after a long-term exposure. The second finding concerns the repeated application of a coating onto the same strip. During the process of spray deposition the newly formed coating suffers damage from particle impacts. Thus, during a repeated spraying of a strip on a substrate on which a coating has already been formed, some weak parts of the previously deposed coating can be removed.
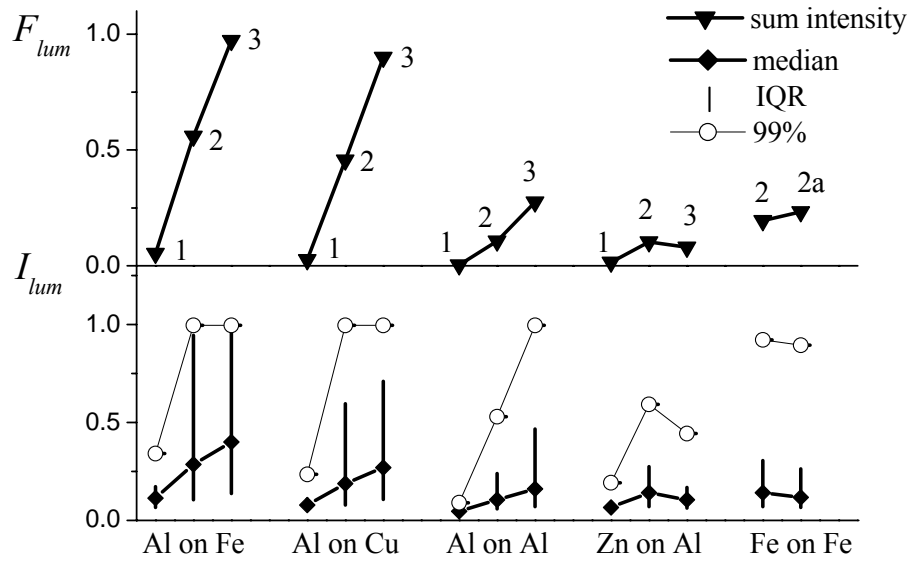
Fig. 5.10. Variation with stagnation temperature of the intensity of light for different impact conditions (e. g., "Al on Cu" means spraying of aluminium powder onto a copper substrate). F_{lum} is the total radiant flux of a light spot. A local intensity (I_{lum}) relating to light received by individual pixels is also shown (mean value, IQR - the inter quartile range (from 25th to 75th percentile) and the 99th percentile). Numbers indicate the stagnation temperature of the gas flow: 1) $T_0 = 300$ K, 2) $T_0 = 500$ K, 2a) $T_0 = 550$ K, 3) $T_0 = 650$ K.

Under such conditions a local flash of brighter luminescence is observed until this region of substrate becomes again coated. It is clear that a flashing appearance of luminescence occurs when particles impact on the substrate but not on the coating. Both of these findings show that the origin of luminescence is rather independent of oxidation (or any other impurities) layer on the surface of both particles and substrate.

Based on pictures of light spots as in Fig. 5.8 the intensity of the emitted light has been measured for different conditions of spraying. Results of the measurements are shown in Fig. 5.10. The local intensity of the smallest region of an image, i.e., of a pixel, is given by I_{lum}. In considering the intensity of a light spot it is useful to provide statistical values: the mean value, the inter quartile range (the IQR: from 25th to 75th percentiles) and the 99th percentile. The latter characterizes the maximum value. Also it is possible to calculate an integral value, F_{lum}, which is defined as the sum of the intensity of all pixels in a light spot. The parameters introduced are scaled by the sensibility of the CCD-matrix, so that a local intensity of $I_{lum} = 1.0$ corresponds to the maximal brightness of an image pixel. Note that, particularly at bright spots, the image pixel can become overexposed. In this case the integral value F_{lum} is more credible.

In Fig. 5.10 experimental data are grouped according to the combination of powder and substrate materials used. In all cases an increase of the stagnation temperature of the jet at otherwise equal conditions leads to an increase of the intensity of the light. Note that an increase of the stagnation temperature of the jet results in an increase of the temperature of particles before impact as well as in an increase of the impact velocity of particles.

106

It is possible to obtain an estimate of the mean power density of the luminescence, I_{exp}, observed in the experiments. When it is assumed that light is radiated isotropically into the half space bounded by the substrate the intensity of light can be evaluated as follows:

$$I_{exp} \approx E_{ccd.pix} \cdot \frac{2\pi L^2}{s_{obj}} \cdot \frac{1}{s_{im} t_{exp}}, \qquad (5.1)$$

where $E_{ccd.pix} \approx 1.9 \cdot 10^{-15}$ J is the maximal energy that can be registered by one cell (pixel) of the CCD-matrix, $s_{obj} \approx 3.1 \cdot 10^{-4}$ m^2 is the area of the camera objective, $L \approx 0.2$ m is the distance between the substrate and the camera, $s_{im} \approx 3.8 \cdot 10^{-8}$ m^2 is the area of the substrate region imaged by one pixel of the CCD-matrix, and $t_{exp} \approx 1 \cdot 10^{-2}$ s is the time of exposure of the CCD-matrix. In the experiments the direction of light observation was close to normal, hence the influence of the angular distribution is negligible. This estimate gives a value of $I_{exp} \approx 4 \cdot 10^{-3}$ W/m^2.

What can be the source of luminescence? Let us consider different possibilities. The first one is thermal radiation originating from the area of contact between particle and substrate. This contact area is heated by energy released during the impact. The second explanation of luminescence is based on the emission of charged particles (ions and electrons) by deformed surfaces. In this case a collision of electrons or ions with atoms and molecules of the ambient gas, i.e., a gas discharge, could result in a luminescence. The third possibility is the phenomenon of mechanoluminescence that is typically observed at the formation, motion, collision and dissipation of defects in solids. Here, such defects are produced during the impact of particles. These mechanisms are considered more deeply in the following.

Thermal radiation. The intensity of thermal radiation of a heated surface can be calculated. Here, luminescence has been observed in the visible range of wavelengths (from $\lambda_1 = 0.4 \cdot 10^{-6}$ to $\lambda_2 = 0.8 \cdot 10^{-6}$ m). The intensity of thermal radiation I_{therm} corresponding with this range can be presented as follows (equation of black-body radiation [Eckert & Drake 1972]):

$$I_{therm} \approx 2\pi\varepsilon_\lambda hc^2 \int_{\lambda_1}^{\lambda_2} \frac{1}{\lambda^5} \exp\left(-\frac{hc}{\lambda k T_{therm}}\right) d\lambda, \qquad (5.2)$$

where ε_λ is a spectral coefficient (emmisivity) of thermal radiation (for aluminium: $\varepsilon_\lambda \approx 0.1$), h is Planck's constant, k is Boltzmann's constant, c is the speed of light in vacuum and T_{therm} is the temperature of the surface. Using this expression it is possible to calculate a temperature of the contact area at which the $I_{therm} \approx I_{exp}$. For aluminium this gives $T_{therm} \approx 850$ K. The stagnation temperature of the gas flow was always smaller than T_{therm}. Therefore, heating up the impacted surface to a temperature as high as T_{therm} can only be due to the kinetic energy of particles that is set free on impact and result in heating part of both the particle and the substrate. Let us estimate the amount of kinetic energy which is released during the impact of a particle on a surface of area s_{im} within a given time of exposure t_{exp}. For flow parameters as given in Table 4.3 (aluminium powder) the mean quantity of particle impacts per s_{im} and t_{exp} is about $n_{p.im.exp} \approx 20$ and the kinetic energy of each particle is of the order 10^{-6} J. The energy Q_{therm} needed in order to increase the particle temperature, for example, from the initial (stagnation) temperature T_0 up to T_{therm} is given by:

$$Q_{therm} = m_p q (T_{therm} - T_0), \qquad (5.3)$$

where m_p is the mass of a particle and q is the specific heat of the material of the particle (aluminium). This estimate gives the order of $Q_{therm} \approx 5 \cdot 10^{-6}$ J. Considering furthermore

that not all of the kinetic energy will be transformed into heat (think of the kinetic energy of reflected particles), it is clear that the kinetic energy of the impinging particles does not suffice to raise the temperature of the whole particle up to T_{therm}.

However, the duration of a particle-substrate interaction is determined by the time of propagation of the compression wave which propagates much faster than the thermal wave. Alkhimov et al (2000*b*) assumed that within this short time only a small part of the materials is heated. The mass of material heated is then smaller than the mass of the whole particle this may cause a partial melting in a thin contact layer. However the calculated temperature of this layer is still lower than T_{therm}. Thus, thermal radiation can only contribute an insignificant part to the observed luminescence.

Gas discharge or gas excitation (Glow of the gas). Upon impact of a particle on a substrate materials are deformed and can fracture. A phenomenon light emission occurring upon fracture of a wide range of materials, the so-called *gas-discharge triboluminescence*, is described in the literature [Sage & Bourhill 2001]. Generally, it is accepted that the mechanism for gas-discharge triboluminescence is a crystalline fracture resulting in piezoelectric charging of the newly created surfaces. In this, the charge is sufficiently large to cause a gas discharge and/or gas excitation *via* electron bombardment. When the ambient gas is air the glow of the gas has a pronounced spectral characteristic equaling that of a nitrogen discharge [Zinc et al. 1976]. Known materials that exhibit gas-discharge triboluminescence upon fracture are non-metals. The efficiency of triboluminescence varies from the emitting of several photons up to "light which can be seen in daylight" [Sage & Bourhill 2001]. This range obviously covers the intensity of impact-induced light (I_{exp}) measured in our experiments (which can be characterized as "light which can be seen in a dark laboratory"). It appears that it has not yet been studied whether metals can show fracture-induced triboluminescence. On the other hand particles of metal are normally covered by a thin layer of oxide which can include also other impurities. Fracture of this layer could result in a gas discharge.

Another mechanism of gas glow is an anomalous emission of electrons which occurs from a deformed surface under certain conditions when a mechanical load is applied to metals [Kusov et al. 1990, Zakrevskii & Shul'diner 1999]. In this case the collision of electrons with molecules of the ambient gas can result in an excitation of the gas and in a glow. This phenomenon has also not well been studied. Furthermore, the phenomenon of emission of electrons from solids under mechanical loads can occur simultaneously with the emission of photons [Abramova et al. 1998]. Since the mechanism of direct emission of photons does not involve the ambient gas the latter mechanism of luminescence is considered separately in the following.

Mechanoluminescence. It is known that solids under mechanical loading emit photons. This phenomenon is called *mechanoluminescence*. The experiments indicate that mechanoluminescence is a quite universal property of solids. In our case luminescence of metals is of interest. It was established experimentally and theoretically [Abramova et al. 2001, 2002, Chandra et al. 1996] that mechanoluminescence of metals is caused by dislocations that are formed during thermal or mechanical strains. These dislocations interact, move and can reach the surface of deformed metal. The energy stored in the dislocations is released when the boundary conditions change. This happens when a dislocation reaches a surface. Thus, the intensity of mechanoluminescence of metals depends on the number of dislocations in the near-surface region and on their mobility.

In works of [Abramova et al. 1999*a*, 1999*b*, Banishev et al. 2003] the dynamics of the emission process has been studied for the example of mechanoluminescence caused by thermal strains of metals such as copper, silver, gold and tungsten. In

108

experiments mechanoluminescence is excited on the backside of metal samples whose front side is irradiated by single laser pulses. The energy of the laser pulse has been lower than that causing the onset of metal spallation. The fast nondestructive loading initiates mechanical and thermal stresses. The stresses propagate through the metal from the front side to the back side of the metal sample. When dislocations formed by the stress wave reach the rear surface this results in the emission of photons. Typical intensities of mechanoluminescence I_{ML} were found to be in the range of $I_{ML} \approx 10^{-4}$-10^{-3} W/m^2 in visible range of wavelengths. This is of the same order of magnitude as the intensity I_{exp} of the impact-induced luminescence observed in the present work.

In conclusion, all three mechanisms can contribute to impact-induced luminescence that has been observed in the present work. However, the characteristics of impact-induced luminescence allow to assume that mechanoluminescent is the major source of light. As has been shown above thermal radiation is negligible since insufficient heat is produced during particle impacts on the substrate. Gas-discharge glow has so far not been observed for metals. The strong dependence of the intensity of the light on both, materials and particle velocity supports the conclusion that impact-induced luminescence is caused by mechanoluminescence.

Certainly, further theoretical and experimental investigations of luminescence observed during high-velocity particle impacts will help to distinguish the contribution of each mechanism described above. In addition to changing the conditions of the experiment (gas temperature, particle velocity, different materials of particles and substrates) the irradiated light needs to be studied by spectroscopy. This is beyond the scope of the present investigation.

6. Conclusions

A newly developed multi-exposure shadowgraphy and high-frequency surface-pressure measurements have been used for studying the unsteady gas flow and particle behavior in a supersonic jet impinging onto a plate. This method enables one to obtain information on the gas flow and the particle motion at the same time. In this manner it becomes more easy to obtain a physical understanding of processes occurring in the flow. The wide flexibility of the multi-exposure shadowgraphy allows for determining not only parameters of an object (e.g., velocity) but also the rate of change (e.g., acceleration) at different times. Furthermore it is possible to obtain additional information on objects as, for example, the shape and size of particles or the shape of shock waves.

The study covers a wide variety of problems occurring when supersonic two-phase jets impinge onto plates: mean flow parameters and the unsteady behavior of the gas in the impingement zone, particle dynamics in the shock layer ahead of a plate and particle-plate interactions. In the following the main results of this study will be summarized.

In order to obtain a proper understanding of processes occurring during the impingement of jets a knowledge of the properties of the impinging free jet is required. Especially, shock structures in the free jet are of interest since they interact significantly with the flow field formed ahead of the plate. For this purpose over- and underexpanded supersonic jets formed by an extremely slender axisymmetric nozzle (as it is applied in the Cold Spray deposition technology) have been investigated. The particular feature of such nozzles is the presence of a thick boundary layer at the nozzle exit. The influence of the boundary layer on properties of jets issuing from the nozzle has been studied.

The main subject of the work is the unsteady flow field in the impingement region, the complexity of which poses many problems for researchers. Many features of the flow dynamics, in particular, when a recirculation bubble is present, have been explored here for the first time. A synchronized measurement of the shock motion (by multi-exposure shadowgraphy) and of the high-frequency pressure fluctuations on the plate was performed. It has been found that there exists a strong anti-phase correlation between the motion of the plate-shock and the variation of the pressure on the plate surface. In addition, the response of the pressure on the shock motion is delayed. This conforms the supreme role of shock structures in the formation of a recirculating flow in the shock layer ahead of the plate. Such a role had been assumed theoretically before.

The influence of a recirculating flow on the dynamics of the shock layer has been examined in detail by spectrometry. For the first time it has been shown that there are at least three types of flow oscillations which can be excited due to the impingement of supersonic jets onto plates. The first type is due to instability waves propagating through the shear layer formed at the jet boundary and, hence, it is independent of the flow field ahead of the plate. This type of oscillation is always present in combination with several harmonics. Its parameters depend crucially on the nozzle-to-plate distance. The second type of oscillations is connected with a spreading of flow instabilities through the jet core and the shock layer. These oscillations are characterized by a strong dependence on parameters of the shock layer. The third type of flow instabilities appears only under certain conditions. It involves an unsteady trigger-like behavior of the recirculating flow occurring in the shock layer. Such pulsations have a non-periodic character that results in low-frequency bursts in the pressure spectrums. Whereas the first two types of flow oscillations are resonance-like and exist at the same time, the

110

third one leads to an elimination of all resonance peaks. It should be noted that in most previous publications the presence of only one type of flow oscillations has been assumed. The simultaneous existence of different types of oscillations, which has been found in the present work, explains some variances in theoretical and experimental data published earlier.

An investigation of the dynamics of particles in the transonic flow field was carried out by high-performance multi-exposure shadowgraphy. Well recognizable traces of particles and unsteady shock waves have been obtained. From the pictures distributions of the particle velocity and concentration were obtained, both, in the free jet as well as in the shock layer. It has been shown that a cloud of reflected particles is formed in the shock layer ahead of the plate. Based on these results an upper bound of the coefficient of restitution has been estimated. Particle dynamics were studied in steady and unsteady shock layers. A strong influence of the state of the gas flow on the particle motion in the shock layer was noted. It has been found that normally reflected particles remain within the shock layer. However, under conditions relating to the third type of flow oscillations reflected particles are also present upstream of the plate shock during a certain part of the oscillation period.

The final part of the work concerns the interaction between particles and a plate. Growth rate and shape of coatings have been examined for impacts occurring under different conditions. It has been shown that flat-top coatings are produced but not Gauss-like shaped coatings as is normally mentioned in the literature. This difference in the coating shape has been explained by a uniform distribution of particle parameters across the jet in the present experiments. It has also been shown that rates of coating growth are different for the conditions of steady and highly unsteady flows, respectively.

The other topic relating to particle-plate interactions is the occurrence of luminescence that has been observed under conditions of high-velocity impacts of metal particles on metal substrates. The character of luminescence has been examined for a wide range of conditions, e.g., for different stagnation temperatures of the gas flow and different combinations of materials of powder particles and plates. Based on the experimental results, an analysis of three potential mechanisms of light emission has shown that impact-induced luminescence is mainly caused by mechanoluminescence.

The new diagnostic method developed here is such that it easily lends itself to incorporation into other scientific and engineering applications. In particular, a further development of the measurement techniques presented enables one to design on-line diagnostics of spray deposition processes as, for example, the Cold Spray technology. All parameters can be examined in real-time: the parameters of particle-laden jets (high-speed multi-exposure shadowgraphy) as well as the quality of coatings produced (observation of impact-induced luminescence). The character of luminescence which is a measure of the rate of bonding, should be studied more intensively by spectrometry. Other aspects of future work are connected with studying the origin and propagation of flow instabilities more deeply. This can be achieved by synchronizing flow visualization with simultaneous pressure measurements at multiple positions (instead of one) both, in the flow and on the plate surface. Thus results of the present work are useful both, for a further development of engineering applications and for a better understanding of the phenomena connected with particle dynamics and instabilities in transonic flows.

Appendix

Software developed for performing the experiments and processing the data

Introduction. More than 25000 pictures and files with numerical data have been collected during the experiments. A series including about one hundred shadowgraph pictures with satellite information was produced for every condition of the experiment. In order to increase the accuracy of the data all measurements have been performed with the highest spatial and time resolution possible. That also leads to strong enlargement of information content. Electronics and software have been built and developed for collecting and processing such great amount of data.

The software can be divided into two classes: software for controlling devices and acquisition of data during experiments, and software for processing the data obtained. The last class includes programs which work separately with either graphical or numerical data, and also programs which execute statistical analysis. Except for drivers for the CCD-camera and the signal generator which have been received from the manufacturers, all of the software has been newly developed in the programming language Visual C++ under a Windows NT operating system. Some samples of application of the software are provided below.

Motors Manager. The largest program for device control is *Motors Manager* with plug-in modules. This software allows to automate completely all figured motions of the object holder and to synchronize that with other measurements. For example, all axial and radial pressure profiles and all coatings on substrates have been performed with this application. In Fig. 2.14 a window of the *Motors Manager* is shown with sample of substrate motion. The program operates motors (changes direction and velocity of linear motion and rotation) and sends synch-signals to other applications (e.g., CCD-camera controls and pressure-measurement devices). The modular design of the code enables to add easily new complimentary modules of the control of devices and measurements. In plug-in windows processes of measurements can be observed and adjusted. Also a CCD-camera installed in the test chamber gives a "live" image in a special window of this program. The *Motors Manager* has a graphical-command user interface which allows easy to program the consequence of actions in the experiment. By this interface the user can also adjust parameters of the facility, e.g., geometry, parameters of electrical signals, step motors, PC-hardware and OS (operation system). The configurations and programs of experiments can be saved in files in PC and be reloaded again. A sample of figured coating produces by *Cold Spray* facility is shown in Fig. 2.15. Examples of profiles of pressure in a free jet and on a plate have been presented in chapter 3.
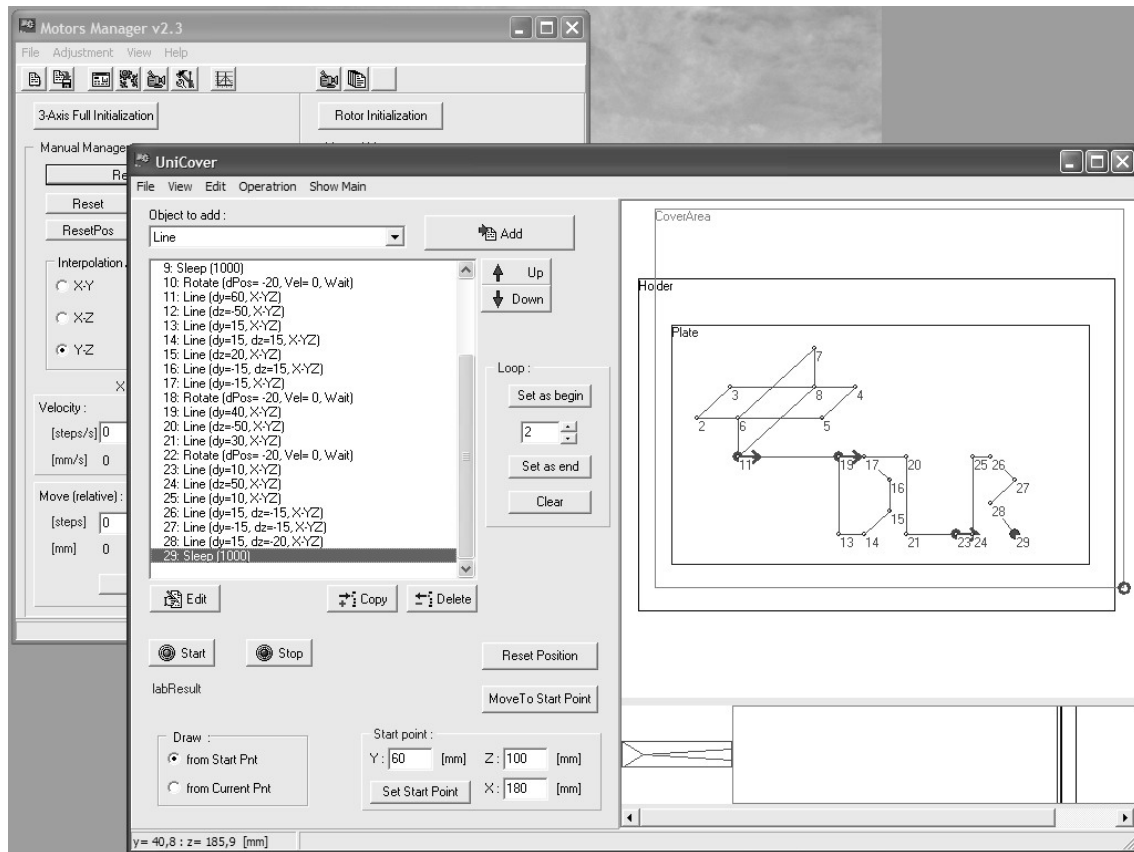
Fig. 2.14. Main window of the *Motors Manager* program: *Universal Programmer of Holder Motion*.
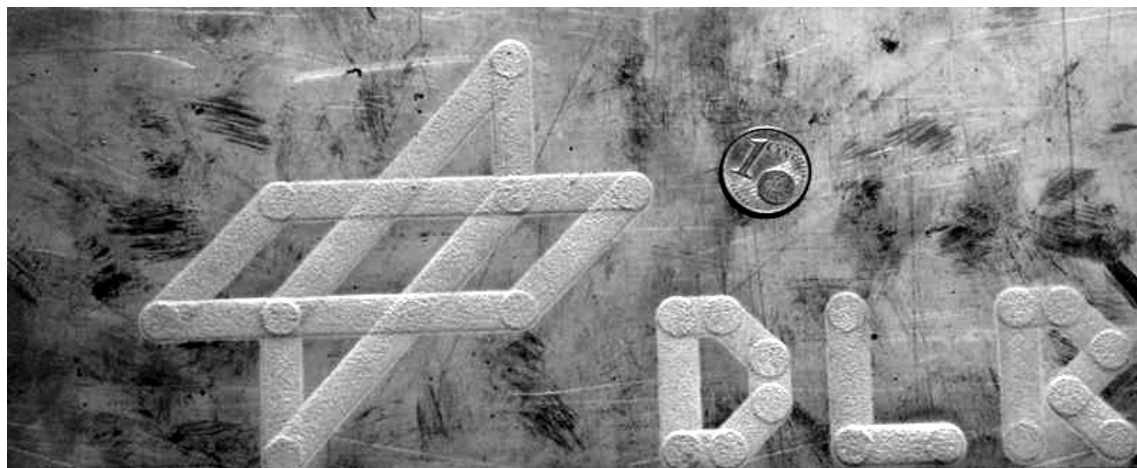

Fig. 2.15. Sample of figured coating produced by *Cold Spray* facility.

Spectrum Analyzer. A software package has been written for processing numerical data both, visually and statistically. Experimental data form several data-bases in which information is logically linked with each other. Programs execute mathematical operations, such as statistics, correlations and sorting, and also give a graphical expression of obtained data. Simultaneous visualization of data of different experiments and quick mathematical processing help a lot to analyze experimental and theoretical results. In Fig. 2.16 a sample of one packaged program is shown: *Spectrum Processor*. This application allows to show profiles of mean pressure and spectrums of pressure oscillations at the same time. Also general spectrum information about pressure oscillations is represented by the gray-scale image. During analyses particular points of profiles or spectrums are marked and are subject to mathematical processing, which is different for different tasks. Results of analyses are formed in report.
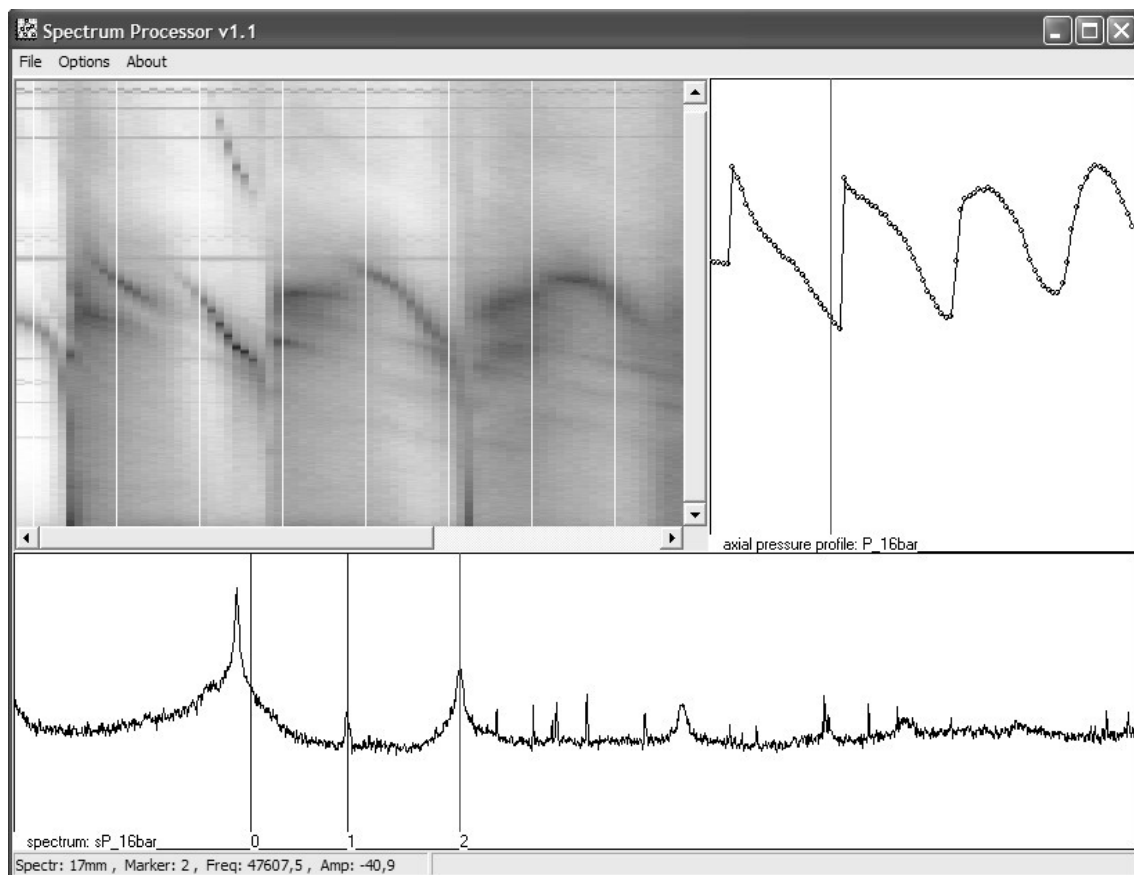
Fig. 2.16. One of windows of the *Spectrum Analyzer* program.

Image Marker. Shadowgraph pictures have been processed in the same way. For this purpose a graphical software package *Image Marker* has been written. This software helps to work with series of pictures: cutting, scaling, shifting and rotating - relative to selected object in pictures. Also pictures can be superposed by several methods for comparison. But the main task of this software package is collecting information about selected objects in the single picture as well as in series of pictures. For example, motions of the shock wave or particles in the impingement zone of a two-phase flow have been analyzed in this way. Sample of one program from this package is shown in Fig. 2.17: *Particle Track Marker*. This plug-in allows to mark wanted objects, such as particle images, and perform a report with required mathematical preprocessing. Particle velocities and distribution described in chapter 4 have been obtained in this program.
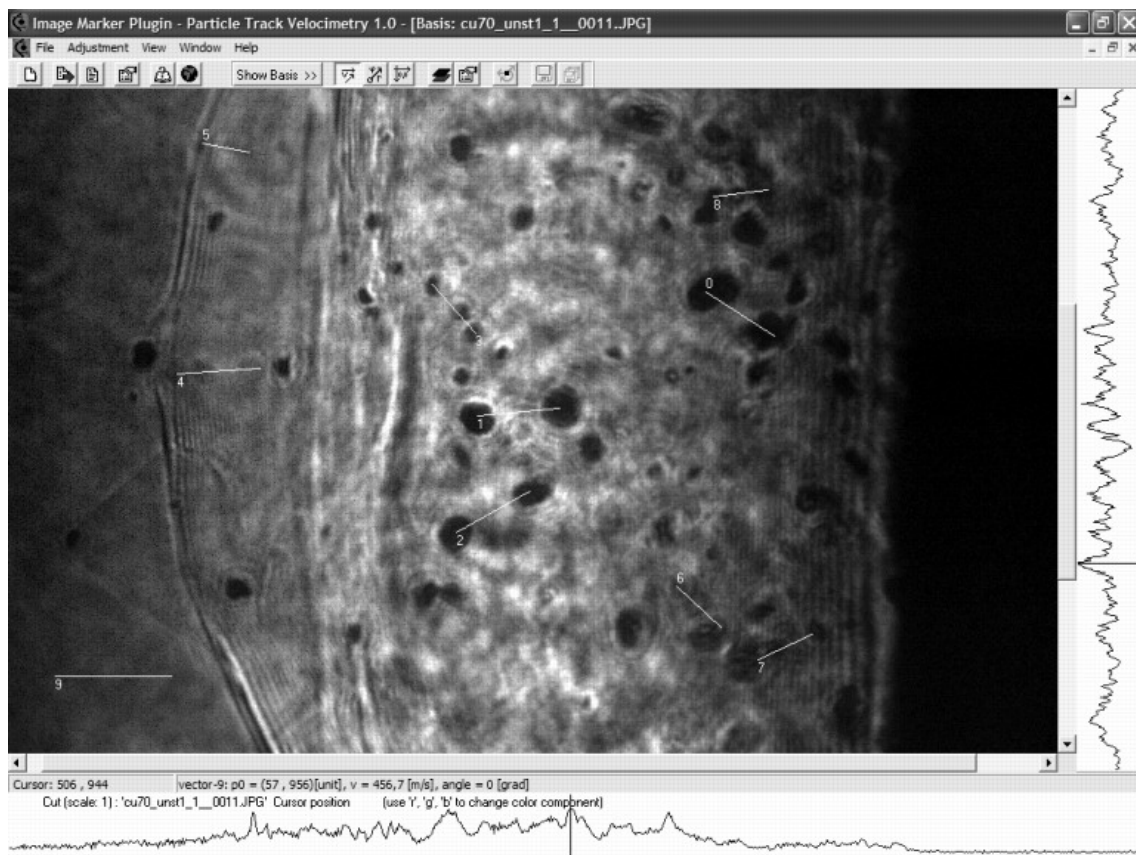
Fig. 2.17. One of windows of the *Image Marker* software package: *Particle Track Marker*.

References

Abramova, K. B., Rusakov, A. I., Semenov, A. A. & Shcherbakov, I. P. Luminescence of metals excited by fast nondestructive loading. *Physics of Solid State* **1998**, *40(6)*: 877-885.

Abramova, K. B., Semenov, A. A. & Shcherbakov, I. P. Dynamics of photon emission due to strains in metals. *Technical Physics* **2001**, *46(11)*: 1396-1400.

Abramova, K. B., Shcherbakov, I. P., Rusakov, A. I. & Semenov, A. A. Emission precesses accompanying deformation and fracture of metals. *Physics of Solid State* **1999a**, *41(5)*: 761-763.

Abramova, K. B., Vettegren', V. I., Shcherbakov, I. P., Rakhimov, S. Sh. & Svetlov, V. N. Mechanoluminescence and submicrorelief of a copper surface. *Technical Physics* **1999b**, *44(12)*: 1491-1493.

Abramova, K. B., Vettegren', V. I., Shcherbakov, I. P. & Svetlov, V. N. The emission of photons and the dynamics of submicrodefects on the surface of noble metals. *Technical Physics* **2002**, *47(2)*: 268-272.

Abramovich, G. N. *The Theory of Turbulent Jets.* Cambridge, **1963**.

Adrianov, A. L., Staryh, A. L. & Uskov, V. N. *Interferenzija Stazionarnyh Gasodinamicheskih Razryvov. (in Russian).* Nauka, Novosibirsk, **1995**.

Alkhimov, A. P., Klinkov, S. V. & Kosarev, V. F. Experimental study of deformation and attachment of microparticles to an obstacle upon high-rate impact. *Journal of Applied Mechanics and Technical Physics* **2000a**, *41(2)*: 245-250.

Alkhimov, A. P., Klinkov, S. V. & Kosarev, V. F. Temperature in contact zone under high-speed particle impact. *Physical Mesomechanics* **2000b**, *3(1)*: 53-57.

Alkhimov, A. P., Klinkov, S. V. & Kosarev, V. F. The features of Cold Spray nozzle design. *Journal of Thermal Spray Technology* **2001**, *10(2)*: 375-381.

Alkhimov, A. P., Klinkov, S. V., Kosarev, V. F. & Papyrin, A. N. Gas-dynamic spraying. Study of a plane supersonic two-phase jet. *Journal of Applied Mechanics and Technical Physics* **1997**, *38(2)*: 324-330.

Alkhimov, A. P., Kosarev, V. F. & Papyrin, A. N. A method of cold gas-dynamic deposition. *Sov. Phys. Dokl.* **1990**, *35(12)*: 1047-1049.

Alkhimov, A. P., Nesterovich, N. I. & Papyrin, A. N. Experimental investigation of supersonic two-phase flow over body. *Journal of Applied Mechanics and Technical Physics* **1982**, *2*: 66-74.

Alvi, F. S., Ladd, J. A. & Bower, W. W. Experimental and computational investigation of supersonic impinging jets. *American Institute of Aeronautics and Astronautics Journal* **2002** , *40(4)*: 599-609.

Antonov, A. N. & Gretsov, V. K. Experimental investigation of the characteristics of unsteady-state breakaway zones arising in a supersonic flow at a needle with a screen. *Fluid Dynamics* **1977**, *12(2)*: 567-572.

Antonov, A. N., Gretsov, V. K. & Shalaev, S. P. Nonsteady supersonic flow over spiked bodies. *Fluid Dynamics* **1976**, *11(2)*: 746-751.

Assadi, H., Gaertner, F., Stoltenhoff, T. & Kreye, H. Bonding mechanism in cold gas spraying. *Acta Materialia* **2003**, *51*: 4379-4394.

Banishev, A. F., Panchenko, V. Ya. & Shishkov, A. V. Nonthermal glow of thin metal plates and films exposed to pulsed laser radiation. *Technical Physics* **2003**, *48(5)*: 612-616.

Ben-Dor, G. *Shock Wave Reflection Phenomena.* Springer, Berlin, **1991**.

Boiko, V. M., Klinkov, K. V. & Poplavskii, S. V. Transonic transition behind shock wave traveling through a dust-gas mixture. *Fluid Dynamics* **2000**, *35(4)* : 605-611.

Boiko, V. M., Klinkov, K. V. & Poplavskii, S. V. Collective bow shock ahead of a transverse system of spheres in a supersonic flow behind a moving shock wave. *Fluid Dynamics* **2004** , *39(2)*: 330-338.

Carling, J. C. & Hunt, B. L. The near wall jet of a normally impinging, uniform, axisymmetric, supersonic jet. *Journal of Fluid Mechanics* **1974**, *66(1)*: 159-176.

Ceylan, K., Altunbass, A. & Kelbaliyev, G. A new model for estimation of drag force in the flow of Newtonian fluids around rigid or deformable particles. *Powder Technology* **2001**, *119*: 250-256.

Chandra, B. P., Khlan, M. S., Singh, S. R. & Ansari, M. H. -. *Cryst. Res. Technol.* **1996**, *4(31)*: 495.

Dillmann, A. Linear potential theory of steady internal supersonic flow with quasi-cylindrical geometry. Part 1. Flow in ducts. *Journal of Fluid Mechanics* **1994**, *281*: 159-191.

Dillmann, A. Linear potential theory of steady internal supersonic flow with quasi-cylindrical geometry. Part 2. Free jet flow. *Journal of Fluid Mechanics* **1995**, *286*: 327-357.

Donaldson, C. D. & Snedeker, R. S. A study of free jet impingement. Part 1. Mean properties of free and iminging jets. *Journal of Fluid Mechanics* **1971**, *45(2)*: 281-319.

Dunbar, L. E., Courtney, J. F. & McMillen, L. D. Heating augmentation in erosive hypersonic enviroments. *American Institute of Aeronautics and Astronautics Journal* **1975**, *13(7)*: 908-912.

Dykhuizen, R. C. & Smith, M. F. Gas dynamic principles of cold spray. *Journal of Thermal Spray Technology* **1998**, *7(2)*: 205-212.

Dykhuizen, R. C., Smith, M. F., Gilmore, D. L., Neiser, R. A., Jiang, X. & Sampath, S. Impact of high velocity Cold Spray particles. *Journal of Thermal Spray Technology* **1999**, *8(4)*: 559-564.

Eckert, E. R. G. & Drake, R. M. *Analysis of Heat and Mass Transfer.* Springer, Heidelberg, **1972**.

Elavarasan, R., Krothapalli, A., Venkatakrishnan, L. & Lourenco, L. Suppression of self-sustained oscillations in a supersonic impinging jet. *American Institute of Aeronautics and Astronautics Journal* **2001**, *39(12)*: 2366-2373.

Elavarasan, R., Venkatakrishnan, L., Krothapalli, A. & Lourenco, L. A PIV study of a supersonic impinging jet. *Journal of Visualization* **2000**, *2*: 213-221.

Gilmore, D. L., Dykhuizen, R. C., Neiser, R. A., Roemer, T. J. & Smith, M. F. Particle velocity and deposition efficiency in the cold spray process. *Journal of Thermal Spray Technology* **1999**, *8(4)*: 576-582.

Ginzburg, I. P., Semiletenko, B. G., Terpigor'ev, V. S. & Uskov, V. N. Some singularities of supersonic underexpanded jet interaction with a plane obstacle. *Journal of Engineering and Physics* **1973**, *19*: 1081-1084.

Gubanova, O. I., Lunev, V. V. & Plastinina, L. N. The central breakaway zone with interaction between a supersonic underexpanded jet and a barrier. *Fluid Dynamics* **1973**, *6*: 298-301.

Henderson, B. The connection between sound production and jet structure of the supersonic impinging jet. *Journal of Acoustical Society of America* **2002**, *111(2)*: 735-747.

Henderson, C. B. Drag coefficient of spheres in continuum and rarefied flows. *American Institute of Aeronautics and Astronautics Journal* **1976**, *14*: 707-708.

Henderson, L. F. Experiments on the impingement of a supersonic jet on a flat plate. *Z. Angew. Math. Phys.* **1966**, *17*: 553-569.

Henderson, L. F., Vasilev, E. I., Ben-Dor, G. & Elperin, T. The wall-jetting effect in Mach reflection: theoretical consideration and numerical investigation. *Journal of Fluid Mechanics* **2003**, *479*: 259-286.

Henderson, L. R. F. & Menikoff, R. Triple-shock entropy theorem and its consequences. *Journal of Fluid Mechanics* **1998**, *366*: 179-210.

Hornung, H. Regular and Mach reflection of shock waves. *Annual Reviews of Fluid Mechanics* **1986**, *18*: 33-58.

Kalghatgi, G. T. & Hunt, B. L. The occurrence of stagnation bubbles in supersonic jet impingement flows. *Aeronautical Quarterly* **1976**, *27*: 169-186.

Klinkov, K. V. & Rein, M. Multi-exposure visualization of supersonic two-phase flows impinging on a plate. *Proc. ICMAR XII in Novosibirsk* **2004**, *2*: 101-106.

Klinkov, S. V., Kosarev, V. F., Erdi-Betchi, A., Klinkov, K. V. & Rein, M. Determination of profile of velocity and concentration of particles in jet at exhaustion from conical nozzle under conditions of cold spray. *Proc. ICMAR XII in Novosibirsk* **2004**, *1*: 131-136.

Krothapalli, A., Rajkuperan, E., Alvi, F. S. & Lourenco, L. Flow field and noise charateristics of a supersonic impinging jet. *Journal of Fluid Mechanics* **1999**, *392*: 155-181.

Kusov, A. A., Klinger, M. I. & Zakrevskii, V. A. *Physics of Solid State* **1990**, *32*: 1694.

Landau, L. D. & Lifshitz, E. M. *Fluid Mechanics. Volume 6.* Butterworth-Heinemann, **1987**.

Meyer, E. & Guicking, D. *Schwingungslehre. (in German).* Friedr. Vieweg + Sohn, Braunschweig, **1974**.

Omel'chenko, A. V., Uskov, V. N. & Chernyshev, M. V. An approximate analytical model of flow in the first barrel of an overexpanded jet. *Technical Physics Letters* **2003**, *29(3)*: 243-245.

Oswatitsch, K. *Grundlagen Der Gasdynamik.* Springer, Wien, **1976**.

Pack, D. C. On the formation of shock-waves in supersonic gas jets. *The Quarterly Journal of Mechanics and Applied Mathematics* **1948**, *1(1)*: 1-17.

Panda, J. Shock oscillation in underexpanded screeching jets. *Journal of Fluid Mechanics* **1998**, *363*: 173-198.

Papyrin, A. N., Klinkov, S. V. & Kosarev, V. F. Modeling of particle-substrate adhesive interaction under the Cold Spray process. *Thermal Spray: Advancing the Science & Applting Technology* **2003**.

Raffel, M., Willert, C. & Kompenhaus, J. *Particle Image Velocimetry.* Springer, Berlin, **1998**.

Rein, M., Erdi-Betchi, A. & Klinkov, K. V. Transonic flow phenomena of the cold spray deposition process. *Fluid Mechanics and Its Applications* **2003**, *73*: 177-182.

Rein, M., Grabity, G. & Meier, G. E. A. Non-linear wave propogation in transonic nozzle flow. *Journal of Sound and Vibration* **1988**, *122(2)*: 331-346.

Rist, D. *Dynamik Realer Gase.* Springer, Berlin, **1996**.

Romine, G. L. Nozzle flow separation. *American Institute of Aeronautics and Astronautics Journal* **1998**, *36(9)*: 1618-1625.

Sage, I. & Bourhill, G. Triboluminescent materials for structural damage monitoring. *Journal of Matherials of Chemistry* **2001**, *11*: 231-245.

Schlichting, H. *Boundary-Layer Theory.* McGraw-Hill, **1978**.

Settles, G. S. *Schlieren and Shadowgraph Techniques: Visualizing Phenomena in Transparant Media.* Springer, Berlin, **2001**.

Sommerfeld, M. Experimental and numerical studies on particle laden underexpanded free jet. *Gas-Solid Flows* **1991**, *121*: 213-220.

Sommerfeld, M. The structure of particle-laden, underexpanded free jets. *Shock Waves* **1994**, *3*: 299-311.

Sommerfeld, M. & Decker, S. On the importance of the Basset-hisoty term on the particle motion induced by a plane shock wave. *Proc. ISSW in Marseille* **1995**, 37-42.

Soo, S. L. *Fluid Dynamics of Multiphase Systems.* Blaisdell, **1967**.

Tam, Ch. K. W. On the noise of a nearly ideally expanded supersonic jet. *Journal of Fluid Mechanics* **1972**, *51*: 69-95.

Tam, Ch. K. W. & Ahuja, K. K. Theoretical model of discrete tone generation by impinging jets. *Journal of Fluid Mechanics* **1990**, *214*: 67-87.

Tam, Ch. K. W. & Burton, D. E. Sound generated by instability waves of supersonic flows. Part 2. Axisymmetric jets. *Journal of Fluid Mechanics* **1984**, *138* : 273-295.

Tam, Ch. K. W. & Hu, F. Q. On the three families of instabilitiy waves of high-speed jets. *Journal of Fluid Mechanics* **1989**, *201*: 447-483.

Thomas, P. J., Buetefisch, K.-A. & Sauerland, K. H. On the motion of particles in a fluid under the influence of a large velocity gradient. *Experiments in Fluids* **1993**, *14*: 42-48.

Tran-Cong, S., Gay, M. & Michaelides, E. E. Drag coefficients of irregularly shaped particles. *Powder Technology* **2003**, *in press(in press)*: in press.

Umeda, Y. & Ishii, R. Hole tone generation from highly choked jets. *Journal of Acoustical Society of America* **1993**, *94(1)*: 1058-1066.

Van Steenkiste, T. H., Smith, J. R. & Teets, R. E. Aluminium coatings via kinetic spray with relatively large powder particles. *Surface and Coatings Technology* **2002**, *154*: 237-252.

Varnier, J. & Raguenet, W. Experimental characterization of the sound power radiated by impinging supersonic jets. *American Institute of Aeronautics and Astronautics Journal* **2002** , *40(5)*: 825-831.

Vasilev, E. I., Ben-Dor, G., Elperin, T. & Henderson, L. F. The wall-jetting effect in Mach reflection: Navier-Stokes simulations. *Journal of Fluid Mechanics* **2004**, *511*: 363-379.

Weinbaum, S. Rapid expansion of a supersonic boundary layer and its application to the near wake. *American Institute of Aeronautics and Astronautics Journal* **1966**, *4(2)*: 217-226.

Willert, C., Raffel, M., Kompenhans, J., Stasicki, B. & Kaehler, C. Recent applications of particle image velocimetry in aerodynamic research. *Flow Measurement Instruments* **1996**, *7(3/4)*: 247-256.

Zakrevskii, V. A. & Shul'diner, A. V. Eletronic excitations owing to plastic deformation of ionic crystals. *Physics of Solid State* **1999**, *41(5)*: 817-819.

Zapryagaev, V. I. & Mironov, S. G. Experimental study of pulsations in the forward separation zone. *Journal of Applied Mechanics and Technical Physics* **1987**, 620-627.

Zapryagaev, V. I. & Mironov, S. G. Features of separated supersonic flow pulsations ahead of the spike-tipped cylinder. *Journal of Applied Mechanics and Technical Physics* **1990**, 913-919.

Zink, J. I., Hardy, G. E. & Sutton, J. E. -. *Journal of Physical Chemistry* **1976**, *80*: 248.

Acknowledgements

Lebenslauf

Name:		Konstantin Vladimirovich Klinkov
Geburtsdatum:		04.06.1977
Geburtsort:		Chulym, Russland
Familienstand:		verheiratet
Staatsangehörigkeit:		russisch

Schulbildung:	Sep 1984 – Jun 1993	Schule N11 in Anjero-Sudjensk, Russland
	Sep 1993 – Jun 1994	Schule N165 in Novosibirsk, Russland
Studium:	Sep 1994 – Jul 2000	Staats-Universität in Novosibirsk, Russland, Fakultät der Physik,
	1998 – 2000	Diplomarbeit am Institut für Theoretische und Angewandte Mechanik (Russische Akademie der Wissenschaften), Novosibirsk, Russland
	Jun 2000	Master Grad der Physik, Staats-Universität in Novosibirsk, Russland
	2000 – 2001	Wiss. Ang. am Institut für Theoretische und Angewandte Mechanik (Russische Akademie der Wissenschaften), Novosibirsk, Russland
Promotion:	Dez 2001 – Mar 2005	Promotion am Deutschen Zentrum für Luft- und Raumfahrt, Göttingen, Deutschland
	Dez 2001 – Nov 2004	Stipendium der Deutschen Forschungs- gemeinschaft
	seit Dez 2004	Wiss. Ang. am III. Physikalischen Institut der Georg-August-Universität, Göttingen, Deutschland